

Wearable inductive  
damping sensors for skin  
edema quantification

Thesis by  
Tzu-Chieh Chou

In Partial Fulfillment of the Requirements for  
the degree of  
Doctor of Philosophy

The logo for the California Institute of Technology (Caltech), featuring the word "Caltech" in a bold, orange, sans-serif font.

CALIFORNIA INSTITUTE OF TECHNOLOGY  
Pasadena, California

2022  
(Defended November 5, 2021)

© 2021

Tzu-Chieh Chou  
ORCID: 0000-0002-6074-8286

All rights reserved except where otherwise noted

## ACKNOWLEDGEMENTS

I would not have been able to complete this thesis without the unconditional support of my mother, father, and sister. You have made me who I am today. I could not have completed this Ph.D. without your constant support and encouragement. I greatly appreciate the help from my longtime friends Dr. Jefferey Lin and Yue Yang. Our many discussions over the years have been memorable.

The Caltech MEMS lab would not be able to function without Trevor Roper's endless knowledge on machines and equipment. I am always amazed how you have managed to keep everything running. I have learned so much about how lab equipment works from you. Christine Garske, you cut through bureaucracy for us, and made it possible for us to do research. I think nothing would ever get done without you. Thank you for all your help over the years. Professor Tai, thank you for giving me the opportunity to work in your world-renowned lab. I am grateful for you took me on as a graduate student. It has been a unique opportunity to work be able to work on such cutting-edge subjects. Your guidance throughout my Ph.D. has molded my work.

I am glad I had the chance to work with Dr. Dongyang Kang, Dr. Juhyun Lee, Dr. Yang Liu, Dr. Shell Zhang, Dr. Yuan Luo, Dr. Nicholas Scianmarello, Dr. Aubrey Shapero, Dr. Colin Cook, Dr. Yudan Pi, Dr. Shane Shahrestani, Dr. Ting-Wei Wang, May Zi-Yu Huang, Allen Kuang-Ming Shang, Suhash Aravindan, and Haiku Shen. You have been splendid colleagues and I have learned a great deal from working alongside you all. I could not have asked for better lab mates.

Finally, I would like to thank my fellow friends at the Association of Caltech Taiwanese (ACT) who went through the long journey of Ph.D. together. It has always been a pleasure for me to hang out on Friday nights and play badminton in the Brown Gym over the weekends.

## ABSTRACT

The electrical conductivity of human organs is closely related to the physiological or pathological changes occurring within the organ. For example, metastatic liver tumors significantly increase electrical conductivity compared to healthy liver tissues over a wide frequency range. Therefore, knowing when and where these conductivity changes happen within an organ is highly valuable for disease monitoring.

Skin is the largest human organ by surface area, and under its large surface, there are numerous tiny blood and lymphatic vessels that circulate body fluid and dissipate heat. Therefore, it contains critical information about systemic circulation. Diseases such as congestive heart failure, acute renal injury, and liver failure disturb the systemic circulation and allow extra interstitial fluid to accumulate in the form of peripheral skin edema. As the interstitial fluid is highly conductive, the overall skin conductivity significantly increases when edema occurs.

Consequently, quantification of skin edema allows us to track the progression of these diseases and is the main goal to pursue in this study. The current clinical standard uses a 0-to-4 grade system to quantify the severity of edema based on how the skin responds to a pressing force. However, it requires in-person examination and has relatively large inter-examiner variations, making it less suitable for real-time edema monitoring.

To solve the unmet need to quantify edema in real-time, I present a skin edema model that relates skin conductivity to the interstitial fluid volume fraction. The latter is used to quantify the severity of edema. Furthermore, I developed a wearable coil sensor that provides accurate real-time conductivity measurements on subcutis, a significant portion of the skin where edema typically occurs. The coil sensor uses alternating magnetic fields to induce eddy currents in the skin and measures the skin conductivity as a function of coil resistance change. The experimental results suggested that when grade-1 edema occurs, the subcutis conductivity increases from the average value of 0.09 S/m to 0.25 S/m. This change corresponds to an increase of interstitial volume

fraction from 10% to 20% in the subcutis. These quantitative results are consistent with finite element simulations and allow direct comparison with ultrasonography measurements. Due to its high accuracy and portability, the proposed wearable sensor opens a new possibility for continuous monitoring of skin edema.

## PUBLISHED CONTENT AND CONTRIBUTIONS

Yu-Chong Tai, Tzu-Chieh Chou, and Shane S. Shahrestani (2019). “Wearable Inductive Damping Sensor”. In: *United States Patent Application Publication*, US 2020/0082926 A1. URL: <https://patents.google.com/patent/US20200082926A1/en>.

T.-C. C. participated in the conception of the invention, prepared the data, and participated in the writing of the patent application.

All third-party materials incorporated in the thesis are reprinted with permission from the copyright holder, as indicated in the figure captions.

## TABLE OF CONTENTS

|  |       |
|--|-------|
| Acknowledgements.....  | iii   |
| Abstract .....   | iv    |
| Published Content and Contributions.....   | vi    |
| Table of Contents.....   | vii   |
| List of Illustrations.....   | x     |
| List of Tables.....  | xviii |
| <br>   |       |
| <i>Chapter 1</i> INTRODUCTION.....   | 1     |
| 1.1    MOTIVATION OF THIS WORK.....  | 1     |
| 1.2    PREVIOUS WORKS ON SKIN EDEMA QUANTIFICATION .....   | 2     |
| MECHANICAL IMPEDANCE .....   | 2     |
| PITTING TEST.....  | 4     |
| ULTRASOUND VISCOELASTICITY.....  | 5     |
| ULTRASOUND ECHOGENICITY .....  | 8     |
| CAPACITIVE SENSING.....  | 11    |
| BIOIMPEDANCE SPECTROSCOPY .....  | 12    |
| EDDY CURRENT METHOD .....  | 13    |
| B-MODE ULTRASONOGRAPHY .....   | 15    |
| MAGNETOMETER ANKLE CIRCUMFERENCE SENSOR.....   | 17    |
| OPTICAL LIMB VOLUMETRY .....   | 17    |
| NEAR-INFRARED SPECTROSCOPY .....   | 19    |
| THERMAL DIFFUSIVITY .....  | 21    |
| MAGNETIC RESONANCE IMAGING.....  | 23    |
| 1.3    PREVIOUS WORKS ON SKIN EDEMA QUANTIFICATION .....   | 24    |
| 1.4    THESIS OUTLINE.....   | 26    |
| 1.5    REFERENCES .....  | 27    |
| <br>   |       |
| <i>Chapter 2</i> SKIN ANATOMY, EDEMA PATHOLOGY, AND INTERSTITIAL FLUID MODEL.....                                | 29    |
| 2.1    HUMAN SKIN ANATOMY .....  | 29    |
| MACROSCOPIC STRUCTURES OF THE SKIN – EPIDERMIS, DERMIS, AND SUBCUTANEOUS SPACE .....                             | 29    |
| MICROSCOPIC STRUCTURES OF THE SKIN – EXTRACELLULAR MATRIX, INTERSTITIAL FLUID, AND INTRACELLULAR COMPONENT ..... | 32    |
| MICROCIRCULATION IN THE SKIN .....   | 33    |
| 2.2    SKIN EDEMA PATHOLOGY .....  | 35    |
| COMMON DISEASES LEADING TO SKIN EDEMA .....  | 35    |

|                  |   |    |
|------------------|---|----|
|                  | PATHOLOGICAL CHANGES RELATED TO SKIN EDEMA.....                               | 37 |
| 2.3              | INTERSTITIAL FLUID MODEL .....  | 40 |
|                  | SKIN THICKNESS AND INTERSTITIAL FLUID VOLUME FRACTION .....                   | 40 |
|                  | FREQUENCY DEPENDENCY OF SKIN CONDUCTIVITY .....                               | 42 |
| 2.4              | REFERENCES .....  | 46 |
| <br>             |   |    |
| <i>Chapter 3</i> | SKIN EDEMA SENSOR BASED ON LC-RESONATOR ..                                    | 48 |
| <br>             |   |    |
| 3.1              | PROPOSED METHOD FOR SKIN EDEMA QUANTIFICATION ..                              | 49 |
|                  | SKIN EDEMA AND SKIN CONDUCTIVITY .....  | 49 |
|                  | LC-RESONATOR AS EDDY CURRENT SENSOR.....                                      | 50 |
| 3.2              | SKIN CONDUCTIVITY SENSOR.....   | 54 |
|                  | COIL SENSOR .....   | 54 |
|                  | PRINTED CIRCUIT BOARD LAYOUT .....  | 57 |
|                  | RESISTANCE AND INDUCTANCE TO DIGITAL CONVERTER .....                          | 58 |
|                  | TEMPERATURE COMPENSATION CIRCUIT .....  | 60 |
|                  | SENSOR TESTING.....   | 62 |
|                  | LIMITATIONS OF THE SENSOR .....   | 68 |
| 3.3              | REFERENCES .....  | 71 |
| <br>             |   |    |
| <i>Chapter 4</i> | THEORETICAL ANALYSIS FOR SENSOR OPTIMIZATION .....                            | 73 |
| <br>             |   |    |
| 4.1              | COIL OPTIMIZATION .....   | 73 |
|                  | COIL GEOMETRY AND GEOMETRIC DAMPING EFFICIENCY .....                          | 74 |
|                  | COIL RESISTANCE AND ELECTRICAL DAMPING EFFICIENCY ...                         | 79 |
|                  | COIL FOCAL SPREAD AREA AND HALF-LOSS PENETRATION DEPTH .....                  | 82 |
| 4.2              | NOISE ANALYSIS.....   | 83 |
|                  | THERMAL NOISE.....  | 83 |
|                  | PHASE NOISE AND AMPLITUDE NOISE.....  | 84 |
| 4.3              | REFERENCES .....  | 88 |
| <br>             |   |    |
| <i>Chapter 5</i> | COIL SENSOR SIMULATION AND EXPERIMENTAL RESULTS .....                         | 89 |
| <br>             |   |    |
| 5.1              | AC RESISTANCE OF COILS MADE FROM THE LITZ CABLE ...                           | 91 |
| 5.2              | MAGNETIC FIELD, INDUCED ELECTRICAL FIELD, AND VOLUMETRIC INDUCTIVE LOSS ..... | 95 |
| 5.3              | ANATOMICAL MODEL OF THE HUMAN ANKLE .....                                     | 97 |
| 5.4              | FABRICATION OF WEARABLE INDUCTIVE DAMPING SENSORS.....                        | 99 |
|                  | COIL FABRICATION .....  | 99 |



|   |     |
|---|-----|
| PRINTED CIRCUIT BOARD FABRICATION.....  | 100 |
| 5.5 MEASUREMENTS FROM CONDUCTIVITY STANDARDS,<br>SALINE SOLUTIONS AND GELATIN PHANTOMS..... | 102 |
| POTASSIUM CHLORIDE CONDUCTIVITY STANDARDS AND<br>SALINE SOLUTIONS.....                      | 102 |
| GELATIN PHANTOMS WITH VARYING THICKNESS AND SALINE<br>SOAKING TIME.....                     | 104 |
| 5.6 RESULTS FROM HEALTHY HUMAN SUBJECTS.....  | 108 |
| VACUUM INDUCED SUBCUTANEOUS EDEMA CONDUCTIVITY<br>.....                                     | 108 |
| SKIN THICKNESS MEASUREMENTS.....  | 110 |
| 5.7 REFERENCES.....   | 112 |
| <i>Chapter 6</i> MAGNETIC SHIELDING FOR IMPROVED SENSOR<br>PERFORMANCE.....                 | 113 |
| 6.1 SIMULATION SETUP.....   | 114 |
| 6.2 SIMULATION RESULTS.....   | 115 |
| SPREAD OF INDUCTIVE LOSS DISTRIBUTION.....  | 115 |
| RATIO OF TARGET LOSS TO TOTAL LOSS.....   | 122 |
| 6.3 EXPERIMENTAL RESULTS.....   | 123 |
| 6.4 REFERENCES.....   | 125 |
| <i>Chapter 7</i> CONCLUSION AND FUTURE WORKS.....   | 126 |

## LIST OF ILLUSTRATIONS

- Figure 1.1:** Semi-quantitative grading of skin edema using the pitting test. (a) Photo of pitting edema in the leg. A dimple on the skin is clearly visible after the finger press. (b) Grading of skin edema based on  $d_{max}$  is commonly used in a clinical setting. Figure (a) is reprinted under the license from Wikipedia (Heilman, 2010).  
..... 5
- Figure 1.2:** Ultrasound viscoelasticity imaging. (a) Experimental setup. (b) The viscoelastic model of the tofu skin phantom. (c) Measured time constant  $\tau = E1/\eta1$  as a function of depth. (d) Measured elastic modulus  $E1$  in the viscoelastic model as a function of depth. For tofu skin phantom “A” in subfigures (c) and (d), the outliers with an r-squared value less than 0.9 are marked in red and so are the corresponding depth on the x-axis. The figures are reprinted with permission from Elsevier (Pitre et al., 2016).  
..... 7
- Figure 1.3:** Ultrasound echogenicity measurements in the forearm. (A) MRI (left column) and ultrasound images (right column) showing normal skin (top row) and edematous skin (bottom row). The epidermis layer is marked by “E” and the dermis-subcutis interface is marked by “P”. Black arrows indicate the histamine injection site and local skin edema. Black asterisks indicate the surface of the ultrasound transducer. (B) NMR spectra showing water and fat peaks. Solid curve is from normal skin and dashed curve is from edematous skin. (C) the regression lines showing the correlation between the number of low echogenic pixels (LEP) and the logarithmic value of the water-to-fat ratio in the NMR spectrum taken from the edematous skin. The figures are reprinted with permission from John Wiley and Sons (Gniadecka and Quistorff, 1996).  
..... 9
- Figure 1.4:** Ultrasound echogenicity measurements from the subcutaneous tissue in the lower legs. (a) The measurement setup including a portable ultrasound probe (left) and a custom-made gel pad on the skin surface (right). The gel pad with uniform acoustic impedance is used as the echogenicity reference for objective edema quantification. (b) Representative B-mode ultrasound images of subcutaneous edema (A) and normal skin (B) showing different levels of echogenicity compared to the gel pad reference (C) in the subcutis layer (D). Figures are reprinted under Creative Commons Attribution 4.0 International (Lu et al., 2013).  
..... 10
- Figure 1.5:** Capacitive sensing of dielectric constants of skin. (a) The operating principle of the capacitive skin hydration sensor uses the fringing electric field (dashed lines) to sense the changes in the skin’s effective dielectric constant. (b) The simulated electric potential in the skin for a commercial capacitive skin hydration sensor (E100). Note the dependency of measurement depth on the material dielectric constant. The detection threshold is set to 0.01 V. Figures (b) and (c) are reprinted under the Creative Commons Attribution License (Bontozoglou and Xiao, 2020).  
..... 11

- Figure 1.6:** Bioimpedance spectroscopy. (a) The block diagram of the multi-frequency bioimpedance spectroscopy sensor showing the 4-electrode skin interface (A), sensing electronics (B), and mobile app (C) that collects and transmits data wirelessly. (b) The fitted impedance loci from Cole-Cole dispersion model over time. The “hydration factor”  $H$  as a function of time is derived as the ratio  $Re/Ri$  (see context for derivations). Figures are reprinted with permission (Allegrì et al., 2017). © 2017, IEEE..... 13
- Figure 1.7:** The eddy current method for measuring tissue conductivity. (a) Noninvasive conductivity sensor based on serial RLC resonant circuit with gapped ground shielding. (b) Coil resistance change versus conductivity in the target. The figures are reprinted with permission (Hart et al., 1988). © 1988, IEEE..... 14
- Figure 1.8:** B-mode ultrasonography study on the correlation between skin thickness and lower leg edema. (a) SonoSite 5 MHz convex array ultrasound probe used in the study and the schematic drawing showing the measurement location. (b) B-mode ultrasonography showing the thickness of normal skin (top) and the edematous skin (bottom). The blue arrows indicate the start and end of the skin section, which includes epidermis (marked by “1”), dermis (marked by “2”), and subcutaneous fat (marked by “3”). The measured skin thickness is on the top left. (c) Overall skin thickness data including both the obese and non-obese groups. (d) Skin thickness data separating the two groups. The figures are reprinted under the Creative Common Attribution-NonCommercial-NoDerivatives 4.0 International (Yanagisawa et al., 2019)..... 16
- Figure 1.9:** Magnetometer-based ankle circumference sensor (a) Schematic drawing of the sensor. The inductor generates a static magnetic field that is measured by two 3-axis magnetometers located on the opposite sides. (b) Sensor band readout versus different ankle diameters and test runs, showing the accuracy and reliability of the sensor. The figures are reprinted with permission (Zhang and Rajamani, 2015). © 2015, IEEE..... 17
- Figure 1.10:** Comparison of two optical limb volume measurement methods. (a) Photos showing the near-infrared optical volumetry that uses an optical scanner to obtain the cross-sectional area at each limb slice (left) and the 3-D depth volumetry that uses a 3-D camera to obtain the depth information from the limb surface (right). (b) Optical image showing a human forearm and the reconstructed limb from the 3-D depth information. (c) Comparison of limb volume measured by the two methods. Note that the limb volume estimated by the 3-D camera is always higher than that measured by the perometer. Figures (a) and (b) are reprinted with permission (Lu et al., 2013). © 2013, IEEE..... 18
- Figure 1.11:** Near-infrared spectroscopy imaging. (A) Multispectral images of the skin at 560 nm (a), 580 nm (b), 700 nm (c), and 970 nm (d). Skin erythema is visible in (a)(b) due to strong hemoglobin absorption, while skin edema is identified in (d) due to excess water absorption at histamine injection sites (indicated by white arrows). (B) Concentration maps of different chromophores including oxy-hemoglobin (a), deoxy-hemoglobin (b), water (c), and collagen fibers (d). The injection sites are indicated by white arrows. Figures are reprinted with permission (Stamatas et al., 2006). ..... 20

- Figure 1.12:** The apparent erythema and skin edema indices. They are derived from the concentration of oxy-hemoglobin (a) and water (b), respectively. Figures are reprinted with permission (Stamatas et al., 2006)..... 21
- Figure 1.13:** Thermal diffusivity skin hydration sensor. (A) Cross-sectional view of the skin that includes sebaceous glands (1), eccrine sweat glands (2), blood vessels (3), epidermis, and dermis. (B) Flow chart that shows the conversion from temperature sensor readings to the water content in epidermis and dermis. (C)(D) Simulated temperature profiles showing the heat transfer into the dermis after 2 seconds and 13 seconds. (E)(F) The dependency of temperature change on epidermis and dermis water content. (G) Measured epidermis and dermis water content at various body locations. Figures are reprinted with permission (Madhvapathy et al., 2020)..... 22
- Figure 1.14:** Magnetic resonance imaging for skin edema quantification. High resolution chemical shift magnetic resonance images (A) showing water content (a) and fat content (b) of a normal leg, and (B) showing water content (a) and fat content (b) of a leg with lymphedema. Scale bars are 1 mm. D = dermis, M = muscle, F = fatty tissue. Figures are reprinted with permission (Idy-Peretti et al., 1998). 23
- Figure 2.1:** Cross-section view of the human skin showing the macroscopic four-layer structure (the epidermis, dermis, subcutis/hypodermis, and bone in **bold** text) and microscopic components in the thick, hairless skin (left) and thin, hairy skin (right). Figure is licensed from Wikipedia and remixed with the addition of the bone layer (Komorniczak and Madhero88, 2012). ..... 30
- Figure 2.2:** (a) Body mass distribution shows the average adult's solid and fluid weight percentages. The liquid portion is divided into the intracellular and extracellular components, and the latter contains both the interstitial fluid and blood plasma. (b) The schematic drawing shows the location of the main body fluid components. The figure is reprinted under Creative Commons Attribution-ShareAlike 4.0 International License (Biga et al., 2019),..... 32
- Figure 2.3:** (a) Body fluid composition showing the concentrations for each ion type. Note the similarities between blood plasma and interstitial fluid. The figure is reprinted under Creative Commons Attribution-ShareAlike 4.0 International License (Biga et al., 2019). (b) The electrical conductivity of blood plasma and interstitial fluid derived from ion concentrations (blue) and experimental measurements (orange) at body temperature (Peters et al., 2005). ..... 33
- Figure 2.4:** (a) The revised Starling equation shows the glycocalyx-cleft model (red dashed line and arrows) and the classical filtration-reabsorption model (black dashed line and arrows). Net capillary opposing pressures  $P_{co} = \sigma\Pi_p - \Pi_i + P_i$  are shown in dashed lines. Continuous drainage of the interstitial fluid by the lymphatics replaces the role of reabsorption in the glycocalyx-cleft model. The figure is reprinted with permission from the Oxford University Press (Levick and Michel, 2010). (b) Starling's pressures measured in human subcutis from arms with lymphedema (orange) and control arms on the contralateral side (blue). Note that lymphedema arms have lower  $\Pi_i$  and higher  $P_i$  than the control. .... 34

- Figure 2.5:** (a) The schematic drawing of the experimental setup showing the fluid collection needle and the pressure transducer for interstitial pressure measurements in the leg with deep vein thrombosis. (b) The measured pressure components in Starling's equation.  $P_v$  and  $P_{if}$  are the saphenous vein pressure and interstitial pressure,  $COP_{pl}$  and  $COP_{if}$  are the colloid osmotic pressure of the blood plasma and interstitial fluid,  $P_r$  is the reabsorption pressure. Control group: empty boxes. Thrombosed legs: solid boxes. Contralateral legs: grid boxes. Values are presented as mean plus standard deviation. The \* symbol denotes thrombosed legs significantly different from contralateral legs. The † symbol denotes the control group significantly different from contralateral legs. The figures are reprinted with permission from Taylor & Francis (Seem and Strandén, 1986). ..... 37
- Figure 2.6:** Skin ultrasonography images from (a) normal skin and (b) skin with severe subcutaneous edema. The interface between dermis and subcutis is visible in normal skin (a), which is indicated by white solid crosses. However, the interface is not visible in the skin with severe subcutaneous edema (b). On the other hand, interstitial fluid invasion is visible in (b) as dark low echogenic regions indicated by white hollow triangles. The figures are reprinted with permission from Taylor & Francis (Rönkä et al., 2004). ..... 38
- Figure 2.7:** Histology images from (a) normal skin (magnification ratio 10x) and (b) skin with mild to moderate edema (magnification ratio 100x) stained with H&E. The mild edema has a pale-white appearance in the papillary dermis and is not stained well by H&E. The areas intruded by the interstitial fluid are indicated by white hollow triangles. Figure (a) is reprinted and licensed from Wikipedia (Kilbad, 2008). Figure (b) is reprinted with permission from Elsevier (Berg et al., 2013). ..... 39
- Figure 2.8:** Electric circuit model of biological tissues showing the extracellular branch of resistance  $R_e$  and the intracellular branch with resistance  $R_i$  and membrane capacitance  $C_m$  in series. .... 40
- Figure 2.9:** Skin conductivity model based on the subcutaneous thickness and interstitial fluid volume fraction. .... 41
- Figure 2.10:** Conductivity spectrum of different skin layers and the whole skin under different conditions (dry, wet, and edema). The stratum corneum (green solid square) dominates the skin impedance below 100 kHz. The beta dispersion is visible from 100 kHz to 10 MHz. The distinction between dry and wet skin becomes smaller when the frequency is above 10 MHz. The wet skin and skin with edema conductivity data at 6 kHz are measured with two needles inserted into the skin (Hladovec and Přerovský, 1973). The dermis, subcutis, and stratum corneum data below 1 MHz are measured by a non-invasive electrode probe on human female forearms (Birgersson et al., 2010). ..... 44
- Figure 2.11:** The typical four-order Cole-Cole model of bone, skin and fat showing the conductivity (a) and relative permittivity (b) versus frequency (Sasaki et al., 2014). ..... 44

- Figure 3.1:** Invasive skin conductivity measurements on edema patients. (a) The schematic drawing of the experimental setup. (b) skin conductivity values of healthy and edematous skin at 6 kHz (Hladovec and Přerovský, 1973)..... 49
- Figure 3.2:** Eddy current model of the coil sensor showing the sensor-target inductive coupling and the corresponding transformer model (Redpath and Hutchison, 1984). ..... 51
- Figure 3.3:** Simplified equivalent circuit model from the transformer model when the coil sensor is (a) undamped and (b) inductively damped by the target. .... 52
- Figure 3.4:** Simulation results showing (a) the skin effect and (b) the proximity effect in solid copper wires with a diameter of 2 mm. The skin depth of copper is 0.206 mm at 100 kHz. The currents are concentrated near the wire surface with the highest current density (red) and drops to  $1/e$  of the maximum value at one skin depth from the surface (light blue)..... 55
- Figure 3.5:** Block diagram of the LDC1101 ASIC. .... 58
- Figure 3.6:** Circuit diagrams showing (a) the hypothesized current driving circuitry consisting of two cross-coupled pairs, (b) simplified circuit model of the negative resistance cross-coupled differential pair oscillator, and (c) driving current profile of LDC1101 assuming the cross-coupled differential pair is in the current limited regime (Hajimiri and Lee, 1999). .... 59
- Figure 3.7:** Custom-made coil's DC resistance  $R_{dc}$  as a function of temperature..... 63
- Figure 3.8:** Typical ESR profile of a surface-mounted multi-layer ceramic capacitor showing frequency ranges dominated by dielectric loss below the self-resonant frequency ( $\sim 500$  MHz) and metallic loss above the self-resonant frequency. . 65
- Figure 3.9:** Equivalent circuit model for a multi-layer ceramic capacitor (MLCC). ESR = equivalent series resistance, ESL = equivalent series inductance. .... 65
- Figure 3.10:** Frequency counter measurements showing the average reference frequency at 16 MHz (left) and standard deviation (right)..... 66
- Figure 3.11:** Coil quality factor measurements. (a) The Q-meter measurement setup. (b) The electrical circuit model of the Q-meter. The quality factor (Q) is the ratio of the capacitor voltage amplitude (E) to the injection voltage amplitude (e) at the resonant frequency..... 67
- Figure 3.12:** Measured quality factor Q and series resistance  $R_s$  of the sensor coil. ... 68
- Figure 4.1:** (a) Circular coil geometry showing the rectangular cross-section and geometric parameters (b) Conceptual drawing of the geometric damping efficiency. .... 76
- Figure 4.2:** Components of the total resistance  $R_s$ . .... 79
- Figure 4.3:** (a) Equivalent circuit of the LC oscillator at the damped resonant frequency  $\omega d$ , and (b) the same equivalent circuit with total resistance  $R_s$  expanded to show the individual resistive components. The electrical damping efficiency, defined as the ratio of total inductive loss to the coil loss, is equal to the ratio  $R_i/R_s$  as all the resistive components are in series. See Figure 4.2 for definitions for each resistive element..... 80
- Figure 4.4:** Contour plots of the induced electrical field intensity  $|\mathbf{E}|$  showing the half-maximum contour of an axially symmetric planar circular coil. The half-field spread  $SE/2$  is approximately the surface area enclosed by the  $E_{max}/2$

- contour surface (black arrow in the left figure). The half-field depth  $dE/2$  is the maximum depth of the 2-D contour line representing  $E_{max}/2$  (black arrow in the right figure). Note the colormap in the 3-D contour plot (left) is adjusted for better visualization..... 83
- Figure 4.5:** The linear time-varying system model showing the impulse sensitivity function for the phase modulation process in an oscillator..... 84
- Figure 4.6:** The time domain oscillation voltage waveform measured across one of the coil terminals and ground. The amplitude noise resulted from the current injection is indicated by the white double arrow..... 86
- Figure 4.7:** Representative phase noise spectrum of the oscillation voltage waveform near the sensor resonant frequency at 4.8 MHz. Maximum frequency offset is 50 kHz from the resonant frequency. Horizontal scale is 10 kHz per division. Vertical scale is 10 dBVrms per division..... 87
- Figure 5.1:** The schematic drawing of the 2-D axially symmetric model. The symmetric axis is  $r = 0$ . The coil lies flat on the  $z=0$  surface and has its height and width as free variables. The target ( $z<0$ ) is positioned right below coil and contains four layers (epidermis, dermis, subcutis, and bone). The air domain ( $z>0$ ) surrounds the coil and target from above and is assigned with zero conductivity. The purple region is the infinite domain that contains a stretched mesh to approximate an infinitely large space. Note the target also stretches out to infinity in this model..... 91
- Figure 5.2:** 7-turn, 1-inch diameter solenoid coil geometry used in the simulation. The magnified view of the Litz cable showing the individual strands is on the right. .... 92
- Figure 5.3:** The current density in the azimuthal direction at (a) 500 kHz where the stand diameter to skin depth ratio  $ds\delta\sim 14$  and (b) 5 MHz where the stand diameter to skin depth ratio  $ds\delta\sim 1$ . The proximity effect is visible at 5 MHz near the edge of the Litz cable (indicated by the black arrow)..... 94
- Figure 5.4:** Simulated coil properties. (a) Coil resistance and (b) coil inductance as a function of frequency..... 95
- Figure 5.5:** Two types of target geometry used in the axially symmetric model (left) cylindrical target (right) ellipsoidal target. The coil position remains the same in both cases..... 96
- Figure 5.6:** Volumetric loss function in the (a) cylindrical target and (b) ellipsoid target at 8 MHz. Note the differences in the color map scale. .... 97
- Figure 5.7:** 3D model of the right foot showing (a) the surface curvature and (b) magnetic flux intensity..... 98
- Figure 5.8:** Cross-sectional views of the ankle showing (a) different layers under the skin and the relative location of the coil sensor, (b) conductivity distribution under normal conditions, and (c) conductivity distribution under subcutaneous edema conditions. .... 98
- Figure 5.9:** Cross-sectional views of the ankle showing (a) magnetic flux intensity distribution, (b) volumetric loss density function under normal conditions, and (c) volumetric loss density function under subcutaneous edema conditions. ... 99
- Figure 5.10:** Block diagram of the custom designed PCB for LDC1101..... 101

- Figure 5.11:** Schematic drawing (left) and photo (right) of the experimental setup for measuring the conductivity standards. The plastic bottle containing the conductivity standard has a volume of 500 mL and a diameter of 7 cm. The height of the plastic support is 25 cm. .... 103
- Figure 5.12:** The coil resistance increase  $\Delta R_s$  as a linear function of conductivity. (a) Results from potassium chloride conductivity standards (500 mL, diameter = 7cm) measured at 5 MHz. (b) Results from sodium chloride solutions (25 mL, diameter = 2 cm) measured at 7.7 MHz. The room temperature was at 25 degrees Celsius. .... 104
- Figure 5.13:** The experimental setup for gelatin phantom soaking test. .... 105
- Figure 5.14:** The four-electrode circuit diagram (left) and experimental setup (right). The currents  $I_1$  and  $I_2$  flowing into the oscilloscope probes are assumed to be negligible compared to the total current  $I$ . The voltage source is from a commercial signal generator. The oscilloscope has a sampling rate of 500 MSPS. The letters (A, B, C, and D) mark the wiring connections to the four electrodes. The electrode pair A-D provides the driving current  $I$  while the pair B-C senses the voltage drop  $V$ . The resistor  $R$  serves a current-sensing element and limits the amount of current flowing through the sample to prevent overload.  $R_e$  denotes the electrode resistance. .... 106
- Figure 5.15:** The measured increase in coil resistance  $\Delta R_s$  as a function of measured four-point probe conductivity from the 46.0 g gelatin phantom. The r-square value of the linear fit line is 0.97. .... 107
- Figure 5.16:** (a) Schematic drawing of the experimental setup for vacuum suction induced edema, and (b) a photo showing the vacuum pump integrated with the skin edema sensor (top) and the induced skin edema (bottom). Measurements were taken from human ankle over 30 minutes. .... 109
- Figure 5.17:** Experimental results from healthy human subjects. (a) relative thickness change of dermis and subcutis as a function of negative pressure applied to the skin, (b) subcutaneous conductivity predicted by the edema model and Archie's law (blue solid line) and measured by the skin edema sensor (orange error bars). Measurements were taken from human ankle over 15 minutes. .... 109
- Figure 5.18:** Skin thickness measurement setup. (left) schematic drawing of the setup dimension and relative locations of the ultrasound transducer and skin edema eddy current damping (ECD) sensor, (right) the motion-mode ultrasound image captured by the skin thickness sensor. The epidermis is below the axial resolution of the ultrasound transducer and is labeled with an arrow to only indicate its boundary. .... 111
- Figure 6.1:** The schematic drawing of the 2-D axially symmetric model of ferrite magnetic shielding. The symmetric axis is  $r = 0$ . The purple region is the domain that contains the ferrite material with relative permeability of 130. The shielding thickness  $t$ , air gap width  $w$  and height  $h$  are the changing variables. The target ( $z < 0$ ) is positioned right below coil and contains three layers (epidermis, dermis, and subcutis). The region of interest has a cross-section area of 40 mm (width) by 8 mm (depth). The air domain ( $z > 0$ ) surrounds the coil,



- magnetic shielding, and target from above and is assigned with zero conductivity. .... 114
- Figure 6.2:** The schematic drawing of the volume integration to calculation the cumulative loss distribution in the skin ( $z < 0$ ). The red area is the region for the definite volume integral in equation 6.1. Also note that the integration is taken on a revolved geometry that has a symmetric axis at  $r = 0$ . .... 116
- Figure 6.3:** Comparison of the cumulative loss distribution for the coil sensor with different magnetic shielding thickness values (top-left: 8 mm, top-right: 4 mm, bottom-left: 2 mm, bottom-right: 1 mm). Doubling the shielding thickness increases the total loss by about 13% but has almost no effect on the equal loss contours. For  $t = 1$  mm (bottom-right), a slight change in the 97.5% loss contour is visible (blue arrow). .... 118
- Figure 6.4:** Comparison of the cumulative loss distribution for the coil sensor with different bottom magnetic shielding thickness values (top-left: 4 mm, top-right: 2 mm, bottom-left: 1 mm, bottom-right: 0 mm). The top and side magnetic shielding thickness is 8 mm. The opening width of the bottom shielding is 4 mm. .... 119
- Figure 6.5:** Comparison of the cumulative loss distribution for the coil sensor with different bottom magnetic shielding opening widths (top-left: 0.5 mm, top-right: 1 mm, bottom-left: 2 mm, bottom-right: 4 mm). The top and side magnetic shielding thickness is 2 mm. The bottom magnetic shielding thickness is 1 mm. .... 120
- Figure 6.6:** Comparison of the inductive loss density for the coil sensor with different bottom magnetic shielding opening widths (top-left: 0.5 mm, top-right: 1 mm, bottom-left: 2 mm, bottom-right: 4 mm). The top and side magnetic shielding thickness is 2 mm. The bottom magnetic shielding thickness is 1 mm. .... 121
- Figure 6.7:** Comparison of the cumulative loss distribution for the coil sensor without magnetic shielding (left) and with optimal magnetic shielding (right). The 82.5% cumulative loss ratio contours are indicated by orange arrows. Note that  $P_{max}$  increases by more than 250% in the improved sensor design, and radial spread is reduced from 25 mm to 20 mm (orange arrows). The orange boxes represent the cylinder containing 82.5% of total inductive loss. .... 122
- Figure 6.8:** Loss ratio for different gap distance between the coil and target. (a) Sensor without magnetic shielding, (b) sensor with top and side magnetic shielding (opening width = coil windings width). .... 123
- Figure 6.9:** (a) Schematic drawing of the experimental setup to measure the inductive loss versus depth profile. (b) Photo of the coil sensor with optimized magnetic shielding design. .... 124
- Figure 6.10:** (a) Comparison of the experimentally measured resistance with simulations. The only fitting parameter used is the initial coil resistance when no saline is present (saline thickness = 0 mm). (b) Comparison of the measured resistance increase from coil designs with and without magnetic shielding. .... 124

## LIST OF TABLES

|   |    |
|---|----|
| <b>Table 1.1:</b> Summary of current non-invasive quantitative methods to detect skin edema.....  | 25 |
| <b>Table 2.1:</b> Classification of skin edema pathology according to different parameters in the Starling equation (Cho and Atwood, 2002). ..... | 36 |
| <b>Table 2.2:</b> Multiple Cole-Cole dispersion model parameters ( $n = 4$ ) of various tissue types (Sasaki et al., 2014). .....                 | 45 |
| <b>Table 3.1:</b> Ratio of AC resistance to DC resistance, $H$ , for an isolated solid round wire. ....   | 56 |
| <b>Table 3.2:</b> Factor $K$ as a function of the number of strands $n_s$ . ....  | 56 |
| <b>Table 4.1:</b> Common coil geometries and comparison of their geometric damping efficiency $\eta_G$ .....                                      | 78 |
| <b>Table 5.1:</b> Parameters of a solenoid coil made from the Litz cable .....  | 93 |
| <b>Table 5.2:</b> Parameters of two types of target geometry .....  | 95 |

*Chapter 1*

## INTRODUCTION

**1.1 MOTIVATION OF THIS WORK**

Skin edema in the lower limbs has been shown to correlate with chronic systematic diseases such as congestive heart failure and acute diseases such as deep vein thrombosis (Cho and Atwood, 2002). Therefore, detecting edema is important for diagnosing these diseases.

There are two types of needs regarding skin edema detection. Firstly, for acute diseases like deep vein thrombosis (DVT), the symptom can appear and worsen in 72 hours. In this case, early detection of edema can give out warnings before the blood clots from DVT break free and circulate in the bloodstream. When the circulating blood clots get stuck in the lungs, they can potentially cause a life-threatening disease called pulmonary embolism.

Secondly, for long-term diseases like chronic kidney disease, the patients need regular dialysis to maintain the body fluid balance. In this case, continuous and accurate monitoring of the skin water content is desirable for determining when to go for the dialysis, and if the treatment outcome is satisfactory. Another long-term disease example is lymphedema resulting from breast cancer surgery. Patients with breast cancer usually have their lymph nodes removed so the lymphatic drainage deteriorates. This causes the interstitial fluid to build up over time and form swollen arms, a typical symptom for lymphedema. Therefore, continuous post-surgery monitoring can help prevent lymphedema and improve patient life quality.

From the two types of needs mentioned above, it is desirable to have a device that provides objective, continuous, automatic, non-invasive, and highly accurate measurements of skin edema. Considering the age group of the potential users, the

device should also be accessible, low-cost, not relying on experts, and convenient to use. A wearable skin edema sensor has the potential to overcome these challenges as it can be integrated into a smart device for health monitoring. However, this goal is yet to be accomplished. There are a lot of efforts in the field that try to address this challenge, and yet they are not adequate as I will explain in the next section.

## **1.2 PREVIOUS WORKS ON SKIN EDEMA QUANTIFICATION**

From the two types of needs mentioned above, it is desirable to have a device that provides objective, continuous, automatic, non-invasive, and highly accurate measurements of skin edema. Considering the age group of the potential users, the device should also be accessible, low-cost, not relying on experts, and convenient to use. A wearable skin edema sensor has the potential to overcome these challenges as it can be integrated into a smart device for health monitoring. However, this goal is yet to be accomplished. There are a lot of efforts in the field that try to address this challenge, and yet there are still gaps to fill in as I will explain in this section.

### *MECHANICAL IMPEDANCE*

When excessive interstitial fluid enters the subcutaneous space, the extracellular matrix (ECM) expands to accommodate the increase in hydrostatic pressure. The pressure-volume relationship is characterized by interstitial compliance, which is defined by the ratio of interstitial volume change to pressure change:  $C = \Delta V / \Delta P$ .

Previous studies showed that during tissue hydration, the effective pore size of the ECM increases, causing a greater portion of tissue water to become available for solute redistribution. In addition, the interstitial compliance changes abruptly to a much higher value when the interstitial water content increases by 20% from its normal value (Scallan et al., 2010).

As a result of higher hydraulic conductance (the ability to allow interstitial fluid flow), the mechanical properties of an edematous tissue change significantly under both static and dynamic loading conditions. For the static loading condition, a

constant deformation is applied to the tissue and the peak force is recorded. The relation between the peak static force  $F$  and can be approximated by the Hooke's law:

$$F = kd \quad (1.1)$$

, where  $F$  is the force,  $d$  is the deformation, and  $k$  is the stiffness.

The  $F$ - $d$  curve has a decreasing slope (corresponding to stiffness  $k$ ) when the water percentage increases from 88% to 96% in gelatin tissue phantoms (Mridha and Odman, 1985). In addition, a higher force difference  $\Delta F$  exists between the edematous limb and contralateral normal limb at large deformations ( $> 5$  mm). On the other hand, there is no significant force difference between the two limbs in healthy subjects. These observations lead to the conclusion that tissue stiffness can be used to characterize tissue edema.

For the dynamic loading condition, the tissue vibrates sinusoidally with a constant maximum velocity at various frequencies. The steady-state force  $F$  and velocity  $V$  can be represented by the phasor notation as  $F = \bar{F}e^{j\omega t}$  and  $V = \bar{V}e^{j\omega t}$ . The ratio of  $\bar{F}$  to  $\bar{V}$  is defined as the mechanical impedance  $Z = \frac{\bar{F}}{\bar{V}}$ , which is the mechanical analogy of electrical impedance. The mechanical impedance can be derived as follows:

$$F = m \frac{dV}{dt} + bV + k \int V dt \quad (1.2)$$

$$\bar{F} = \left( j\omega m + b + \frac{k}{j\omega} \right) \bar{V} \quad (1.3)$$

$$Z = \frac{\bar{F}}{\bar{V}} = j\omega m + b + \frac{k}{j\omega} \quad (1.4)$$

, where  $m$  is the mass,  $b$  is the damping, and  $k$  is the stiffness.

At frequencies  $\omega \ll k/b$ , the stiffness term  $\frac{k}{j\omega}$  dominates the mechanical impedance  $Z$ . Therefore,  $Z$  has a phase close to  $-90$  degrees and an amplitude decreasing at  $-20$  dB/decade in the low frequency range. Furthermore, the ratio of  $Z$  is approximately proportional to the ratio of stiffness  $k$ . In vitro mechanical impedance measurements from 10 Hz to 1000 Hz confirmed the  $Z$  ratio between two limbs is higher for people with unilateral edema, and the edematous limb has lower  $Z$  compared to normal limb up to 30 Hz (Mridha and Odman, 1985).

### *PITTING TEST*

The pitting test, which is the clinical standard for edema assessment, is looking at the time-domain characteristics of the tissue response. The examiner would press the skin surface with a finger for a few seconds and observe if a dimple starts to form. Depending on the dimple depth and how long it lasts, a score of 0 (no edema) to 4 (most severe edema) is given.

Specifically, the maximum indentation depth  $d_{max}$  and recovery time (how long to recover from the indentation)  $t_{rec}$  are the two quantities of interest. From the derivation of mechanical impedance above (equation 1.4),  $d_{max}$  is proportional to  $1/k$  and  $t_{rec}$  is proportional to  $b/k$ . When edema occurs, the tissue stiffness  $k$  decreases so both  $d_{max}$  and  $t_{rec}$  increase consequently. Depending on the values of  $d_{max}$  and  $t_{rec}$ , a score of 0 (no edema) to 4 (most severe edema) is given (Figure 1.1).

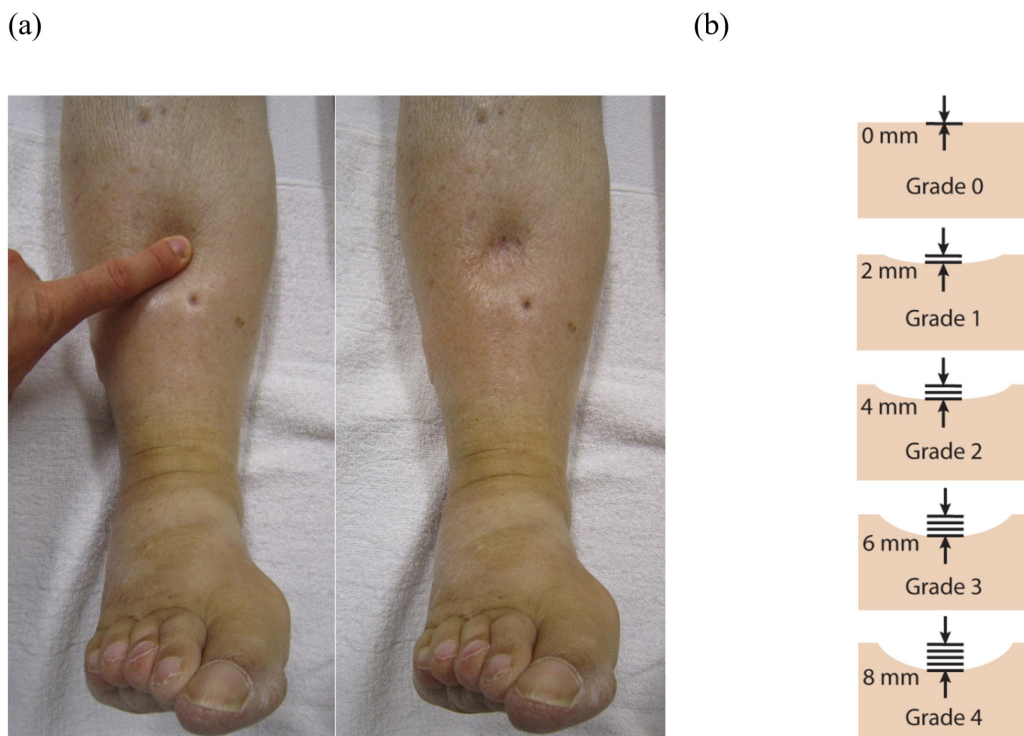


**Figure 1.1:** Semi-quantitative grading of skin edema using the pitting test. (a) Photo of pitting edema in the leg. A dimple on the skin is clearly visible after the finger press. (b) Grading of skin edema based on  $d_{max}$  is commonly used in a clinical setting. Figure (a) is reprinted under the license from Wikipedia (Heilman, 2010).

### *ULTRASOUND VISCOELASTICITY*

Ultrasound viscoelasticity imaging uses an ultrasound transducer to track the deformation at various depths in the tissue. An external force is applied to the skin surface as in the pitting test. However, the deformation is not measured with a caliper but by tracking the “speckle” patterns from the ultrasound wave reflections. Speckles are the constructive or destructive interference patterns from the superposition of reflected ultrasound waves. As the skin undergoes different degrees of deformation, nearby anatomical microstructures move together and so do the speckles. Consequently, speckle movement between two consecutive image frames approximates the deformation field and thus provides information on the depth-deformation relationship.

Ultrasound viscoelasticity imaging was proposed in a previous work as a non-invasive way to quantify skin edema (Pitre et al., 2016). The speckle tracking algorithm was applied to identify the strain field and generate tissue elastograms.

The mechanical model of the skin is a modified version of the Kelvin viscoelastic model that consists of three parameters: two elastic moduli  $E_0$  and  $E_1$ , and one viscosity constant  $\eta_1$  (Figure 1.2). In the benchtop experiments, the instantaneous elastic modulus  $E_0$  was derived from the center deformation of the tofu skin phantom. The derived value  $E_0$  was then used a constant to fit  $E_1$  and  $\eta_1$  in all other stress-strain curves at different depths. The depth-dependent stress  $\sigma(z)$  and time-dependent strain  $\epsilon(t, z)$  are given in the following equations:

$$\tau = E_1/\eta_1 \quad (1.5)$$

$$\sigma(z) = \sigma_0 \left[ \frac{z^3}{(a^2 + z^2)^{\frac{3}{2}}} - 1 \right] \quad (1.6)$$

$$\epsilon(t, z) = \sigma(z) \left[ \frac{1}{E_0} + \frac{1}{E_1} \left( 1 - e^{-\frac{t}{\tau}} \right) \right] H(t - t_0) \quad (1.7)$$

, where  $\tau$  is the viscoelastic time constant,  $\sigma_0$  is the instantaneous constant stress,  $a$  is the radius of the compressor,  $z$  is the depth, and  $H(t)$  is the Heaviside step function.

When edema occurs, the accumulation of interstitial fluid causes the microscopic mechanical properties (viscoelastic time constant  $\eta_1$  and elastic moduli  $E_0$  and  $E_1$ ) to change with extra fluid. The author used tofu as the tissue-mimicking model as tofu contains numerous tiny voids filled with saline solution. Unfortunately, the method was not tested on human subjects, so its accuracy and reliability remain unknown.



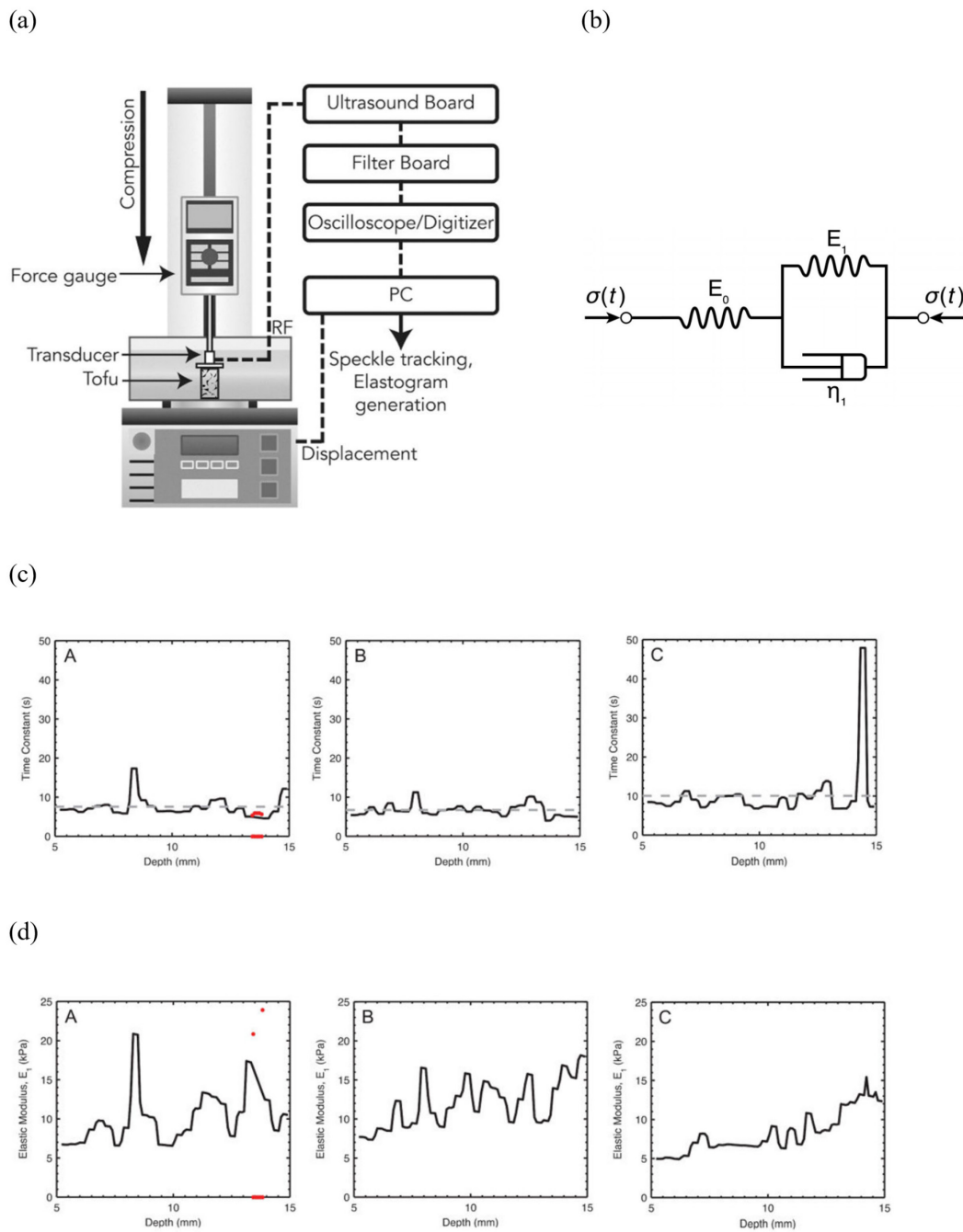


**Figure 1.2:** Ultrasound viscoelasticity imaging. (a) Experimental setup. (b) The viscoelastic model of the tofu skin phantom. (c) Measured time constant  $\tau = E_1/\eta_1$  as a function of depth. (d) Measured elastic modulus  $E_1$  in the viscoelastic model as a function of depth. For tofu skin phantom “A” in subfigures (c) and (d), the outliers with an r-squared value less than 0.9 are marked in red and so are the corresponding depth on the x-axis. The figures are reprinted with permission from Elsevier (Pitre et al., 2016).

### *ULTRASOUND ECHOGENICITY*

In addition to the ultrasound viscoelasticity imaging, there is yet another way to characterize edematous tissue with ultrasound waves. Ultrasound echogenicity measures the intensity of ultrasound echoes within a particular tissue region (corresponding to a pixel in the ultrasound image).

When an ultrasound wave hits the interface of two layered materials with different acoustic properties, part of the wave is reflected with an energy portion equal to the reflection coefficient  $R$ :

$$R = (Z_2 - Z_1)^2 / (Z_2 + Z_1)^2 \quad (1.8)$$

, where  $Z_1$  and  $Z_2$  are the acoustic impedance of the top layer (layer which the incident wave first enters) and bottom layer, respectively.

In the dermis, ultrasound reflections are generated on the surface of collagen bundles (see histology images in Figure 2.7). An influx of water into the dermis rearranges these collagen bundles to have less echogenicity. A previous study showed moderate correlation coefficients ( $r = 0.42$  for women and  $r = 0.56$  for men) between the number of low echogenic pixels (LEP) and water-to-fat (W/F) ratio in the nuclear magnetic resonance spectra and the dependency of the W/F ratio on gender (Figure 1.3).

During normal conditions, the adipose lobules in the subcutis give relatively low echogenicity compared to dermis. However, when interstitial fluid starts to flow through the intercellular space, the acoustic impedance mismatch between fat and water causes stronger ultrasound reflections. Consequently, the subcutaneous edema is visible as a brighter and more homogeneous layer in the ultrasound images (Figure 1.4).

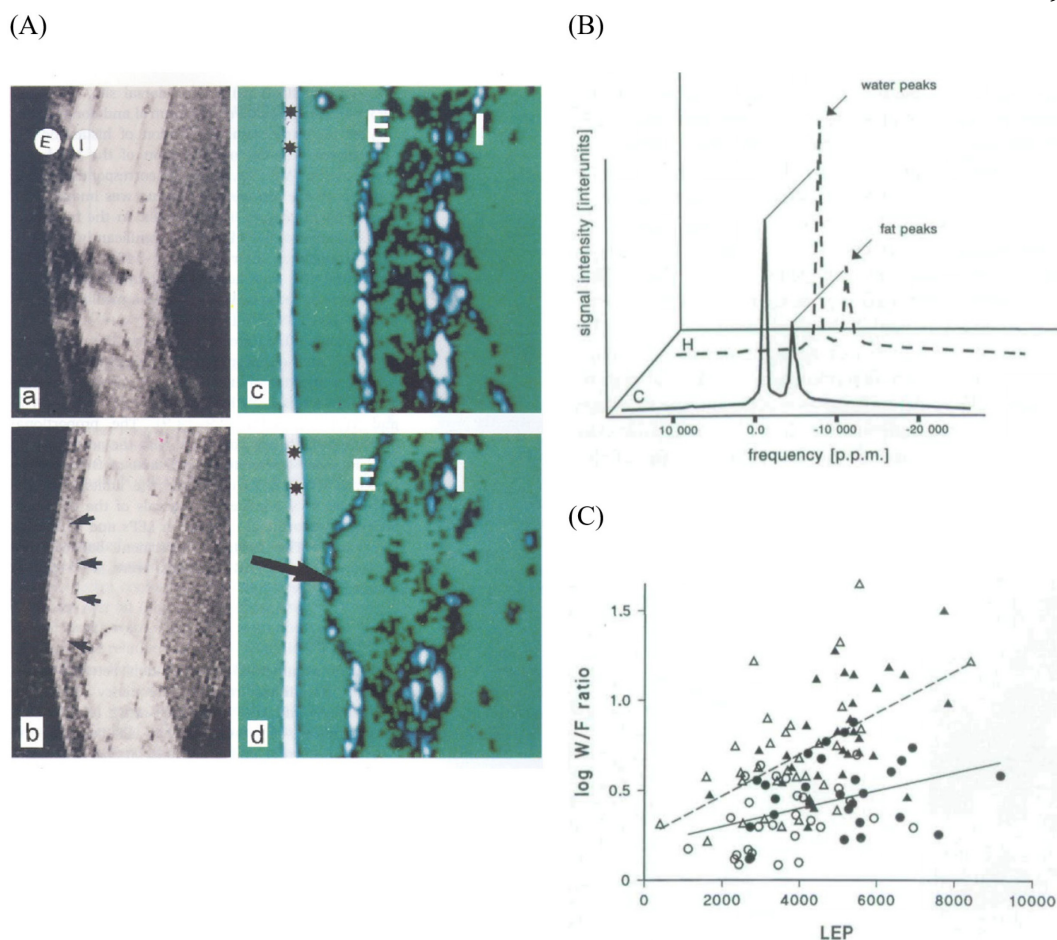


**Figure 1.3:** Ultrasound echogenicity measurements in the forearm. (A) MRI (left column) and ultrasound images (right column) showing normal skin (top row) and edematous skin (bottom row). The epidermis layer is marked by “E” and the dermis-subcutis interface is marked by “I”. Black arrows indicate the histamine injection site and local skin edema. Black asterisks indicate the surface of the ultrasound transducer. (B) NMR spectra showing water and fat peaks. Solid curve is from normal skin and dashed curve is from edematous skin. (C) the regression lines showing the correlation between the number of low echogenic pixels (LEP) and the logarithmic value of the water-to-fat ratio in the NMR spectrum taken from the edematous skin. The figures are reprinted with permission from John Wiley and Sons (Gniadecka and Quistorff, 1996).

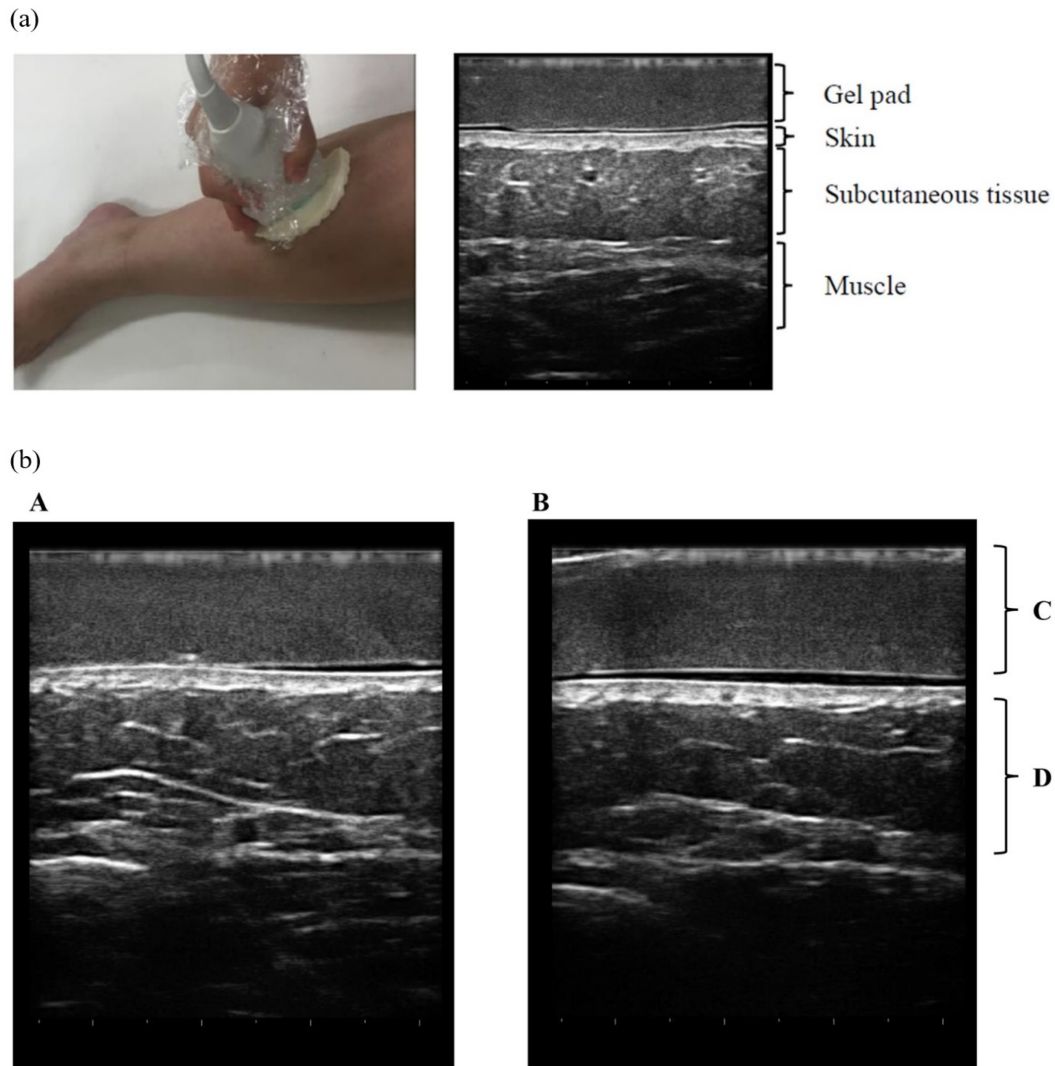


**Figure 1.4:** Ultrasound echogenicity measurements from the subcutaneous tissue in the lower legs. (a) The measurement setup including a portable ultrasound probe (left) and a custom-made gel pad on the skin surface (right). The gel pad with uniform acoustic impedance is used as the echogenicity reference for objective edema quantification. (b) Representative B-mode ultrasound images of subcutaneous edema (A) and normal skin (B) showing different levels of echogenicity compared to the gel pad reference (C) in the subcutis layer (D). Figures are reprinted under Creative Commons Attribution 4.0 International (Lu et al., 2013).

### CAPACITIVE SENSING

The hydration level of the skin can be measured by two interdigitated electrodes, which detect the change in the fringing capacitance as a function of water content (Figure 1.5). Since water has a relatively high dielectric constant of  $\sim 80$ , higher hydration level increases the magnitude of fringing capacitance compared to the baseline value from dry skin. To make the measurement more repeatable, the compressive force is controlled around 10 N as the fringing field decays to less than 30% when the separation is greater than one electrode pitch.

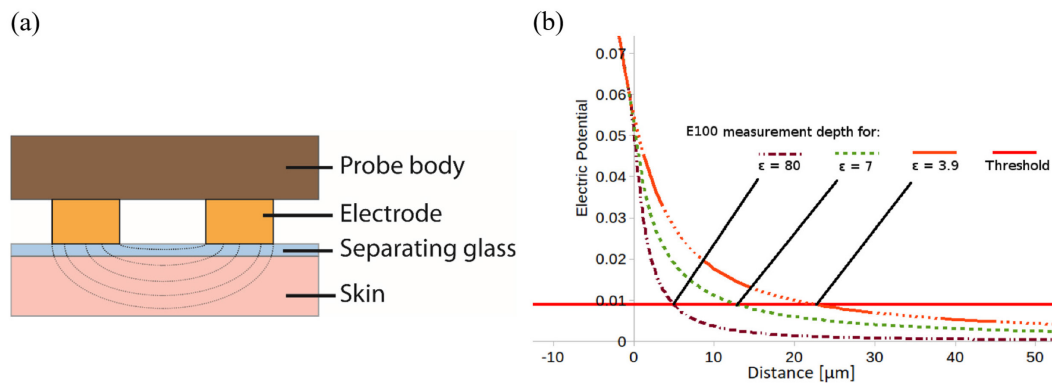


**Figure 1.5:** Capacitive sensing of dielectric constants of skin. (a) The operating principle of the capacitive skin hydration sensor uses the fringing electric field (dashed lines) to sense the changes in the skin's effective dielectric constant. (b) The simulated electric potential in the skin for a commercial capacitive skin hydration sensor (E100). Note the dependency of measurement depth on the material dielectric constant. The detection threshold is set to 0.01 V. Figures (b) and (c) are reprinted under the Creative Commons Attribution License (Bontozoglou and Xiao, 2020).

### BIOIMPEDANCE SPECTROSCOPY

The theory of bioimpedance spectroscopy is based on the single time constant model of tissue, which consists of an extracellular resistor  $R_e$ , a membrane capacitor  $C_m$ , and an intracellular resistor  $R_i$  (Allegri et al., 2017). To measure the values of these circuit components, the impedance spectrum over a wide range of frequencies is obtained and fitted by the Cole-Cole dispersion curves (Figure 1.6).

The Cole-Cole model consists of an array of resistors and capacitors as the equivalent electrical circuit of the body. At low frequencies (below 50 kHz), the current cannot pass the insulating membrane capacitor  $C_m$  and flows completely around the cell through extracellular resistor  $R_e$ . At higher frequencies (above 50 kHz), the current partially passes the membrane capacitor and flows through the intracellular resistor  $R_i$ . The Cole-Cole “0” resistor  $R_0$  and “ $\infty$ ” resistor  $R_\infty$  correspond to the equivalent resistance of the Cole-Cole model at DC and infinite frequency, respectively. They have demonstrated to better correlate with the intracellular fluid volume and the extracellular fluid volume.

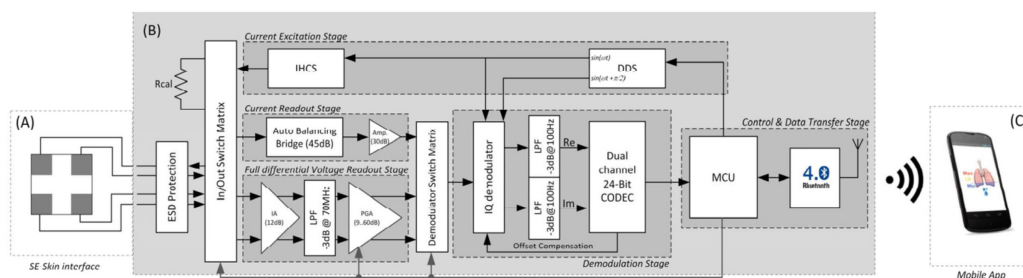
In practice, a spectrum of frequencies between 10 kHz and 1 MHz are used to fit the Cole-Cole model elements  $R_0$ ,  $R_\infty$  and  $C_1$  by nonlinear, least-squares analysis. Then, a circuit transformation is applied to obtain  $R_e$ ,  $R_i$  and  $C_m$ . The circuit transformation equations are

$$R_e = R_0 \quad (1.9)$$

$$R_i = \frac{R_\infty R_0}{R_0 - R_\infty} \quad (1.10)$$

$$C_m = \frac{(R_0 - R_\infty)^2}{R_0^2} C_1 \quad (1.11)$$

(a)



(b)

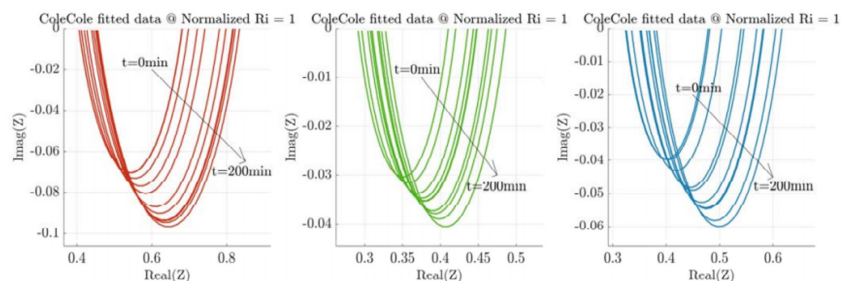


**Figure 1.6:** Bioimpedance spectroscopy. (a) The block diagram of the multi-frequency bioimpedance spectroscopy sensor showing the 4-electrode skin interface (A), sensing electronics (B), and mobile app (C) that collects and transmits data wirelessly. (b) The fitted impedance loci from Cole-Cole dispersion model over time. The “hydration factor”  $H$  as a function of time is derived as the ratio  $R_e/R_i$  (see context for derivations). Figures are reprinted with permission (Allegrì et al., 2017). © 2017, IEEE.

### EDDY CURRENT METHOD

The eddy current method uses a magnetic coil to generate alternating magnetic field to look for induced “eddy currents” inside the field and mathematically the whole system of a coil and eddy-current-generating materials in a 3D space can be accurately calculated by Maxwell’s equations. In theory, any conductive material will induce eddy currents except that edema induces much smaller eddy currents due to its low conductivity ( $2 \text{ S/m}$ ) compared to that of metals ( $\sim 10^7 \text{ S/m}$ ).

When edema occurs, the interstitial fluid content is expected to increase due to fluid accumulation in the extracellular space. The equivalent skin conductivity is assumed to follow Maxwell's mixing formula, which is a nonlinear combination of the average skin conductivity and the interstitial fluid conductivity.

The eddy current method is particularly advantageous for continuous, noninvasive monitoring of skin edema. The advantages include (1) the skin is located at the body surface and is easy to access, (2) the maximum inductive damping occurs at the outmost boundary of the conductive region, which happens to coincide with the skin, (3) other methods like ultrasonography and capacitive sensing can provide the necessary depth and volume information needed to convert the total inductive loss to skin conductivity.

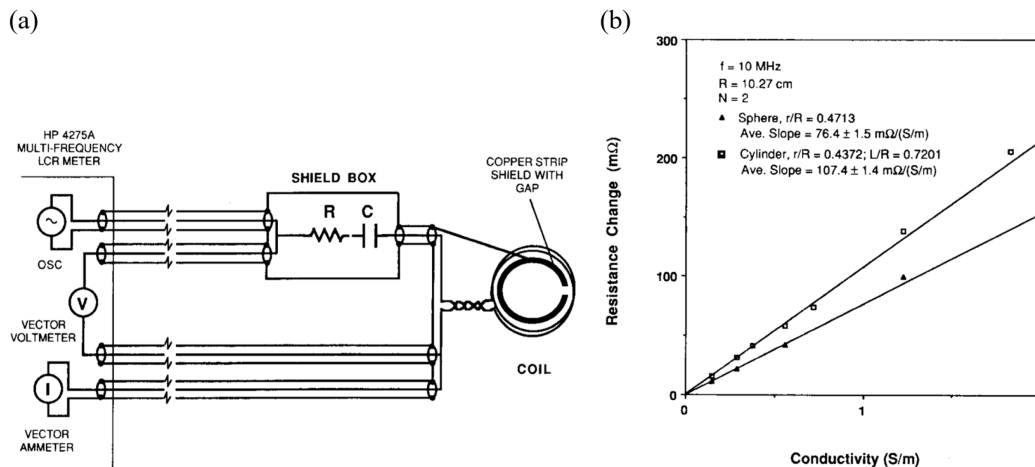


**Figure 1.7:** The eddy current method for measuring tissue conductivity. (a) Noninvasive conductivity sensor based on serial RLC resonant circuit with gapped ground shielding. (b) Coil resistance change versus conductivity in the target. The figures are reprinted with permission (Hart et al., 1988). © 1988, IEEE.



### *B-MODE ULTRASONOGRAPHY*

B-mode ultrasonography provides a direct measurement of skin thickness and structural dimensions. When edema occurs, subcutis layer thickens as interstitial fluid accumulates and stretches the connective tissue.

In a previous clinical study, pregnant women subjects are scanned with a B-mode ultrasound probe (5 MHz) for leg edema. The measurement site is located at 6 cm from the upper part of the medial malleolus and 1 cm inside the anterior border of the tibia. This measurement site was chosen because few other structures exist between the skin and bone other than a thin portion of the soleus muscle. The skin thickness is obtained by detecting the boundary between the dermis and fascia with the help of the human subjects stretching their legs (Figure 1.8).

The measurement procedure is as follows (Yanagisawa et al., 2019):

“When the skin thickness was being measured, the women repeatedly performed anteflexion and retroflexion of the ankle. Because the skin thickness measurements included the epidermis, dermis, and subcutaneous layers above the fascia and muscle, movements of the ankle resulted in the movement of the fascia and muscle layers, but not the skin, which allowed identification of the skin layer.”

According to the study, the correlation between the degree of pitting edema and skin thickness is statistically significant ( $\rho = 0.56$ ,  $p < 0.0001$ ). The same study also compared the method's sensitivity on obese versus non-obese subjects. The results suggested statistical significance within the non-obese group ( $p < 0.0001$ ). However, when it comes to the obese group, the p value increases to 0.02 within the group. This result suggests no statistical significance exists between the non-obese group with edema and the obese group without edema. Therefore, without knowing a prior whether a subject is obese or not, it is statistically unlikely to diagnose the edema with the increase of skin thickness alone.

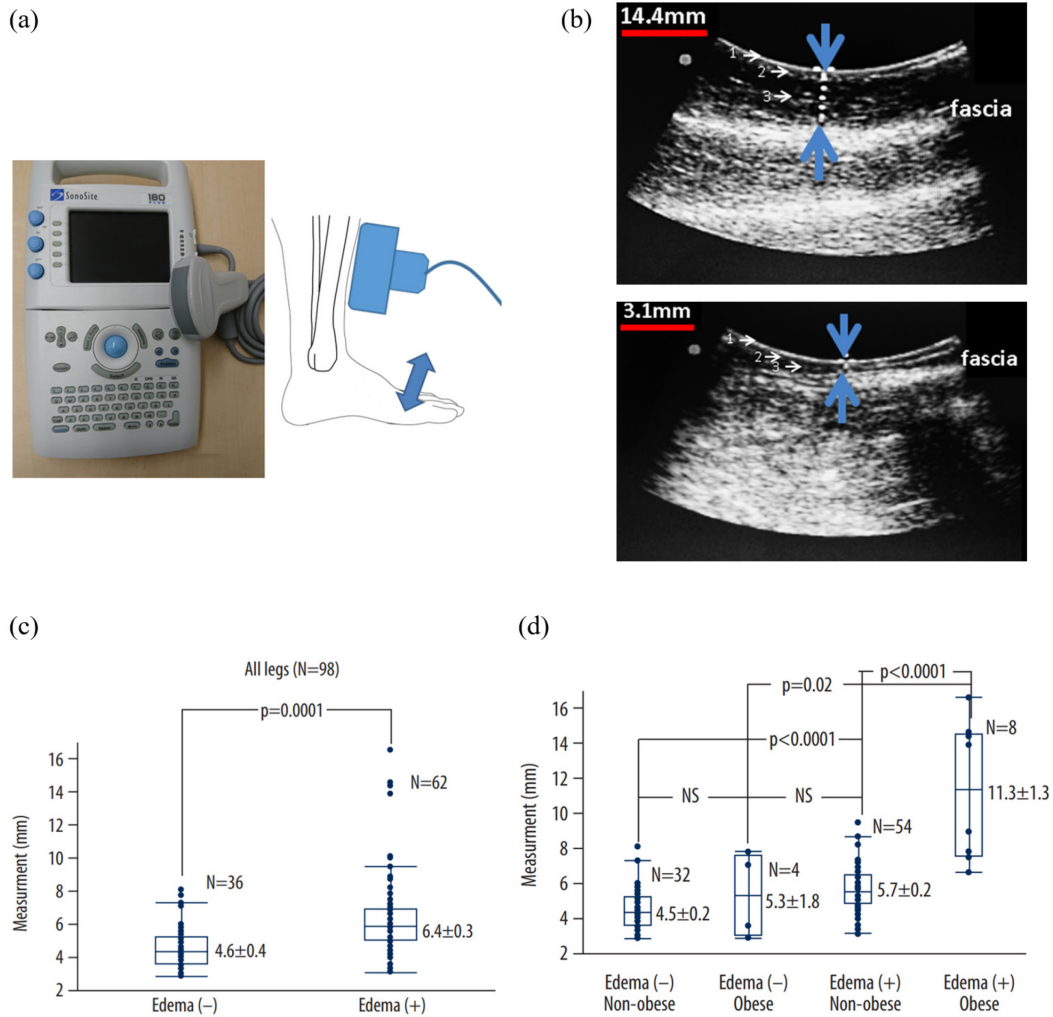


**Figure 1.8:** B-mode ultrasonography study on the correlation between skin thickness and lower leg edema. (a) SonoSite 5 MHz convex array ultrasound probe used in the study and the schematic drawing showing the measurement location. (b) B-mode ultrasonography showing the thickness of normal skin (top) and the edematous skin (bottom). The blue arrows indicate the start and end of the skin section, which includes epidermis (marked by “1”), dermis (marked by “2”), and subcutaneous fat (marked by “3”). The measured skin thickness is on the top left. (c) Overall skin thickness data including both the obese and non-obese groups. (d) Skin thickness data separating the two groups. The figures are reprinted under the Creative Common Attribution-NonCommercial-NoDerivatives 4.0 International (Yanagisawa et al., 2019).

### MAGNETOMETER ANKLE CIRCUMFERENCE SENSOR

The ankle circumference sensor consists of a ferrite-core inductor and two magnetometers on the opposite sides of the inductor (Zhang and Rajamani, 2015).. The magnetometers measure the static magnetic field generated by the inductor, compare them with the theoretical values, and obtain the change in the ankle circumference. As demonstrated in the benchtop experiments, the sensor has a resolution of less than 1 mm and an accuracy of 0.5 mm among 10 test runs (Figure 1.9). The out-of-plane movement of the magnetometers were also characterized and regarded as not significant when compared to the primary in-plane stretching.

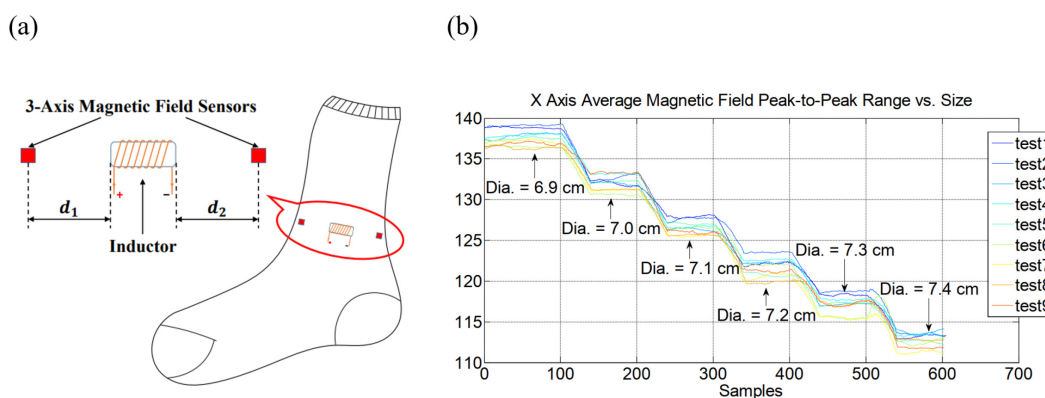


**Figure 1.9:** Magnetometer-based ankle circumference sensor (a) Schematic drawing of the sensor. The inductor generates a static magnetic field that is measured by two 3-axis magnetometers located on the opposite sides. (b) Sensor band readout versus different ankle diameters and test runs, showing the accuracy and reliability of the sensor. The figures are reprinted with permission (Zhang and Rajamani, 2015). © 2015, IEEE.

### OPTICAL LIMB VOLUMETRY

This category includes near-infrared (NIR) perometry and 3-D depth imaging, both of which give out measures of the limb volume by either integrating individual cross-sectional area or obtaining depth information from the limb surface (Figure 1.10).

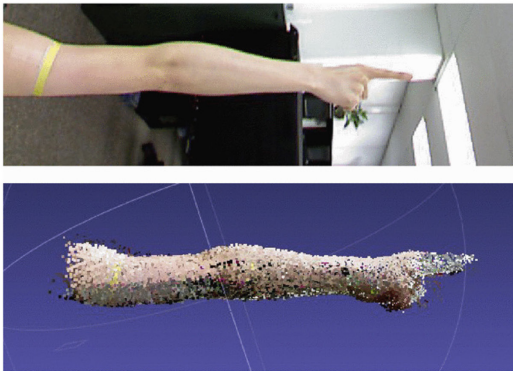
The perometer emits NIR beams from an array of transmitters and counts how many receivers detect a signal on the other side of the scanner. The 2-D heatmap reconstructed from the receiver signals approximates the cross-section area of the

limb as NIR beams are easily blocked by the presence of limb. The perometer then moves along the longitudinal direction and obtains the cross-sectional area of the next slice. By multiplying the area by the step size and summing over the entire length of the limb, the total limb volume is obtained.

(a)



(b)



(c)

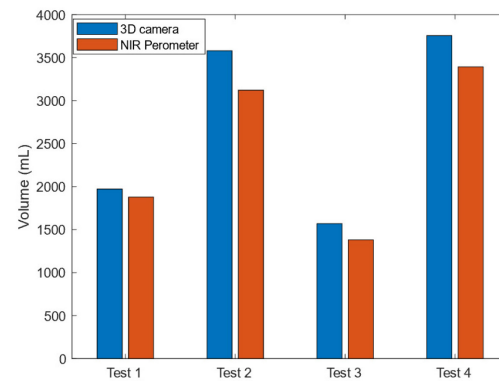


**Figure 1.10:** Comparison of two optical limb volume measurement methods. (a) Photos showing the near-infrared optical volumetry that uses an optical scanner to obtain the cross-sectional area at each limb slice (left) and the 3-D depth volumetry that uses a 3-D camera to obtain the depth information from the limb surface (right). (b) Optical image showing a human forearm and the reconstructed limb from the 3-D depth information. (c) Comparison of limb volume measured by the two methods. Note that the limb volume estimated by the 3-D camera is always higher than that measured by the perometer. Figures (a) and (b) are reprinted with permission (Lu et al., 2013). © 2013, IEEE.

*NEAR-INFRARED SPECTROSCOPY*

The near-infrared spectroscopy detects the unique water absorption peaks when skin edema is present (Stamatas et al., 2006). A multispectral camera takes several images of the same skin area at different wavelengths (Figure 1.11), then the acquired reflectance spectrum is used to fit the extinction coefficients of the chromophores for each pixel. Since different chromophores have their own extinction coefficient as a function of frequency, the spectral images can be transformed into a concentration map of a specific chromophore (for example, oxyhemoglobin). After baseline subtraction, the apparent skin edema severity is obtained in terms of water intensity. The measured edema severity is proportional to the dosage of histamine, the drug that was used to induce skin edema (Figure 1.12).

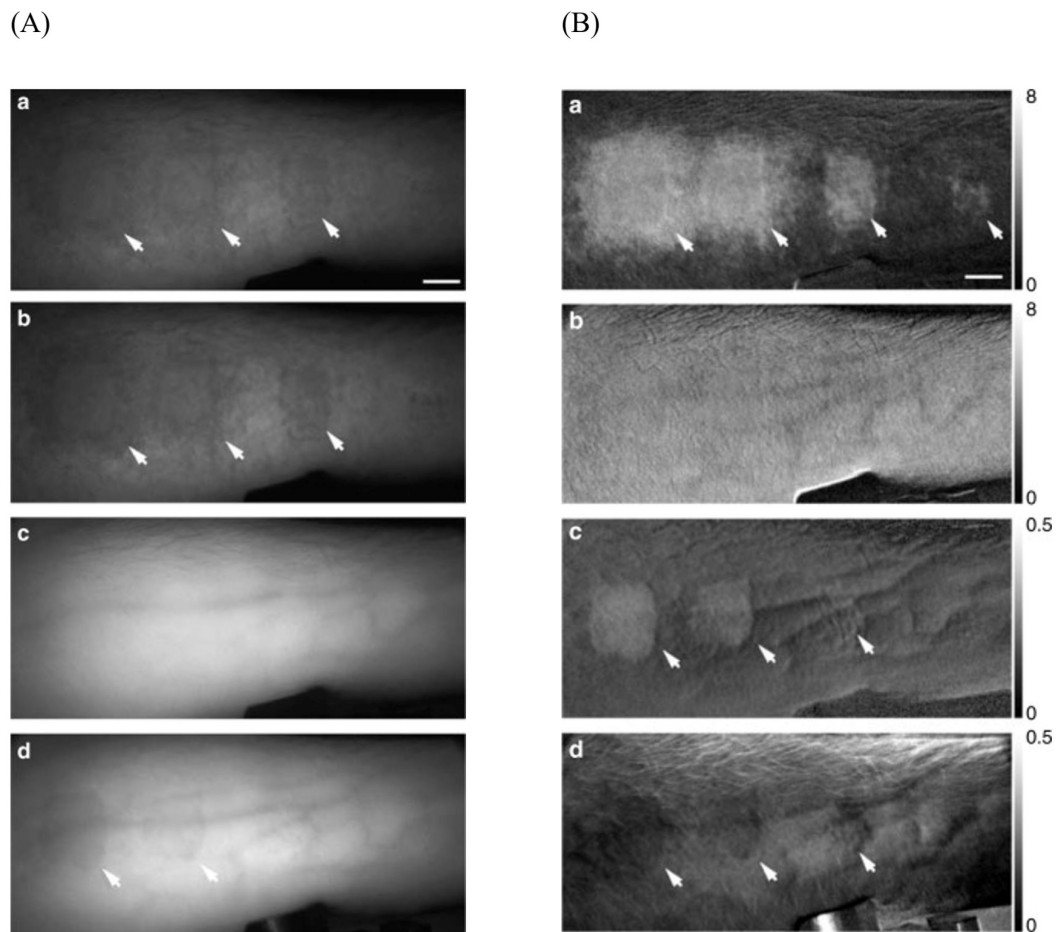


**Figure 1.11:** Near-infrared spectroscopy imaging. (A) Multispectral images of the skin at 560 nm (a), 580 nm (b), 700 nm (c), and 970 nm (d). Skin erythema is visible in (a)(b) due to strong hemoglobin absorption, while skin edema is identified in (d) due to excess water absorption at histamine injection sites (indicated by white arrows). (B) Concentration maps of different chromophores including oxy-hemoglobin (a), deoxy-hemoglobin (b), water (c), and collagen fibers (d). The injection sites are indicated by white arrows. Figures are reprinted with permission (Stamatas et al., 2006).

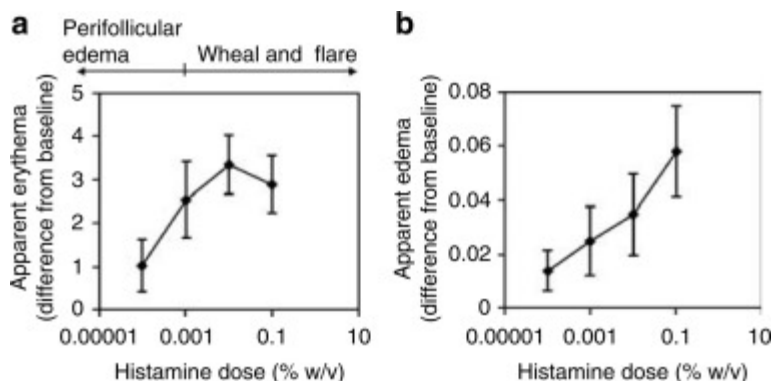


**Figure 1.12:** The apparent erythema and skin edema indices. They are derived from the concentration of oxy-hemoglobin (a) and water (b), respectively. Figures are reprinted with permission (Stamatas et al., 2006).

### THERMAL DIFFUSIVITY

The thermal diffusivity skin hydration sensor uses a resistive heater as the heat source and a thermistor as the temperature sensor (Madhvapathy et al., 2020). Depending on the water content in the epidermis and dermis, the equivalent thermal conductivity  $k$  and thermal diffusivity  $\alpha$  change accordingly:

$$p = \frac{k_W}{k_{dry}} \quad (1.12)$$

$$\frac{k_E}{k_{dry}} = \frac{(p + 2) + 2(p - 1)\phi_E}{(p + 2) - (p - 1)\phi_E} \quad (1.13)$$

$$\frac{\alpha_E}{\alpha_{dry}} = \frac{\alpha_W k_E}{(1 - \phi_E)\alpha_W k_{dry} + \phi_E \alpha_{dry} k_W} \quad (1.14)$$

, where  $k_E$  and  $\alpha_E$  are the thermal conductivity and diffusivity of the epidermis,  $k_{dry}$  and  $\alpha_{dry}$  are the thermal conductivity and diffusivity of the dry skin,  $k_W$  and  $\alpha_W$  are the thermal conductivity and diffusivity of water, and  $\phi_E$  is the volumetric epidermal water content (Figure 1.13).

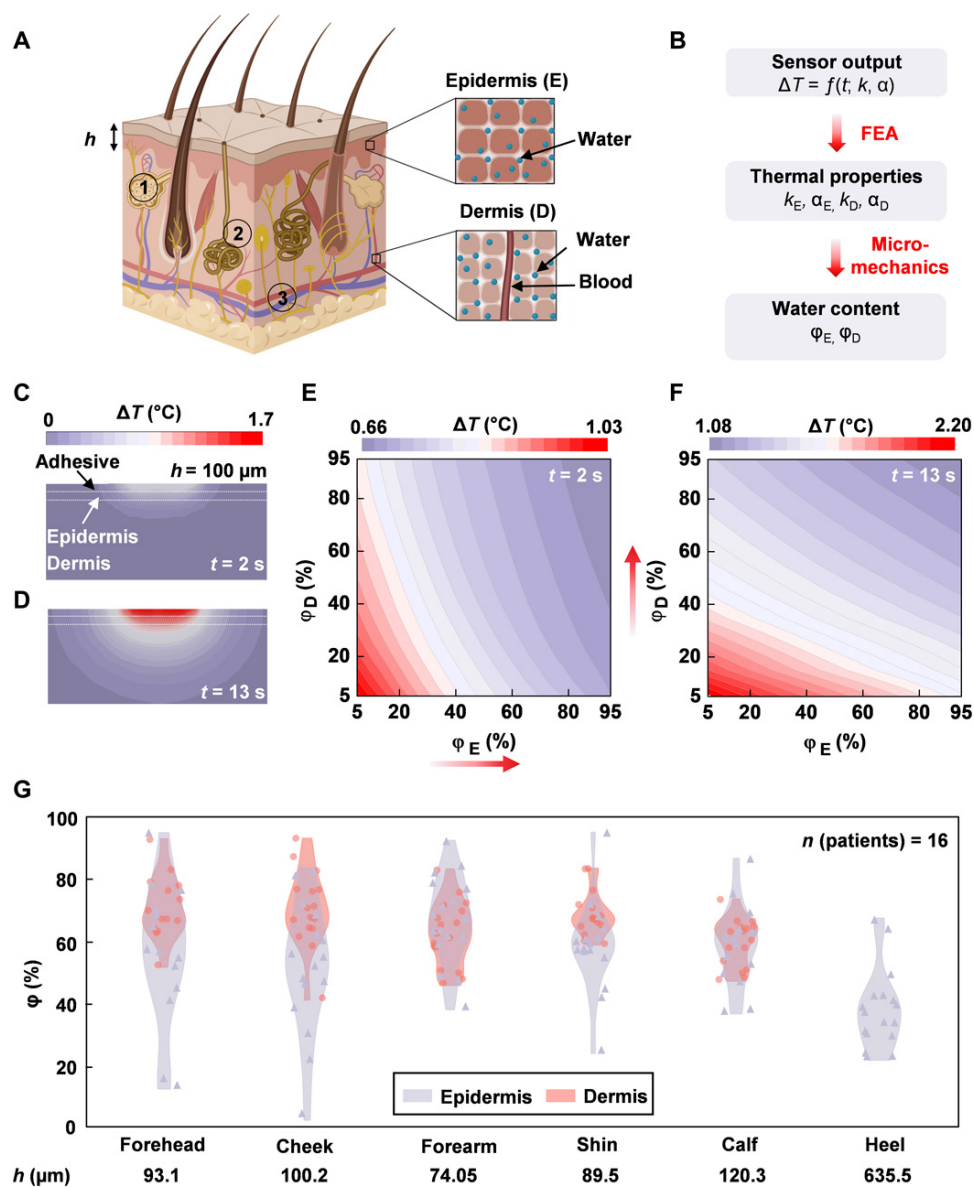


**Figure 1.13:** Thermal diffusivity skin hydration sensor. (A) Cross-sectional view of the skin that includes sebaceous glands (1), eccrine sweat glands (2), blood vessels (3), epidermis, and dermis. (B) Flow chart that shows the conversion from temperature sensor readings to the water content in epidermis and dermis. (C)(D) Simulated temperature profiles showing the heat transfer into the dermis after 2 seconds and 13 seconds. (E)(F) The dependency of temperature change on epidermis and dermis water content. (G) Measured epidermis and dermis water content at various body locations. Figures are reprinted with permission (Madhvapathy et al., 2020).



### MAGNETIC RESONANCE IMAGING

The magnetic resonance imaging (MRI) has been widely used to quantify the tissue water and lipid content by the nuclear properties of the hydrogen atoms in the water or lipid molecule. Since the magnetic resonance frequency or “chemical shift” depends on the surrounding environment, the mapping of nuclei distribution at a particular chemical shift can be associated with a particular molecular group (Brateman, 1986). In the case of skin edema, the tissue water and fatty acid lipid distributions show the locations where ISF accumulates and the associated structural changes (Figure 1.14). The T1 and T2 relaxations times also change significantly during the occurrence of edema (Idy-Peretti et al., 1998).

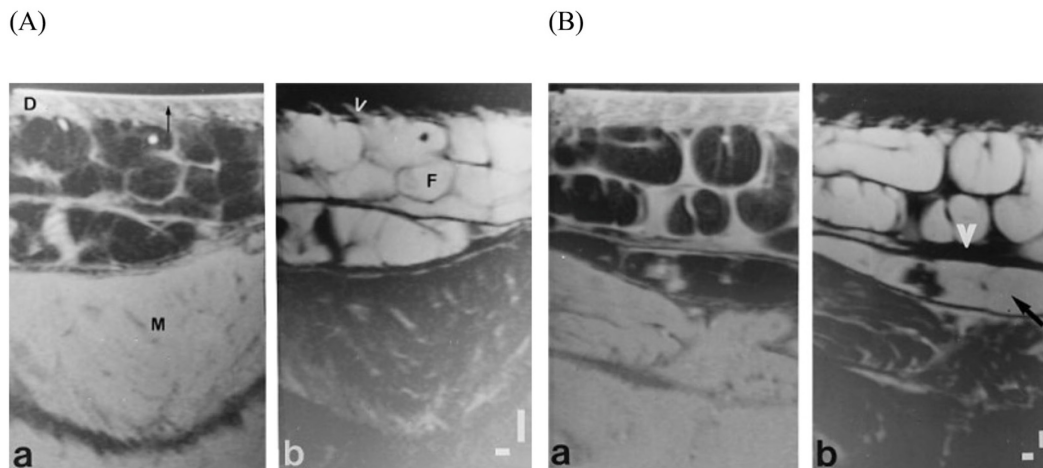


**Figure 1.14:** Magnetic resonance imaging for skin edema quantification. High resolution chemical shift magnetic resonance images (A) showing water content (a) and fat content (b) of a normal leg, and (B) showing water content (a) and fat content (b) of a leg with lymphedema. Scale bars are 1 mm. D = dermis, M = muscle, F = fatty tissue. Figures are reprinted with permission (Idy-Peretti et al., 1998).

### 1.3 PREVIOUS WORKS ON SKIN EDEMA QUANTIFICATION

The mechanical impedance and ultrasound viscoelasticity methods mimic the standard pitting test and allow direct comparison with clinical evaluation results. However, they require external force actuators and sensors to quantify how much the skin is compressed. The extra mechanical components may not be portable enough for continuous monitoring of skin edema, and they usually consume much more power. The standard pitting test is quick and easy to conduct, but it requires professional personnel to do the manual palpation. Otherwise, the maximum applied pressure and duration of palpation may not be consistent among examiners to meet the standards (Sanderson et al., 2015). The ultrasound echogenicity can be measured by a portable ultrasound probe which allows continuous measurements. However, the correlation coefficient with MRI (for measurements in the dermis) and the statistical significance p-value (for measurements in the subcutis) were not high enough.

For methods based on electrical properties, capacitive sensing uses the fringing electric field to detect changes in the dielectric constant. Therefore, it is not only sensitive to the vertical displacement but also limited in penetration depth. More importantly, because the sensor cannot distinguish conduction currents from displacement currents, the capacitive sensor will respond to both conducting and non-conducting materials.

Methods based on measuring the geometric dimensions of the skin are often highly repeatable because they require minimal contact with the skin. B-mode ultrasonography can even selectively measure the subcutis thickness with an accuracy on the order of 1 mm. However, they suffer from the non-specific problem that the change in limb size does not necessarily imply edema formation.

The pros and cons from different quantitative methods discussed in the previous sections are listed in the table below for comparison:

**Table 1.1:** Summary of current non-invasive quantitative methods to detect skin edema.

| Category         | MECHANICAL PROPERTIES |              |                            |                         | ELECTRICAL PROPERTIES |                           |              |
|------------------|-----------------------|--------------|----------------------------|-------------------------|-----------------------|---------------------------|--------------|
| <b>Method</b>    | Mechanical impedance  | Pitting test | Ultrasound viscoelasticity | Ultrasound echogenicity | Capacitive sensing    | Bioimpedance spectroscopy | Eddy current |
| Sensitivity      | High                  | Middle       | High                       | Middle                  | High                  | High                      | Middle       |
| Accuracy         | Middle                | Middle       | Middle                     | High                    | Middle                | Middle                    | High         |
| Cost             | Low                   | Low          | Middle                     | Middle                  | Low                   | Low                       | Low          |
| Manual operation | Yes                   | Yes          | No                         | Yes                     | Yes                   | No                        | No           |
| Wearable device  | No                    | No           | No                         | No                      | No                    | Yes                       | No           |

| Category         | GEOMETRIC DIMENSIONS   |   |                        | OPTICAL PROPERTIES         | THERMAL PROPERTIES  | OTHER PROPERTIES           |
|------------------|------------------------|---|------------------------|----------------------------|---------------------|----------------------------|
| <b>Method</b>    | B-mode ultrasonography | Magnetometer ankle circumference sensor | Optical limb volumetry | Near-infrared spectroscopy | Thermal diffusivity | Magnetic resonance imaging |
| Sensitivity      | Middle                 | Middle                                  | Middle                 | High                       | High                | High                       |
| Accuracy         | High                   | High                                    | High                   | High                       | Middle              | High                       |
| Cost             | Middle                 | Low                                     | Middle                 | Middle                     | Low                 | High                       |
| Manual operation | Yes                    | No                                      | Yes                    | No                         | No                  | Yes                        |
| Wearable device  | No                     | Yes                                     | No                     | No                         | Yes                 | No                         |

## 1.4 THESIS OUTLINE

This thesis tries to improve existing methods by proposing a novel wearable sensor that better detects skin edema in its early stage. Specifically, the device utilizes the eddy current method to measure the effective skin conductivity, and a skin edema model is established to link the skin conductivity to the interstitial fluid volume fraction. The latter is regarded as an objective measurement of skin edema severity.

I will address the challenges mentioned in the previous section and solve the problem of continuous and accurate measurements of skin edema in the following steps:

1. I summarized previous works on noninvasive methods to quantify skin edema, compared the pros and cons of different methods, and discussed what needs to be improved in Chapter 1.
2. To better understand skin edema quantification, I will review the structure of human skin anatomy and the pathological causes of skin edema in Chapter 2.
3. To solve challenges in skin edema quantification, I will propose a wearable sensor based on the eddy current method and a skin conductivity model that characterizes skin edema by the interstitial fluid volume fraction in Chapter 3.
4. I will describe the electronic circuit and electromagnetic theory behind the proposed sensor and procedures to design and optimize the sensor in Chapter 4.
5. To verify the sensor design, I will provide simulation and experimental results of the first prototype sensor in Chapter 5.
6. Based on the results from the first prototype sensor, I will show how to further improve the sensor performance with magnetic shielding in Chapter 6.
7. I will summarize the thesis with conclusion and future works in Chapter 7.

## 1.5 REFERENCES

- Allegri, D., Vaca, D., Ferreira, D., Rogantini, M., Barrettino, D., 2017. Real-time monitoring of the hydration level by multi-frequency bioimpedance spectroscopy, in: 2017 IEEE International Instrumentation and Measurement Technology Conference (I2MTC). Presented at the 2017 IEEE International Instrumentation and Measurement Technology Conference (I2MTC), pp. 1–6. <https://doi.org/10.1109/I2MTC.2017.7969668>
- Bontozoglou, C., Xiao, P., 2020. Applications of Capacitive Imaging in Human Skin Texture and Hair Analysis. *Applied Sciences* 10, 256. <https://doi.org/10.3390/app10010256>
- Brateman, L., 1986. Chemical shift imaging: a review. *American Journal of Roentgenology* 146, 971–980. <https://doi.org/10.2214/ajr.146.5.971>
- Cho, S., Atwood, J.E., 2002. Peripheral edema. *Am J Med* 113, 580–586. [https://doi.org/10.1016/s0002-9343\(02\)01322-0](https://doi.org/10.1016/s0002-9343(02)01322-0)
- Gniadecka, M., Quistorff, B., 1996. Assessment of dermal water by high-frequency ultrasound: comparative studies with nuclear magnetic resonance. *British Journal of Dermatology* 135, 218–224. <https://doi.org/10.1111/j.1365-2133.1996.tb01150.x>
- Hart, L.W., Ko, H.W., Meyer, J.H., Vasholz, D.P., Joseph, R.I., 1988. A noninvasive electromagnetic conductivity sensor for biomedical applications. *IEEE Trans. Biomed. Eng.* 35, 1011–1022. <https://doi.org/10.1109/10.8686>
- Heilman, J., 2010. Pitting edema during and after the application of pressure to the skin. Wikimedia Commons.
- Idy-Peretti, I., Bittoun, J., Alliot, F.A., Richard, S.B., Querleux, B.G., Cluzan, R.V., 1998. Lymphedematous skin and subcutis: in vivo high resolution magnetic resonance imaging evaluation. *J Invest Dermatol* 110, 782–787. <https://doi.org/10.1046/j.1523-1747.1998.00184.x>
- Lu, G., DeSouza, G.N., Armer, J., Anderson, B., Shyu, C.-R., 2013. A system for limb-volume measurement using 3D models from an infrared depth sensor, in: 2013 IEEE Symposium on Computational Intelligence in Healthcare and E-Health (CICARE). Presented at the 2013 IEEE Symposium on Computational Intelligence in Healthcare and e-health (CICARE), pp. 64–69. <https://doi.org/10.1109/CICARE.2013.6583070>
- Madhvapathy, S.R., Wang, H., Kong, J., Zhang, M., Lee, J.Y., Park, J.B., Jang, H., Xie, Z., Cao, J., Avila, R., Wei, C., D'Angelo, V., Zhu, J., Chung, H.U., Coughlin, S., Patel, M., Winograd, J., Lim, J., Banks, A., Xu, S., Huang, Y., Rogers, J.A., 2020. Reliable, low-cost, fully integrated hydration sensors for

- monitoring and diagnosis of inflammatory skin diseases in any environment. *Sci Adv* 6, eabd7146. <https://doi.org/10.1126/sciadv.abd7146>
- Mridha, M., Odman, S., 1985. Characterization of subcutaneous edema by mechanical impedance measurements. *J Invest Dermatol* 85, 575–578. <https://doi.org/10.1111/1523-1747.ep12283588>
- Pitre, J.J., Koziol, L.B., Kruger, G.H., Vollmer, A., Ophir, J., Ammann, J.-J., Weitzel, W.F., Bull, J.L., 2016. Design and Testing of a Single-Element Ultrasound Viscoelastography System for Point-of-Care Edema Quantification. *Ultrasound in Medicine & Biology* 42, 2209–2219. <https://doi.org/10.1016/j.ultrasmedbio.2016.04.013>
- Sanderson, J., Tuttle, N., Box, R., Reul-Hirche, H.M., Laakso, E.-L., 2015. THE PITTING TEST: AN INVESTIGATION OF AN UNSTANDARDIZED ASSESSMENT OF LYMPHEDEMA. *Lymphology* 48, 175–183.
- Scallan, J., Huxley, V.H., Korthuis, R.J., 2010. Capillary Fluid Exchange: Regulation, Functions, and Pathology. *Colloquium Series on Integrated Systems Physiology: From Molecule to Function* 2, 1–94. <https://doi.org/10.4199/C00006ED1V01Y201002ISP003>
- Stamatas, G.N., Southall, M., Kollias, N., 2006. In vivo monitoring of cutaneous edema using spectral imaging in the visible and near infrared. *J Invest Dermatol* 126, 1753–1760. <https://doi.org/10.1038/sj.jid.5700329>
- Yanagisawa, N., Koshiyama, M., Watanabe, Y., Sato, S., Sakamoto, S., 2019. A Quantitative Method to Measure Skin Thickness in Leg Edema in Pregnant Women Using B-Scan Portable Ultrasonography: A Comparison Between Obese and Non-Obese Women. *Med Sci Monit* 25, 1–9. <https://doi.org/10.12659/MSM.911799>
- Zhang, S., Rajamani, R., 2015. Sensors on instrumented socks for detection of lower leg edema--An in vitro study. *Annu Int Conf IEEE Eng Med Biol Soc* 2015, 3153–3156. <https://doi.org/10.1109/EMBC.2015.7319061>

*Chapter 2***SKIN ANATOMY, EDEMA PATHOLOGY, AND  
INTERSTITIAL FLUID MODEL**

The first goal of this chapter is to provide an overview of the skin structure and a quantitative description of the fluid balance in the skin. The second goal is to relate skin edema to measurable quantities like the thickness change and interstitial fluid volume fraction, both of which play a major role in the interstitial fluid model that will appear at the end of this chapter. To facilitate the discussion, I will briefly review the human skin anatomy to give the reader a better sense of where edema occurs and how edema affects the microcirculation in the skin. A quantitative description of the microcirculation is given by the revised Starling's equation. Then I will discuss the pathological causes of edema formation by looking at individual components in the Starling's equation. I will also present the pathological findings from the B-mode ultrasonography and tissue histology. Finally, I will propose an interstitial fluid model that converts the interstitial fluid volume fraction to skin conductivity.

**2.1 HUMAN SKIN ANATOMY***MACROSCOPIC STRUCTURES OF THE SKIN – EPIDERMIS, DERMIS, AND  
SUBCUTANEOUS SPACE*

Skin is the largest organ in the human body responsible for protection, regulation, and sensation. Since edema is a direct indication of fluid accumulation in the tissue, I will focus on the regulation of interstitial fluid under normal physiological conditions and during the occurrence of edema. I will facilitate the discussion in the following sections by showing how the anatomical structures (both macroscopic and microscopic) of the skin are related to edema formation.

The human skin consists of three major layers: the thin epidermis without blood vessels, the dermis where tiny capillaries terminate and form a mesh network (the superficial arteriovenous plexus), and the subcutis containing adipose tissue lobules and larger blood vessels (Figure 2.1). The lymphatic vessels in the dermis and subcutis help circulate the interstitial fluid back to the heart. Note that unlike the normal way to define skin as a two-layer structure consisting of only the epidermis and dermis, I will include the subcutis layer in the skin for its role in edema formation. In other words, I will treat the subcutis as part of the skin in the remaining context, so there are three layers in the skin (epidermis, dermis, and subcutis).

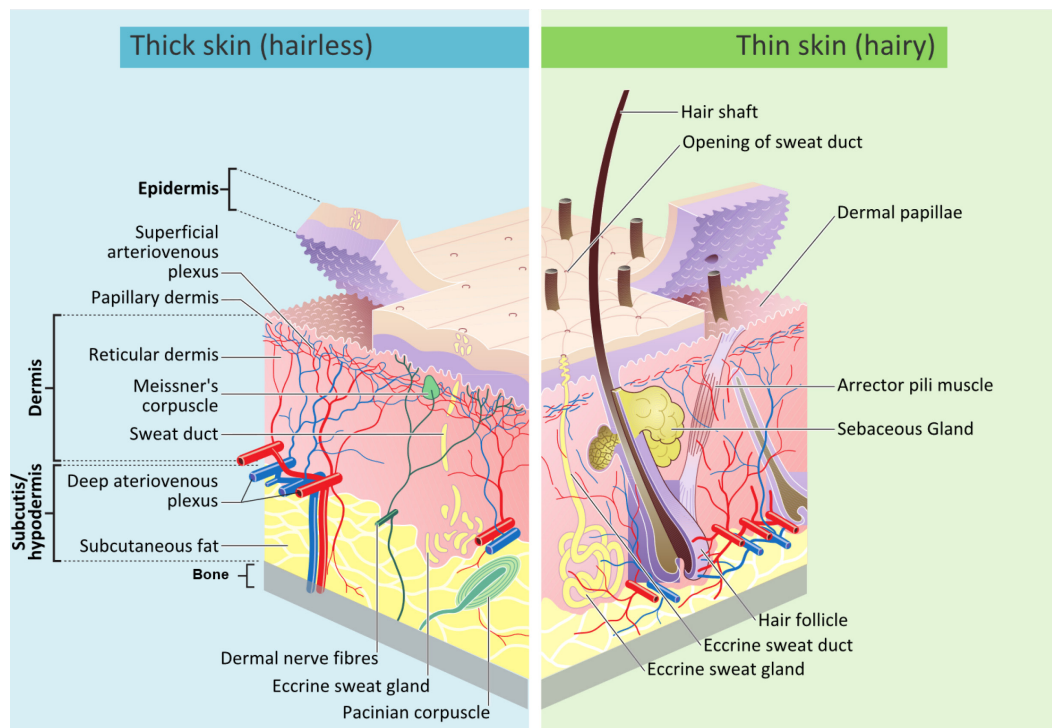


**Figure 2.1:** Cross-section view of the human skin showing the macroscopic four-layer structure (the epidermis, dermis, subcutis/hypodermis, and bone in **bold** text) and microscopic components in the thick, hairless skin (left) and thin, hairy skin (right). Figure is licensed from Wikipedia and remixed with the addition of the bone layer (Komorniczak and Madhero88, 2012).



The electrical conductivities of the three major layers in the skin can be adequately described by the following sentence (Kruglikov, 2015): “From an electrical point of view, the skin has a sandwich structure with its outmost (stratum corneum, SC) and inmost (subcutaneous white adipose tissue, sWAT) layers having electrical conductivities which are much less than that of the middle (dermis) layer.” In this study, however, the skin remains dry during the measurement. Therefore, I will use the dry epidermis/skin data in the literature for theoretical calculations and simulations.

The outer-most layer of the epidermis is the cornified layer (stratum corneum) that lacks the necessary ionic components to conduct electrical currents. The cornified cells are rich in keratin and embedded in a matrix of ceramides, cholesterol, and fatty acids. The keratin molecule absorbs water in a humid environment (for example, after taking a shower) and affects the dielectric constant of the epidermis accordingly.

The dermis consists of mainly collagen bundles (visible as strands in the microscopic images from skin biopsy). Numerous arterioles and venules exist between these bundles that supply and reabsorb blood plasma. Lymph vessels also exist to help drain extra interstitial fluid to complete the dermal micro-circulation. The revised Starling equation (equation 2.1) describes the relationship between the plasma filtration rate, the hydrostatic pressure, and the colloid osmotic pressure in the capillaries.

Right underneath the dermis lies the subcutaneous space, also known as the subcutis or hypodermis. The subcutis is several times thicker than the dermis and lies above the muscle fascia or bone if the muscle is not present. It mainly consists of adipose tissues (subcutaneous fat) and has much higher water permeability than that of the dermis. Therefore, it acts like a water-absorbing layer when edema occurs and is the main target for edema detection.

*MICROSCOPIC STRUCTURES OF THE SKIN – EXTRACELLULAR MATRIX, INTERSTITIAL FLUID, AND INTRACELLULAR COMPONENT*

When zooming into the microscopic structure of the interstitial space, it further divides into two parts: the extracellular matrix (ECM, the non-conductive backbone) and the interstitial fluid (the conductive fluid). Around one-third of the total water in the body is the extracellular fluid, and 80% of the extracellular fluid is the interstitial fluid. The remaining 20% is mostly the plasma in the blood vessels (Figure 2.2).

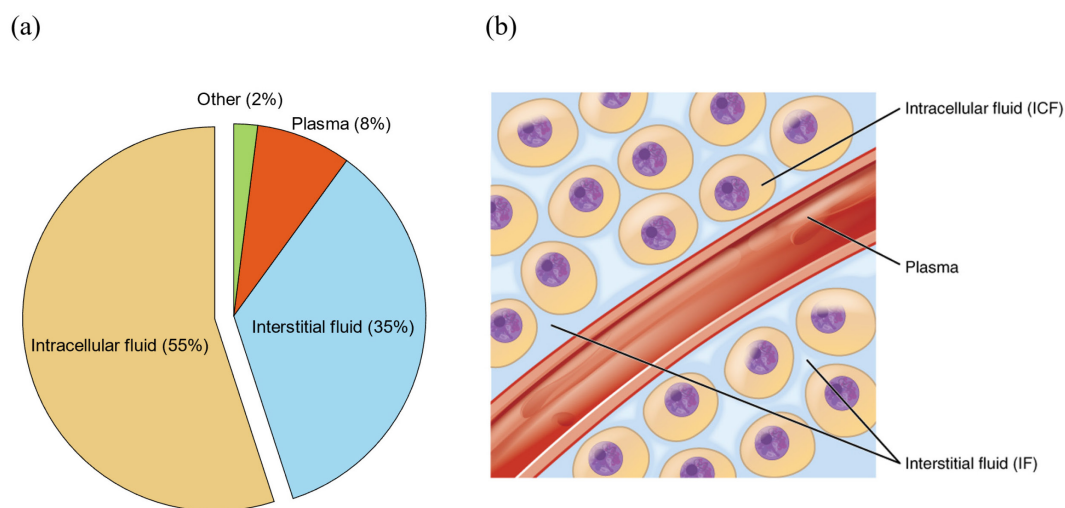


**Figure 2.2:** (a) Body mass distribution shows the average adult's solid and fluid weight percentages. The liquid portion is divided into the intracellular and extracellular components, and the latter contains both the interstitial fluid and blood plasma. (b) The schematic drawing shows the location of the main body fluid components. The figure is reprinted under Creative Commons Attribution-ShareAlike 4.0 International License (Biga et al., 2019).

The extracellular matrix is mainly composed of macromolecules that are water-absorbing. These molecules include collagen, elastin, and glycoproteins. Most of them carry negative charges and attract positive ions. The interstitial fluid consists of several cations and anions, including  $\text{Na}^+$ ,  $\text{Cl}^-$  and  $\text{HCO}_3^-$ . The molar concentrations of these ions are close to those of blood plasma (Figure 2.3). From the total ion

concentration, the average conductivity of interstitial fluid is estimated to be 2.2 S/m at body temperature. The measured value is around 2.0 S/m (Figure 2.3).

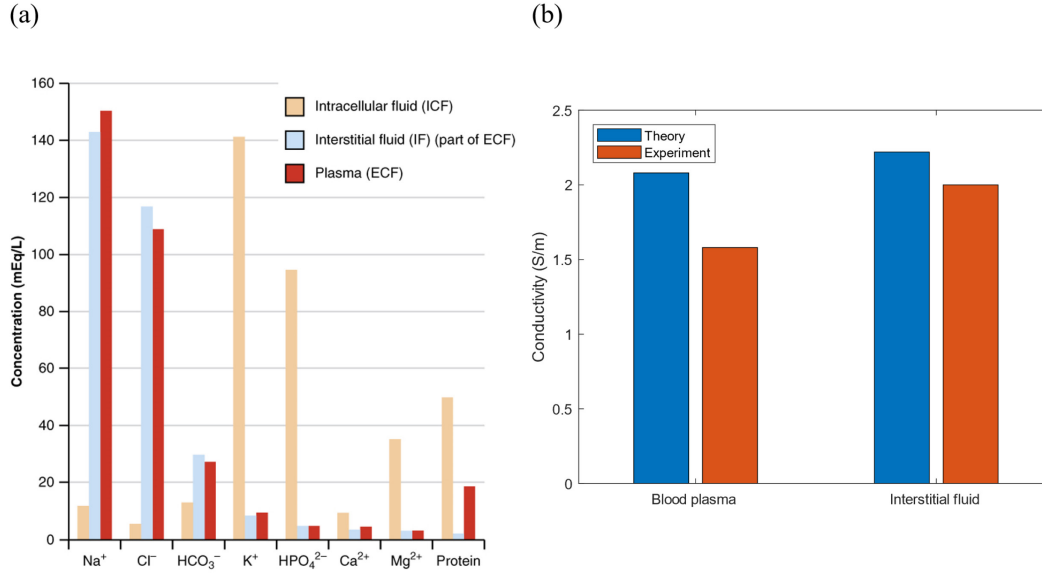


**Figure 2.3:** (a) Body fluid composition showing the concentrations for each ion type. Note the similarities between blood plasma and interstitial fluid. The figure is reprinted under Creative Commons Attribution-ShareAlike 4.0 International License (Biga et al., 2019). (b) The electrical conductivity of blood plasma and interstitial fluid derived from ion concentrations (blue) and experimental measurements (orange) at body temperature (Peters et al., 2005).

### MICROCIRCULATION IN THE SKIN

The circulation of body fluid in the skin follows the revised Starling equation, which is based on the glycocalyx–cleft model (Levick and Michel, 2010):

$$J_v = L_p S [P_c - P_i - \sigma(\Pi_p - \Pi_g)] \quad (2.1)$$

, where  $J_v$  is the filtration rate in volume per unit time,  $L_p$  is the hydraulic conductivity,  $S$  is the capillary surface area,  $P_c$  and  $P_i$  are the hydraulic pressure in the capillary and interstitial space, respectively,  $\sigma$  is the Staverman's reflection coefficient,  $\Pi_p$  and  $\Pi_g$  are the colloidal osmotic pressure of the blood plasma and sub-glycocalyx, respectively.

The steady-state colloidal osmotic pressure in the sub-glycocalyx  $\Pi_g$  is close to zero, so the actual net capillary opposing pressure is higher than the net opposing pressure in the classic Starling model, where the interstitial colloidal osmotic pressure  $\Pi_i$  is used instead of  $\Pi_g$  (Figure 2.4). However, because the net opposing pressure is still lower than the venular pressure in almost every tissue, there is no reabsorption happening in the venules. Under normal conditions, the capillary filtration rate balances out the draining rate of the lymphatic system. The average lymph flow in an adult man is about 150 mL per hour (Caro et al., 2011).

The filtration rate  $J_v$  varies along the length of the microcapillaries. The mean filtration rate per unit area is approximately  $10^{-6} \frac{\mu m}{s \cdot Pa}$  for human capillary beds (Caro et al., 2011).

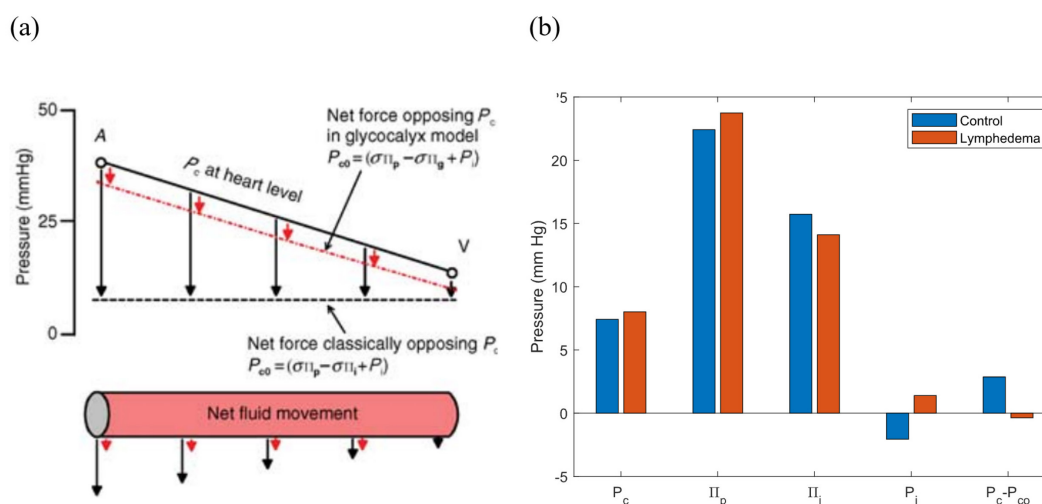


**Figure 2.4:** (a) The revised Starling equation shows the glycocalyx-cleft model (red dashed line and arrows) and the classical filtration-reabsorption model (black dashed line and arrows). Net capillary opposing pressures  $P_{co} = \sigma(\Pi_p - \Pi_i) + P_i$  are shown in dashed lines. Continuous drainage of the interstitial fluid by the lymphatics replaces the role of reabsorption in the glycocalyx-cleft model. The figure is reprinted with permission from the Oxford University Press (Levick and Michel, 2010). (b) Starling's pressures measured in human subcutis from arms with lymphedema (orange) and control arms on the contralateral side (blue). Note that lymphedema arms have lower  $\Pi_i$  and higher  $P_i$  than the control.

## 2.2 SKIN EDEMA PATHOLOGY

### *COMMON DISEASES LEADING TO SKIN EDEMA*

The formation of skin edema is closely related to the perturbation of parameters in the revised Starling equation. The common pathological causes related to skin edema are summarized in Table 2.1. I will highlight the target diseases in **bold** and give brief explanations for their pathological causes.

Pathological causes for edema formation associated with the highlighted diseases are:

- (1) **Lymphedema**: Breast cancer patients often have their lymph nodes removed to prevent possible metastasis of cancer cells. The disrupted lymphatic system has less draining efficiency and therefore causes lymphedema in the affected arm. Lymphedema can be unilateral or bilateral depending on the location of lymph nodes.
- (2) **Congestive heart failure**: The weakened heart contractions cause systemic blood circulation to get congested in the ventricles. The congestion elevates the central venous pressure and causes edema. With left ventricular failure, this manifests as pulmonary edema. Whereas with right ventricular failure, this leads to peripheral edema.
- (3) **Deep vein thrombosis**: Thrombus or blood clot formation in the deep veins blocks the circulation and elevates the local venous pressure in the lower extremities (Figure 2.5). If the thrombus gets carried away to the lungs, a more serious and potentially life-threatening disease called pulmonary embolism can occur.

**Table 2.1:** Classification of skin edema pathology according to different parameters in the Starling equation (Cho and Atwood, 2002).

| Capillary hydrostatic pressure ↑  |  |   | Plasma oncotic pressure ↓   |   | Capillary permeability ↑  |
|---|--|---|---|---|---|
| <u>Regional venous hypertension</u><br>(often unilateral) <ul style="list-style-type: none"> <li>• Inferior vena cava compression</li> <li>• <b>Deep venous thrombosis</b></li> <li>• Chronic venous insufficiency</li> <li>• Compartment syndrome</li> </ul> | <u>Systemic venous hypertension</u> <ul style="list-style-type: none"> <li>• <b>Heart failure</b></li> <li>• Constrictive pericarditis</li> <li>• Restrictive cardiomyopathy</li> <li>• Tricuspid valvular disease</li> <li>• Cirrhosis/liver failure</li> </ul> | <u>Increased plasma volume</u> <ul style="list-style-type: none"> <li>• <b>Heart failure</b></li> <li>• Renal failure (acute, chronic)</li> <li>• Drugs</li> <li>• Pregnancy</li> </ul> | <u>Protein loss</u> <ul style="list-style-type: none"> <li>• Malabsorption</li> <li>• Preeclampsia</li> <li>• Nephrotic syndrome</li> </ul> | <u>Reduced protein synthesis</u> <ul style="list-style-type: none"> <li>• Cirrhosis/liver failure</li> <li>• Malnutrition (e.g., kwashiorkor)</li> <li>• Malabsorption</li> <li>• Beriberi</li> </ul> | (Usually clinically evident) <ul style="list-style-type: none"> <li>• Allergic reactions: histamine release (hives), serum sickness, angioedema</li> <li>• Burns</li> <li>• Inflammation/local infections</li> <li>• Interleukin 2 therapy</li> </ul> |
| Lymphatic obstruction or interstitial oncotic pressure ↑  |  |   | Interstitial hydrostatic pressure ↓   |   | Other   |
| <ul style="list-style-type: none"> <li>• <b>Lymphedema (primary or secondary)</b></li> </ul>  |  |   | Vacuum suction (used to induce artificial edema in healthy subjects)  |   | <ul style="list-style-type: none"> <li>• Idiopathic</li> <li>• Myxedema</li> </ul>  |

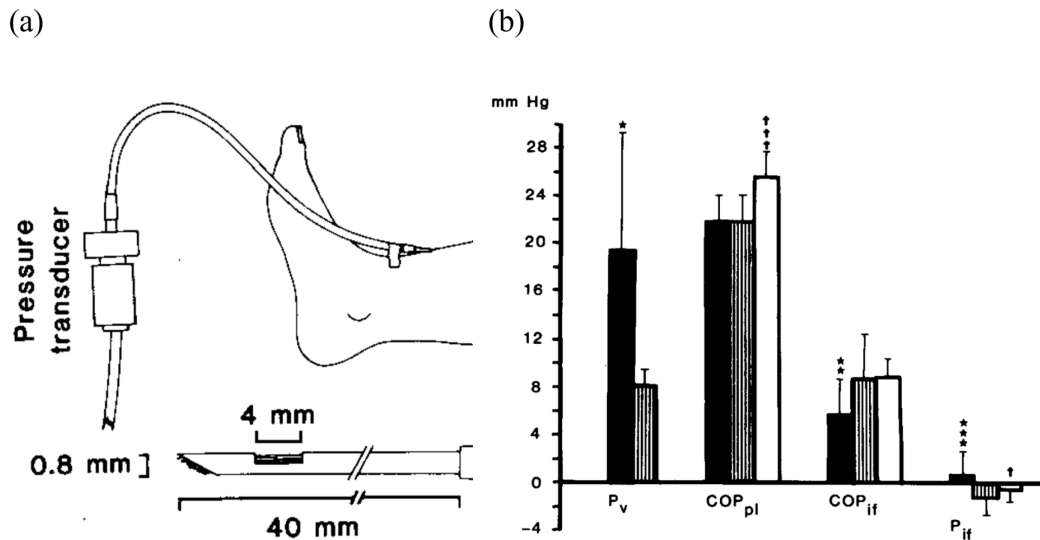


**Figure 2.5:** (a) The schematic drawing of the experimental setup showing the fluid collection needle and the pressure transducer for interstitial pressure measurements in the leg with deep vein thrombosis. (b) The measured pressure components in Starling's equation.  $P_v$  and  $P_{if}$  are the saphenous vein pressure and interstitial pressure,  $COP_{pl}$  and  $COP_{if}$  are the colloid osmotic pressure of the blood plasma and interstitial fluid,  $P_r$  is the reabsorption pressure. Control group: empty boxes. Thrombosed legs: solid boxes. Contralateral legs: grid boxes. Values are presented as mean plus standard deviation. The \* symbol denotes thrombosed legs significantly different from contralateral legs. The † symbol denotes the control group significantly different from contralateral legs. The figures are reprinted with permission from Taylor & Francis (Seem and Strandén, 1986).

Because the tissues constituting the interstitium can easily accommodate several liters of fluid, a patient's weight may increase nearly 10% before pitting edema is evident (Cho and Atwood, 2002). Therefore, it is desirable to detect the onset of edema when there is no sign of swelling visible to the naked eyes.

#### *PATHOLOGICAL CHANGES RELATED TO SKIN EDEMA*

When edema occurs, extra interstitial fluid expands the ECM and causes the collagen bundles to separate from each other. Since aligned collagen bundles generate the strongest ultrasonic speckle reflections, skin edema causes the echogenicity in the

dermis to decrease. On the other hand, adipose lobules in the subcutis are also stretched by ECM expansion and become more reflective to ultrasound waves. The macroscopic changes from skin edema happen mostly in the subcutis layer as its tissue compliance is lower than dermis. When severe edema occurs, the connective tissue (septum) surrounding the adipose lobules is further invaded by the interstitial fluid and represents a dark shadowed zone in the ultrasound image (Figure 2.6).

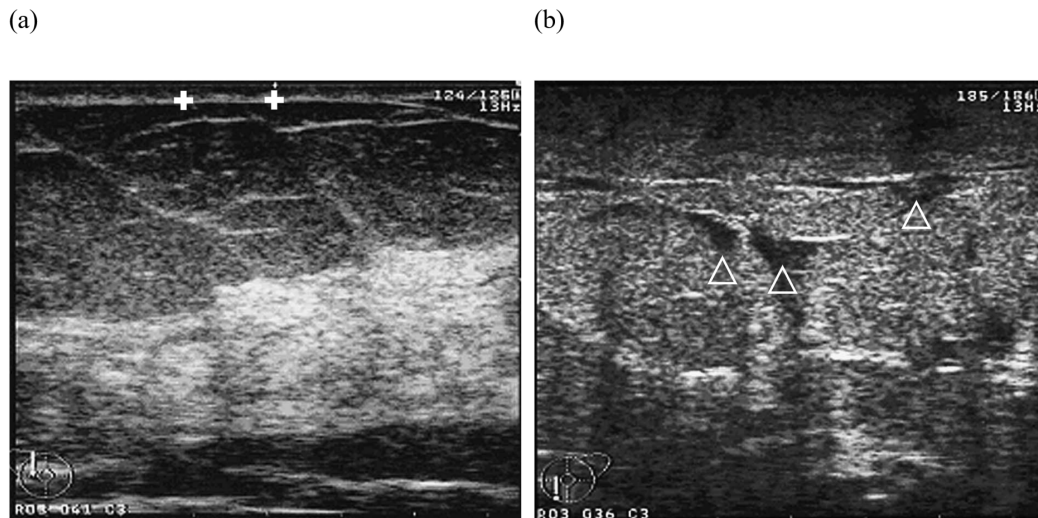


**Figure 2.6:** Skin ultrasonography images from (a) normal skin and (b) skin with severe subcutaneous edema. The interface between dermis and subcutis is visible in normal skin (a), which is indicated by white solid crosses. However, the interface is not visible in the skin with severe subcutaneous edema (b). On the other hand, interstitial fluid invasion is visible in (b) as dark low echogenic regions indicated by white hollow triangles. The figures are reprinted with permission from Taylor & Francis (Rönkä et al., 2004).

Besides changes in the ECM structure, the interstitial fluid volume fraction and electrical conductivity of the subcutis increases significantly. A previous clinical study confirmed the electrical impedance increase in the edematous skin by inserting a pair of needles (12 mm long and 0.4 mm in diameter) in the subcutaneous space (Hladovec and Přerovský, 1973).



In addition to electrical properties, the increase in the bounce-back time in the finger pitting test is related to the viscoelastic properties of the skin. When water enters the subcutis, ECM absorbs the water and causes the skin to become softer and more viscous. These phenomena are related to the decrease in mechanical moduli and increase in the viscous time constant. Therefore, mechanical properties can also be used to quantify edema (section 1.2.1).

On the microscopic scale, skin edema is usually accompanied by inflammatory cell infiltration. As seen from the microscopy images (Figure 2.7), the dermis is intruded by extra interstitial fluid and inflammatory cells and appears to be paler even after the hematoxylin and eosin (H&E) dye is applied. Similar patterns can be found in the subcutis of a lymphedema limb (Nakagawa et al., 2020).

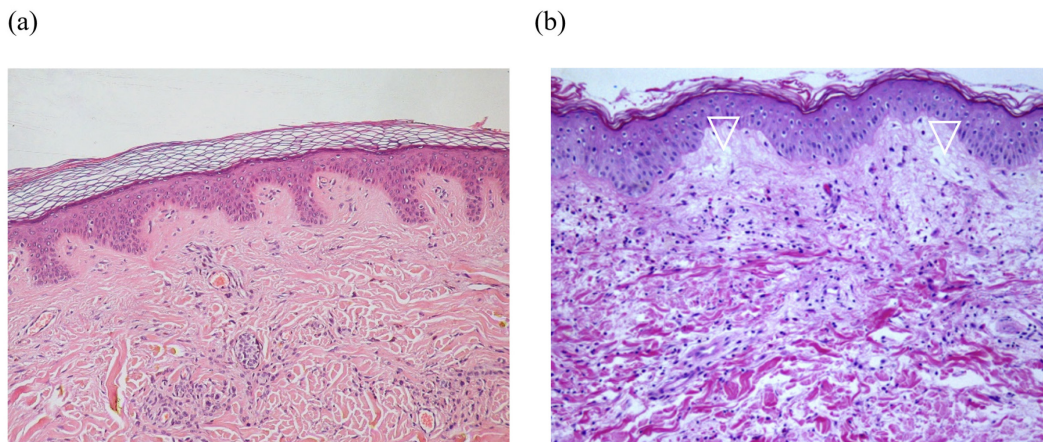


**Figure 2.7:** Histology images from (a) normal skin (magnification ratio 10x) and (b) skin with mild to moderate edema (magnification ratio 100x) stained with H&E. The mild edema has a pale-white appearance in the papillary dermis and is not stained well by H&E. The areas intruded by the interstitial fluid are indicated by white hollow triangles. Figure (a) is reprinted and licensed from Wikipedia (Kilbad, 2008). Figure (b) is reprinted with permission from Elsevier (Berg et al., 2013).

## 2.3 INTERSTITIAL FLUID MODEL

As seen in the previous section, interstitial fluid accumulation is the direct cause for skin edema. Therefore, quantifying skin edema with interstitial fluid is the goal of this section. A quantitative interstitial fluid model is proposed to establish the relation between interstitial fluid volume fraction and skin conductivity. I first introduce the multiple Cole-Cole dispersion for normal skin from the electrical impedance spectroscopy data and then modify it to fit into the interstitial fluid model.

### *SKIN THICKNESS AND INTERSTITIAL FLUID VOLUME FRACTION*

I will propose the electric circuit model for the ECM combined with interstitial fluid based on the following assumptions: (1) the interstitial fluid conductivity is a constant, (2) the subcutis conductivity is a function of the interstitial fluid conductivity and its volume fraction in the subcutis, (3) the overall skin conductivity is a weighted sum of the epidermis, dermis, and subcutis conductivity. The weightings are calculated from the inductive loss distribution function. The electric circuit model is shown below (Figure 2.8):

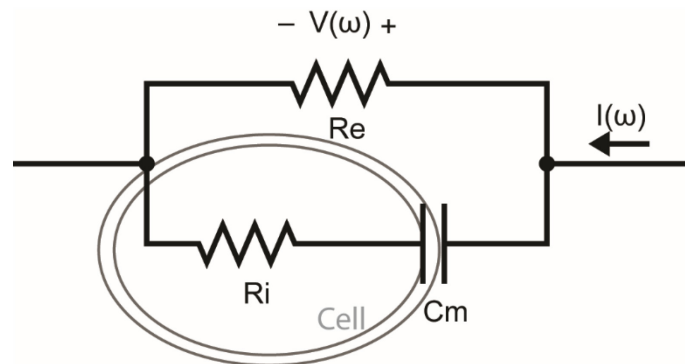


**Figure 2.8:** Electric circuit model of biological tissues showing the extracellular branch of resistance  $R_e$  and the intracellular branch with resistance  $R_i$  and membrane capacitance  $C_m$  in series.

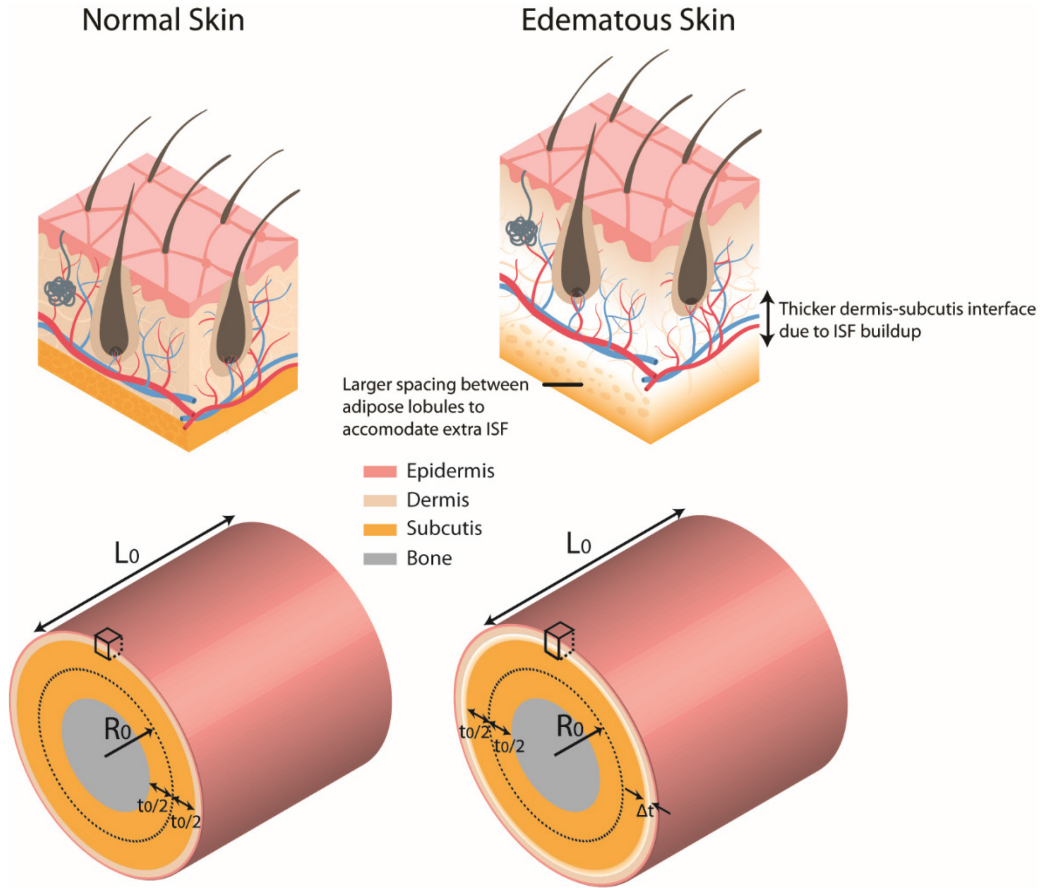


**Figure 2.9:** Skin conductivity model based on the subcutaneous thickness and interstitial fluid volume fraction.

$$\varphi_{sub} = \frac{V_{sub}\varphi_0 + \Delta V_{sub}}{V_{sub} + \Delta V_{sub}} = \frac{2\pi R_0 L_0 t_0 \varphi_0 + 2\pi \left(R_0 + \frac{t_0}{2} + \frac{\Delta t}{2}\right) L_0 \Delta t}{2\pi \left(R_0 + \frac{\Delta t}{2}\right) L_0 (t_0 + \Delta t)} \quad (2.2)$$

$$\xrightarrow{t_0 > 0} \frac{\frac{R_0}{t_0} \varphi_0 + \left(\frac{R_0}{t_0} + \frac{1}{2} + \frac{\Delta t}{2t_0}\right) \frac{\Delta t}{t_0}}{\left(\frac{R_0}{t_0} + \frac{\Delta t}{2t_0}\right) \left(1 + \frac{\Delta t}{t_0}\right)} = \frac{\frac{\varphi_0}{\kappa} + \left(\frac{1}{\kappa} + \frac{1 + \tau}{2}\right) \tau}{\left(\frac{1}{\kappa} + \frac{\tau}{2}\right) (1 + \tau)}$$

, where  $R_0$ ,  $L_0$ ,  $t_0$ , and  $\varphi_0$  are the normal values of subcutis radius, length, thickness, and ISF volume fraction, respectively;  $\Delta t$  and  $\sigma_{ISF}$  are the subcutis thickness increase and conductivity of the interstitial fluid. To further simplify the equation, I

introduced two non-dimensional variables  $\kappa = \frac{t_0}{R_0}$  and  $\tau = \frac{\Delta t}{t_0}$  representing the (principal) surface curvature and normalized subcutis thickness increase.

The conductivity model for a porous material can be extended to a frequency-dependent model. The intracellular conductivity is extracted from the Cole-Cole dispersion model and set to be the same value (that is, no presence of intercellular edema). The extracellular conductivity is calculated from the interstitial fluid volume fraction according to Maxwell's mixture equation (assuming the subcutis consists of homogeneous and isotropic suspension of adipose cells in the ECM). The sum of intracellular and extracellular conductivity is the effective conductivity of the skin.

$$\begin{aligned}\sigma_{eff} &= \sigma_{int} + \sigma_{ext} \\ &= \sigma_{Cole-Cole} + \sigma_{sub}(\varphi_{sub})\end{aligned}\quad (2.3)$$

$$\sigma_{sub} = \sigma_{ISF} \varphi_{sub}^{1.5} \quad (2.4)$$

In the most general multiple Cole-Cole dispersion relation, the electrical model can be expanded to include multiple capacitive branches with different relaxation time constants. In the lower MHz frequency range, only the beta dispersion is dominant, and one single dominant capacitive component is enough to model the electrical properties of the skin.

#### *FREQUENCY DEPENDENCY OF SKIN CONDUCTIVITY*

Skin is a lossy dielectric material that can be modeled by the multiple Cole-Cole dispersion equation:

$$\hat{\epsilon}(\omega) = \epsilon_{\infty} + \sum_n \frac{\Delta\epsilon_n}{1 + (j\omega\tau_n)^{1-\alpha_n}} + \frac{\sigma_0}{j\omega\epsilon_0} \quad (2.5)$$

, where  $\hat{\epsilon}(\omega)$  is the complex dielectric constant,  $\epsilon_{\infty}$  is the dielectric constant as frequency approaches infinity.  $\Delta\epsilon_n$ ,  $\tau_n$ , and  $\alpha_n$  are the dielectric constant difference,

relaxation time, and a parameter controlling the frequency spread of the  $n^{\text{th}}$  dispersion,  $\sigma_0$  is the DC conductivity,  $\omega$  is the angular frequency, and  $\epsilon_0$  is the permittivity in vacuum.

The total equivalent conductivity is:

$$\begin{aligned}
 \sigma &= -\omega\epsilon_0 \text{Im}[\hat{\epsilon}(\omega)] \\
 &= \sigma_0 - \omega\epsilon_0 \sum_n \frac{\Delta\epsilon_n \text{Im}[(-j\omega\tau_n)^{1-\alpha_n}]}{[1 + (j\omega\tau_n)^{1-\alpha_n}][1 + (-j\omega\tau_n)^{1-\alpha_n}]} \\
 &= \sigma_0 + \omega\epsilon_0 \sum_n \frac{\Delta\epsilon_n \sin\left[\frac{(1-\alpha_n)\pi}{2}\right] (\omega\tau_n)^{1-\alpha_n}}{1 + (\omega\tau_n)^{2(1-\alpha_n)} + 2 \cos\left[\frac{(1-\alpha_n)\pi}{2}\right] (\omega\tau_n)^{1-\alpha_n}}
 \end{aligned} \tag{2.6}$$

According to equation 2.6, the conductivity as a function of frequency is plotted and compared to measurements from human skin (Figures 2.10). Note that the skin conductivity is dependent on the hydration status of the epidermis as moisture helps to improve the coupling between the measurement probe and the skin. In addition, the real part (relative permittivity) and imaginary part (loss factor) of the complex dielectric constant exhibit a distinct dispersion at frequencies around 100 kHz for skin, which is consistent with the beta dispersion commonly seen in biological tissues (Figure 2.11). The multiple ( $n = 4$ ) Cole-Cole dispersion model parameters for blood, bone, skin, and fat tissues are summarized in Table 2.1.

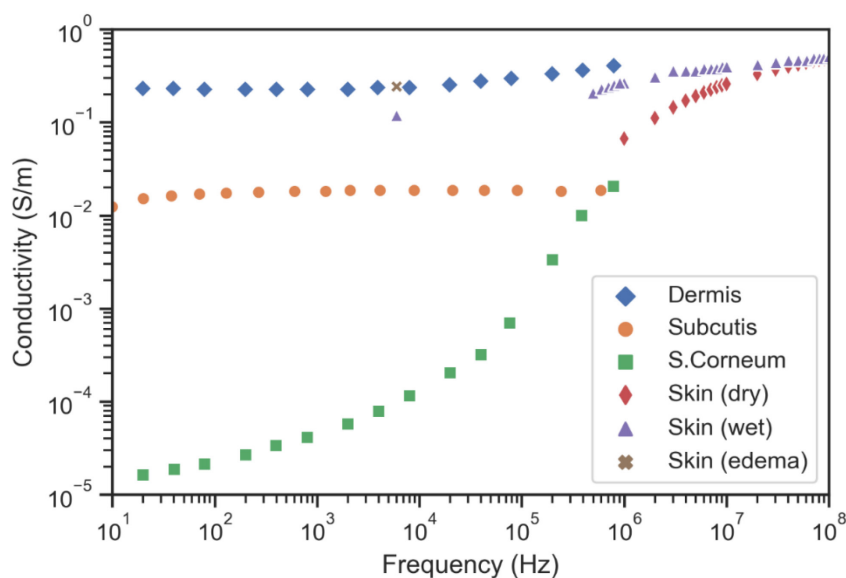


**Figure 2.10:** Conductivity spectrum of different skin layers and the whole skin under different conditions (dry, wet, and edema). The stratum corneum (green solid square) dominates the skin impedance below 100 kHz. The beta dispersion is visible from 100 kHz to 10 MHz. The distinction between dry and wet skin becomes smaller when the frequency is above 10 MHz. The wet skin and skin with edema conductivity data at 6 kHz are measured with two needles inserted into the skin (Hladovec and Přerovský, 1973). The dermis, subcutis, and stratum corneum data below 1 MHz are measured by a non-invasive electrode probe on human female forearms (Birgersson et al., 2010).

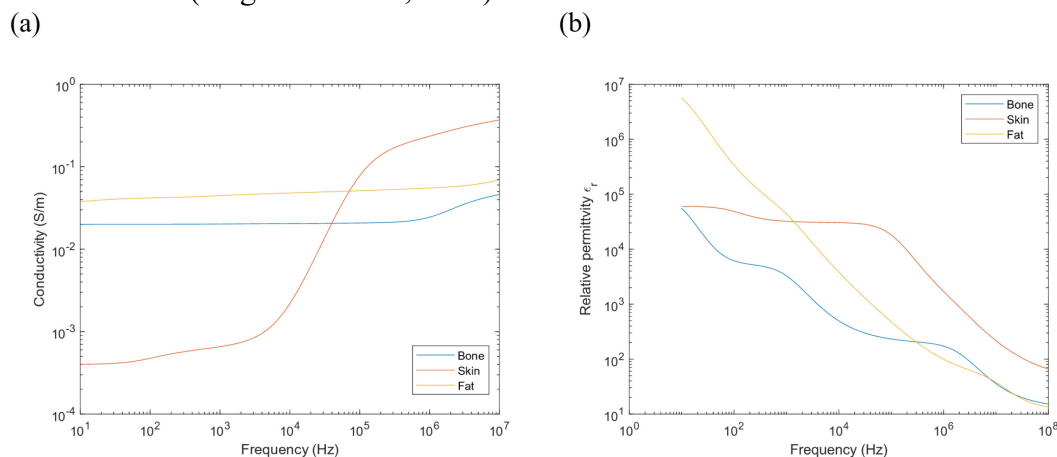


**Figure 2.11:** The typical four-order Cole-Cole model of bone, skin and fat showing the conductivity (a) and relative permittivity (b) versus frequency (Sasaki et al., 2014).

**Table 2.2:** Multiple Cole-Cole dispersion model parameters ( $n = 4$ ) of various tissue types (Sasaki et al., 2014).

| Tissue Type     | $\epsilon_{\infty}$ | $\Delta\epsilon_1$ | $\tau_1$ (ps) | $\alpha_1$ | $\Delta\epsilon_2$ | $\tau_2$ (ns) | $\alpha_2$ | $\Delta\epsilon_3$ | $\tau_3$ ( $\mu$ s) | $\alpha_3$ | $\Delta\epsilon_4$ | $\tau_4$ (ms) | $\alpha_4$ | $\sigma_0$ (mS/m) |
|-----------------|---------------------|--------------------|---------------|------------|--------------------|---------------|------------|--------------------|---------------------|------------|--------------------|---------------|------------|-------------------|
| Blood           | 4.0                 | 56.0               | 8.38          | 0.1        | 5.2k               | 133           | 0.1        | 0                  | -                   | -          | 0                  | -             | -          | 700               |
| Cortical bone   | 2.5                 | 10.0               | 13.3          | 0.2        | 180                | 79.6          | 0.2        | 5k                 | 159                 | 0.2        | 100k               | 15.9          | 0          | 20                |
| Infiltrated fat | 2.5                 | 9.0                | 7.96          | 0.2        | 35                 | 15.9          | 0.1        | 33k                | 159                 | 0.05       | 10M                | 15.9          | 0.01       | 35                |
| Wet skin        | 4.0                 | 39.0               | 7.96          | 0.1        | 280                | 79.6          | 0          | 30k                | 1.59                | 0.16       | 30k                | 1.6           | 0.2        | 0.4               |

## 2.4 REFERENCES

- Berg, I., Nenninger, T., DiMaio, D., Bierman, P., Sandkovsky, U., 2013. Rash and ear swelling in a patient with febrile neutropenia. *International Journal of Infectious Diseases* 17, e360–e361. <https://doi.org/10.1016/j.ijid.2012.12.028>
- Biga, L.M., Dawson, S., Harwell, A., Hopkins, R., Kaufmann, J., LeMaster, M., Matern, P., Morrison-Graham, K., Quick, D., Runyeon, J., 2019. Body Fluids and Fluid Compartments, in: *Anatomy & Physiology*. OpenStax/Oregon State University.
- Birgersson, U., Birgersson, E., Åberg, P., Nicander, I., Ollmar, S., 2010. Non-invasive bioimpedance of intact skin: mathematical modeling and experiments. *Physiol. Meas.* 32, 1–18. <https://doi.org/10.1088/0967-3334/32/1/001>
- Caro, C.G., Pedley, T.J., Schroter, R.C., Seed, W.A., 2011. *The Mechanics of the Circulation*, 2nd ed. Cambridge University Press, Cambridge. <https://doi.org/10.1017/CBO9781139013406>
- Cho, S., Atwood, J.E., 2002. Peripheral edema. *Am J Med* 113, 580–586. [https://doi.org/10.1016/s0002-9343\(02\)01322-0](https://doi.org/10.1016/s0002-9343(02)01322-0)
- Hladovec, J., Přerovský, I., 1973. The Effect of Oedema on the Electric Conductivity of the Subcutaneous Tissue. *Angiologica* 10.
- Kilbad, 2008. Normal Epidermis and Dermis with Intra-dermal Nevus. Wikimedia Commons.
- Komorniczak, M., Madhero88, 2012. Layers of the skin. Wikimedia Commons.
- Kruglikov, I.L., 2015. Influence of layered skin structure on the distribution of radiofrequency currents in dermis and subcutaneous fat. *AIP Advances* 5, 127122. <https://doi.org/10.1063/1.4938545>
- Levick, J.R., Michel, C.C., 2010. Microvascular fluid exchange and the revised Starling principle. *Cardiovascular Research* 87, 198–210. <https://doi.org/10.1093/cvr/cvq062>
- Nakagawa, A., Fujimoto, H., Nagashima, T., Sangai, T., Takada, M., Masuda, T., Teranaka, R., Ota, S., Matsushima, J., Akita, S., Ohtsuka, M., 2020. Histological features of skin and subcutaneous tissue in patients with breast cancer who have received neoadjuvant chemotherapy and their relationship to post-treatment edema. *Breast Cancer* 27, 77–84. <https://doi.org/10.1007/s12282-019-00996-x>
- Peters, M.J., Stinstra, J.G., Leveles, I., 2005. The Electrical Conductivity of Living Tissue: A Parameter in the Bioelectrical Inverse Problem, in: He, B. (Ed.), *Modeling and Imaging of Bioelectrical Activity: Principles and Applications*,



Bioelectric Engineering. Springer US, Boston, MA, pp. 281–319.  
[https://doi.org/10.1007/978-0-387-49963-5\\_9](https://doi.org/10.1007/978-0-387-49963-5_9)

Rönkä, R.H., Pamilo, M.S., von Smitten, K.A.J., Leidenius, M.H.K., 2004. Breast lymphedema after breast conserving treatment. *Acta Oncologica* 43, 551–557.  
<https://doi.org/10.1080/02841860410014867>

Sasaki, K., Wake, K., Watanabe, S., 2014. Development of best fit Cole-Cole parameters for measurement data from biological tissues and organs between 1 MHz and 20 GHz. *Radio Science* 49, 459–472.  
<https://doi.org/10.1002/2013RS005345>

Seem, E., Strandén, E., 1986. Transcapillary forces in subcutaneous tissue of lower limbs with deep venous thrombosis. *Scandinavian Journal of Clinical and Laboratory Investigation* 46, 417–422.  
<https://doi.org/10.3109/00365518609083692>

*Chapter 3*

## SKIN EDEMA SENSOR BASED ON LC-RESONATOR

In Chapter 1, I justified the needs to detect skin edema in the early stage and provide accurate measurements over time. In Chapter 2, I further explained the nature of skin edema and provided evidence on how skin edema changes the structure of the skin and affects the fluid balance at the microscopic level. Based on the assumption that the interstitial fluid volume is conserved, I also presented a skin edema model that converts the interstitial fluid volume fraction to effective skin conductivity. They together provide the necessary background knowledge to address the main problem of noninvasive, continuous, and accurate skin edema quantification.

In this chapter, I will propose a two-step solution to the main problem of continuous and accurate skin edema quantification. The first step establishes the use of skin conductivity as the quantitative index for skin edema. As accumulation of ion-rich interstitial fluid expands the extracellular matrix, the electrical conductivity of skin (the subcutis in particular) is expected to increase significantly. I will review a previous clinical study that confirmed this hypothesis with invasive measurements of subcutis conductivity on edema patients (Hladovec and Přerovský, 1973).

The second step proposes a skin conductivity sensor based on the eddy current method. This method utilizes the change in coil resistance to measure the conductivity of surrounding tissues. Specifically, the eddy-current induced power loss is reflected to the excitation coil as an increase in coil resistance. Previous works showed such a method could measure the target conductivity of simple geometries (Dodd and Deeds, 1968) (Hart et al., 1988). I improve the previous works by proposing a skin conductivity sensor based on the LC-resonator structure that consists of a coil inductor and a parallel capacitor.

### 3.1 PROPOSED METHOD FOR SKIN EDEMA QUANTIFICATION

#### *SKIN EDEMA AND SKIN CONDUCTIVITY*

A previous study on skin conductivity among healthy people and edema patients, to the best of the author's knowledge, provided the first quantitative measurements on the electrical properties of skin edema (Hladovec and Přerovský, 1973). The measurements were taken at the lower leg region in the subjects using a pair of subcutaneous needles, penetrating 12 mm into the subcutis. The results suggest the skin edema has significant correlation with skin conductivity (Figure 3.1). Unfortunately, the study did not have the clinical standard 0-to-4 grading system for comparison. The skin thickness information was also not measured as a separate parameter. Nonetheless, it did show a significant increase of skin conductivity regardless of the disease that causes skin edema (can be of nephrotic, cardiac, lymphatic, or thrombotic origin).

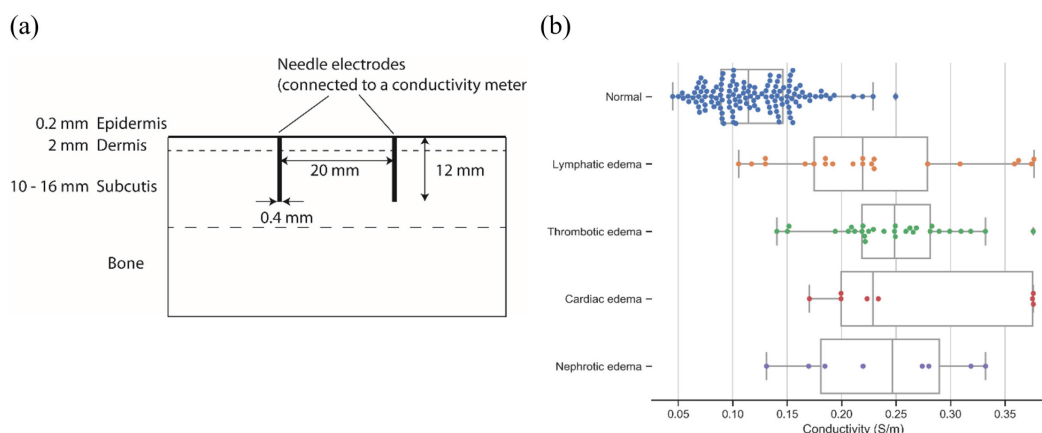


**Figure 3.1:** Invasive skin conductivity measurements on edema patients. (a) The schematic drawing of the experimental setup. (b) skin conductivity values of healthy and edematous skin at 6 kHz (Hladovec and Přerovský, 1973).

Inspired by the study mentioned above, I will focus my study on the eddy current method to quantify skin conductivity. When edema occurs, the interstitial fluid content is expected to increase due to fluid accumulation in the extracellular space.

The equivalent skin conductivity is assumed to follow Maxwell's mixing formula, which is a nonlinear combination of the average skin conductivity and the interstitial fluid conductivity (Chapter 2).

The idea of measuring conductivity originated from the need in the industry. One of the nondestructive testing methods used in the industry to probe metal integrity is the eddy current method. The ASTM E1004 standard test method for determining electrical conductivity using the electromagnetic (eddy current) method summarizes the main aspects of this method, including its limitations that I will discuss and summarize in section 3.2.5 (ASTM International, 2017).

The eddy current method is particularly advantageous for continuous and noninvasive monitoring of skin edema. The advantages include (1) the skin is located at the body surface and is easy to access, (2) the maximum inductive damping occurs at the outmost boundary of the conductive region, which happens to coincide with the skin, (3) other methods like ultrasonography and capacitive sensing can provide the necessary depth and volume information needed to convert the total inductive loss to skin conductivity.

#### *LC-RESONATOR AS EDDY CURRENT SENSOR*

The interaction between the excitation coil and tissue target is best described by a transformer model, where the coil and target are inductively coupled by a mutual inductance  $M$  (Figure 3.2). Applying the circuit transformation that reflects the target impedance to the sensor side, the result is a reflected impedance  $Z_t$  in series with the coil inductance  $L$  given by (Redpath and Hutchison, 1984):

$$Z_t = \frac{\omega^2 M^2 [R_t + j\omega C_t R_t^2 (1 - \omega^2 L_t C_t) - j\omega L_t]}{R_t^2 (1 - \omega^2 L_t C_t) + \omega^2 L_t^2} \approx \frac{\omega^2 M^2 (R_t + j\omega C_t R_t^2 - j\omega L_t)}{R_t^2} \quad (3.1)$$

The real part of  $Z_t$ ,  $Re(Z_t) = \frac{\omega^2 M^2}{R_t}$ , is equivalent to a series resistance  $\Delta R_s$  proportional to  $\omega^2$  and target conductivity  $\sigma \propto \frac{1}{R_t}$ . The imaginary part of  $Z_t$ , on the other hand, is equivalent to a series inductance  $\Delta L = \omega^2 M^2 \left( C_t - \frac{L_t}{R_t^2} \right)$ .

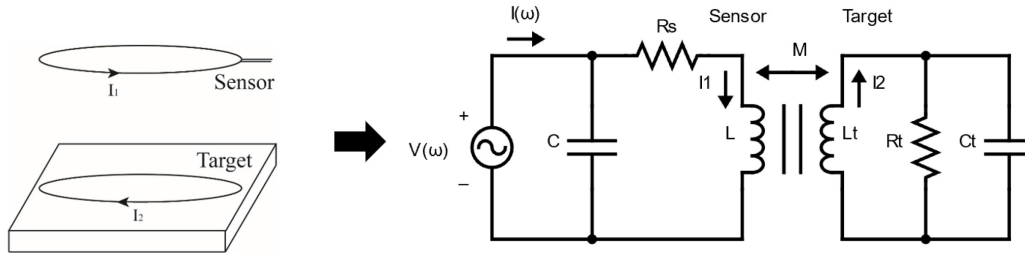


**Figure 3.2:** Eddy current model of the coil sensor showing the sensor-target inductive coupling and the corresponding transformer model (Redpath and Hutchison, 1984).

The transformer model can be expanded to include the dielectric loss from the capacitive coupling effect. The result is an addition of a negligible series resistance to the coil inductance and a parallel capacitance less or equal to the stray capacitance (Redpath and Hutchison, 1984). I will model this parallel capacitance with an extra capacitor  $\Delta C$  (Figure 3.3).

Using an LC-resonator or LC-tank allows easy sensor construction and low power consumption (Nabavi and Nihtianov, 2012), which makes it suitable for battery operated wearable devices. I will discuss two types of sensing with the LC-resonator structure and compare their sensitivity to eddy currents.

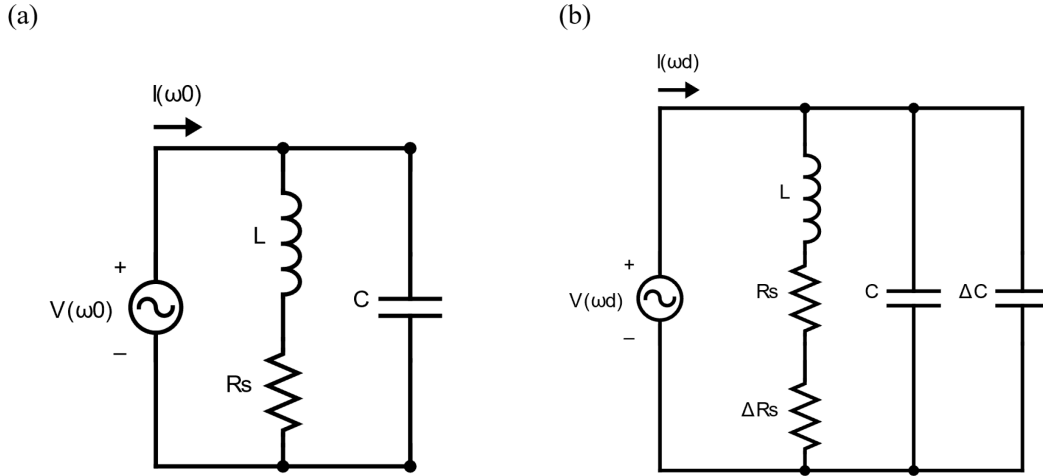


**Figure 3.3:** Simplified equivalent circuit model from the transformer model when the coil sensor is (a) undamped and (b) inductively damped by the target.

Resonant frequency shift sensing:

The resonant frequency shift or detuning in the damped LC-resonator can be calculated as follows assuming  $\Delta L$  from the eddy currents is negligible (Redpath and Hutchison, 1984):

$$\omega_0^2 = \frac{1}{LC} - \left(\frac{R_s}{L}\right)^2 \quad (3.2)$$

$$\omega_d^2 = \frac{1}{L(C + \Delta C)} - \left(\frac{R_s + \Delta R_s}{L}\right)^2 \quad (3.3)$$

$$\omega_0 - \omega_d = \frac{\omega_0^2 - \omega_d^2}{\omega_0 + \omega_d} = \frac{1}{LC} \frac{\Delta C}{C + \Delta C} + \frac{C(2R_s + \Delta R_s)\Delta R_s}{L(\omega_0 + \omega_d)} \quad (3.4)$$

According to the equation, the contribution from capacitive coupling scales with  $\frac{\Delta C}{C + \Delta C} \approx \frac{\Delta C}{C}$ . On the other hand, the contribution from the eddy current damping scales

with  $\frac{C(2R_s + \Delta R_s)\Delta R_s}{L}$ . The typical values for the parameters above are  $\Delta C = 0.1pF$ ,  $C = 1000pF$ ,  $L = 1\mu H$ ,  $\Delta R_s = 1m\Omega$ ,  $R_s = 0.1\Omega$ , therefore  $\frac{\Delta C}{C} = 10^{-4} > 2.01 \cdot 10^{-7} = \frac{C(2R_s + \Delta R_s)\Delta R_s}{L}$  and the detuning is more sensitive to the capacitive coupling than eddy current damping by more than two orders of magnitude.

Power dissipation sensing:

The power dissipation in the damped LC resonator is characterized by the parallel resistance and it is calculated as:

$$R_{p0} = \frac{L}{R_s C} \quad (3.5)$$

$$R_{pd} = \frac{L}{(R_s + \Delta R_s)(C + \Delta C)} \quad (3.6)$$

$$\begin{aligned} R_{p0} - R_{pd} &= \frac{L}{R_s C} \left( \frac{\Delta C}{C + \Delta C} + \frac{\Delta R_s}{R_s + \Delta R_s} \frac{C}{C + \Delta C} \right) \\ &= R_{p0} \left( \frac{\Delta C}{C + \Delta C} + \frac{\Delta R_s}{R_s + \Delta R_s} \frac{C}{C + \Delta C} \right) \end{aligned} \quad (3.7)$$

Using the same values previously assumed, the contribution from capacitive coupling again scales with  $\frac{\Delta C}{C + \Delta C} \approx \frac{\Delta C}{C}$  and the contribution from eddy current damping scales with  $\frac{\Delta R_s}{R_s + \Delta R_s} \frac{C}{C + \Delta C} \approx \frac{\Delta R_s}{R_s + \Delta R_s}$ , therefore  $\frac{\Delta C}{C} = 10^{-4} \ll \frac{1}{101} = \frac{\Delta R_s}{R_s + \Delta R_s}$  and the eddy current damping dominates by two orders of magnitude.

Based on the analysis above, the conclusion is to use power dissipation or the equivalent parallel resistance to measure the inductive damping effect.

### 3.2 SKIN CONDUCTIVITY SENSOR

The skin conductivity sensor is an electrical oscillator consisting of a coil inductor  $L$ , a parallel capacitor  $C$ , and a driving circuit that provides the negative resistance (Figure 3.3). The coil inductor creates a time-varying magnetic field. It induces eddy currents in the skin as introduced in section 3.1. The change in coil resistance is measured by a commercially available inductive sensing application-specific integrated circuit (ASIC), LDC1101 from Texas Instruments. Because the inductive loss due to the eddy currents is small compared to the coil's intrinsic resistance, extra loss in the circuit components and printed circuit board should be minimized whenever possible. On the other hand, procedures to optimize the magnetic field distribution and coil geometry will be given in the next chapter.

Besides the inductive loss, two more factors contribute to the apparent loss reported by the sensor: the temperature effect on the coil wire resistivity and dielectric loss due to the interfacial polarization and relaxation dispersion in the skin. As LDC1101 does not contain a temperature sensor, the temperature effect is compensated by attaching a high-accuracy, low-thermal mass temperature sensor to the coil.

#### *COIL SENSOR*

The coil sensor is made from Litz cables with an appropriate copper strand diameter to minimize extra alternating-current (AC) resistance originated from skin and proximity effects (Figure 3.4). The Litz cable is manufactured by the New England Wire company and has a cable configuration of 675 strands of individually insulated American wire gauge 48 wires.



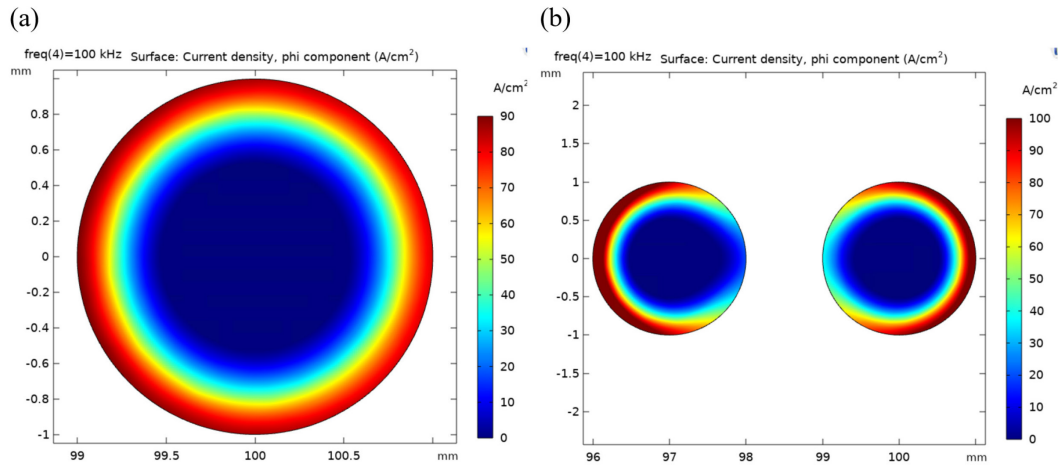


**Figure 3.4:** Simulation results showing (a) the skin effect and (b) the proximity effect in solid copper wires with a diameter of 2 mm. The skin depth of copper is 0.206 mm at 100 kHz. The currents are concentrated near the wire surface with the highest current density (red) and drops to  $1/e$  of the maximum value at one skin depth from the surface (light blue).

The AC resistance of the Litz cable is calculated with the empirical formula provided by the manufacturer as follows (Terman, 1943) (New England Wire Technologies, 2017):

$$\frac{R_{ac}}{R_{dc}} = H + K \left( \frac{n_s r_s}{r_o} \right)^2 G \quad (3.8)$$

, where the  $H$  is the ratio of AC resistance to direct-current (DC) resistance for an isolated solid round wire (Table 3.1),  $G = \left( \frac{r_s \sqrt{f}}{5.22} \right)^4$  is the eddy-current basis factor,  $f$  is the frequency in Hertz,  $n_s$  is the number of strands,  $r_s$  is the strand radius in inches,  $r_o$  is the cable radius in inches,  $K$  is a factor dependent on  $n_s$  (Table 3.2).

**Table 3.1:** Ratio of AC resistance to DC resistance,  $H$ , for an isolated solid round wire.

| $X$ | 0      | 0.5    | 0.6    | 0.7    | 0.8    | 0.9    | 1.0   |
|-----|--------|--------|--------|--------|--------|--------|-------|
| $H$ | 1.0000 | 1.0003 | 1.0007 | 1.0012 | 1.0021 | 1.0034 | 1.005 |

The factor  $X$  is determined by the following formula:

$$X = 0.542r_s\sqrt{f} \quad (3.9)$$

, where  $r_s$  is the strand radius in inches,  $f$  is the frequency in Hertz. For  $r_s = 0.62$  mils and  $f = 9$  MHz,  $X = 1.0$  and  $H = 1.005$ .

**Table 3.2:** Factor  $K$  as a function of the number of strands  $n_s$ .

| $n_s$ | 3    | 9    | 27   | Infinity |
|-------|------|------|------|----------|
| $K$   | 1.55 | 1.84 | 1.92 | 2        |

For  $n_s = 675$ ,  $K = 2$ ,  $r_s = 0.62$  mils,  $r_o = 25$  mils, the ratio of AC to DC resistance is about ten at 9 MHz.

The exact analytical formula for the Litz-cable coil AC resistance is given as (Reatti and Grasso, 2000):

$$\frac{R_{ac}}{R_{dc}} = \frac{\gamma_s}{2} \left[ F_{strand}(\gamma_s) - n_s \left( \frac{4N_l^2 - 1}{3} \right) (2\pi n_s \eta_{ext}^2 + \eta_{int}^2 p) F_{layer}(\gamma_s) \right] \quad (3.10)$$

$$F_{strand}(\gamma_s) = \frac{ber(\gamma_s)bei'(\gamma_s) - bei(\gamma_s)ber'(\gamma_s)}{ber'^2(\gamma_s) + bei'^2(\gamma_s)} \quad (3.11)$$

$$F_{layer}(\gamma_s) = \frac{ber_2(\gamma_s)ber'(\gamma_s) - bei_2(\gamma_s)bei'(\gamma_s)}{ber^2(\gamma_s) + bei^2(\gamma_s)} \quad (3.12)$$

$$R_{dc} = \frac{\rho N l_T}{\pi r_s^2 n_s} \quad (3.13)$$

$$\gamma_s = \frac{\sqrt{2} r_s}{\delta} \quad (3.14)$$

$$\eta_{ext} = \frac{\sqrt{\pi} r_s}{t_o} \quad (3.15)$$

$$\eta_{int} = \frac{\sqrt{\pi} r_s}{t_s} \quad (3.16)$$

$$p = \frac{N r_s^2}{r_o^2} \quad (3.17)$$

, where  $\rho$  is the conductor resistivity,  $l_T$  is the average length per turn,  $\delta = \frac{1}{\sqrt{\pi f \mu \sigma}}$  is the skin depth,  $N$  is the number of turns in the coil,  $N_l$  is the number of winding layers,  $t_o$  is the distance between the centers of two adjacent Litz cables, and  $t_s$  is the distance between the centers of two adjacent strands in the same bundle.

The equations above give an accurate value of  $R_{ac}$  up to the inductor's first self-resonant frequency, according to a recent review paper on various methods to calculate the AC coil resistance (Reatti and Kazimierczuk, 2002). Another precise method to calculate the coil's AC resistance  $R_{ac}$  is the finite element analysis method, and the simulation details will be given in Chapter 5.

### *PRINTED CIRCUIT BOARD LAYOUT*

The printed circuit board layout was carefully drawn to avoid large copper pour regions that minimized eddy currents. Particularly, a gap is introduced in the ground plane to prevent eddy currents to flow in a complete loop. Also, a flexible ferrite sheet

is added between the PCB and the coil as a magnetic shielding that prevents EMI pickup in the loop. Ferromagnetic materials such as ferrite are commonly used in radio frequency identification (RFID) and near-field communication (NFC) technologies as the backing material for coil antennas. In the frequency range of several MHz, the ferrite sheet has a relative permeability of 130, which helps to concentrate the magnetic flux density inside the sheet but reduces the field intensity outside. Therefore, the induced eddy current outside the ferrite sheet is decreased. The temperature coefficient of the relative permeability  $\alpha_{\mu}$  is typically around 200 ppm/K, about ten times smaller than the temperature coefficient of copper resistivity.

### *RESISTANCE AND INDUCTANCE TO DIGITAL CONVERTER*

The LDC1101 ASIC (Texas Instruments) is selected to measure the inductive loss due to eddy currents. The ASIC has two separate modes of operation (Figure 3.5). One is the Rp+L mode, which measures the parallel resistance Rp and resonant frequency together simultaneously. The other mode is the LHR mode, which outputs high-resolution measurements on the resonant frequency.

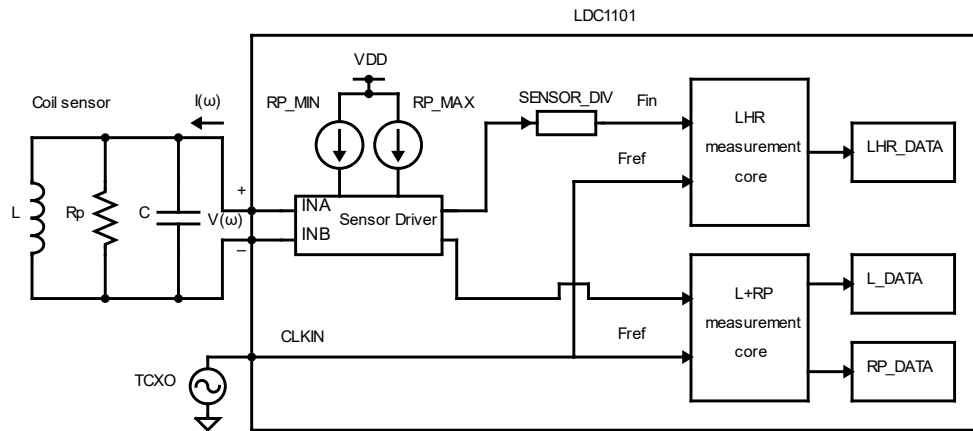


**Figure 3.5:** Block diagram of the LDC1101 ASIC.

Assuming a near-sinusoidal driving current profile (Figure 3.6), the relation between parallel resistance and driving current is:

$$\frac{2I_{drive}R_p}{\pi} = \frac{V_{amp}}{2} \Rightarrow R_p = \frac{\pi V_{amp}}{4I_{drive}} \quad (3.18)$$

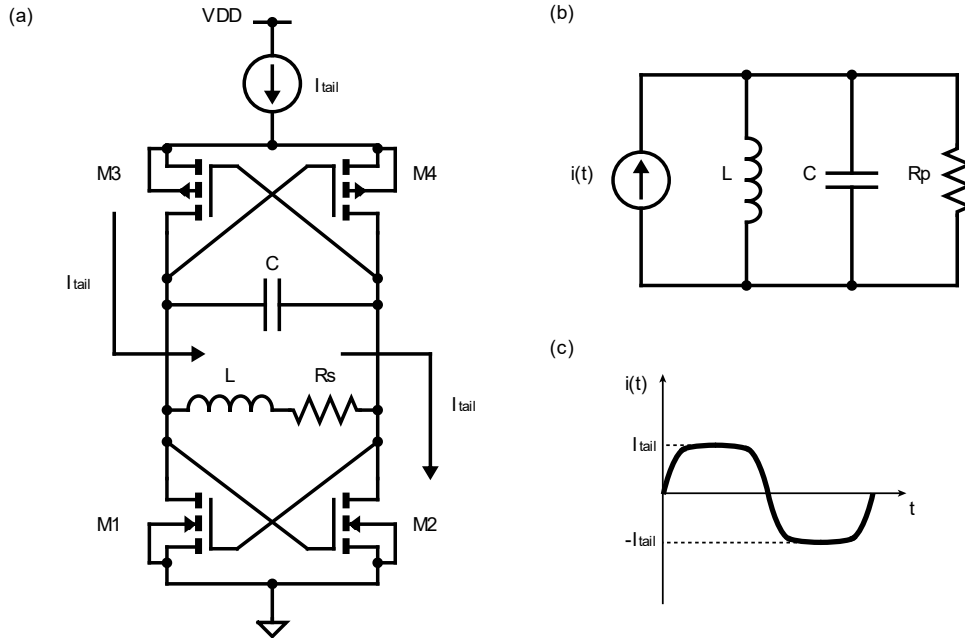


**Figure 3.6:** Circuit diagrams showing (a) the hypothesized current driving circuitry consisting of two cross-coupled pairs, (b) simplified circuit model of the negative resistance cross-coupled differential pair oscillator, and (c) driving current profile of LDC1101 assuming the cross-coupled differential pair is in the current limited regime (Hajimiri and Lee, 1999).

The nominal value of sensor amplitude is  $1.2 V_{pp}$ . The sensor amplitude  $V_{amp}$  must be maintained between  $0.25 V_{pp}$  and  $1.25 V_{pp}$  for accurate resonant frequency measurements:

$$0.25 V_{pp} \leq V_{amp} \leq 1.25 V_{pp} \quad (3.19)$$

Assuming  $V_{amp} = 1.2 V_{pp}$  as recommended by the ASIC datasheet, the relation between  $R_p$  and  $I_{drive}$  becomes:

$$R_p = \frac{0.3\pi}{I_{drive}} \quad (3.20)$$

Given that  $R_p$  typically lies in the range of 3 to 6 k $\Omega$ , this relation gives a value of 150 to 300  $\mu$ A for  $I_{drive}$ . The driving current can be set through the RP\_MAX and RP\_MIN registers, as shown in Figure 3.5.

According to the manufacturer's datasheet (Texas Instruments, 2021), "the LDC1101 uses adjustable current drives to scale the RP measurement range; by setting a tighter current range, a higher accuracy RP measurement can be performed. This functionality can be considered a variable gain amplifier (VGA) front end to an ADC."

A recent work using LDC1101 as a single coil sensor for magnetic induction tomography showed the coil loss measurements are in good agreement with the values predicted by classical electromagnetic theory (Feldkamp and Quirk, 2021). The reported sensor root-mean-square noise is on the order of 0.4 m $\Omega$ , making it a valuable sensor for most medical applications measuring the inductive loss.

#### *TEMPERATURE COMPENSATION CIRCUIT*

The annealed copper making up the wire strands has a temperature-dependent resistivity  $\rho = \rho(T)$ , which means the coil resistance is also a function of temperature that needs compensation.

A linear equation can approximate the relation between the copper resistivity (usually expressed in % of International Annealed Copper Standard, IACS) and temperature. The temperature coefficient of annealed copper conductivity is  $\alpha_{25} = 0.00393/^\circ\text{C}$  at 25  $^\circ\text{C}$ .

$$\frac{\rho(T)}{\rho_{25}} = 1 + \alpha_{25} \cdot (T - 25) \quad (3.21)$$

A typical number of coil resistance change can be calculated as follows:

$$\Delta R_{dc} = \frac{\rho_{Cu} \pi D_{coil} N \alpha_{25} \Delta T}{n_s \pi r_s^2} \quad (3.22)$$

Using  $\rho_{Cu} = 1.72 \mu\Omega/\text{cm}$ ,  $D_{coil} = 2.54 \text{ cm}$ ,  $r_s = 31.6 \mu\text{m}$ ,  $N = 7$ ,  $n_s = 675$ ,  $\alpha_{25} = 0.00393/^\circ\text{C}$ ,  $\Delta T = 18^\circ\text{C}$ , the resulting change in the coil's DC resistance  $\Delta R_{dc}$  is 1.3 m $\Omega$ .

Although this number is only about 4% of the coil resistance, the signal contributed by the eddy current damping is typically in the range of 0.1%. Therefore, it is desirable to have temperature compensation on the coil resistance measurements to avoid errors due to temperature variations. Since the inductance-to-digital ASIC has no built-in temperature compensation circuit, a discrete off-the-shelf temperature sensor is used to measure the temperature of the coil sensor.

The temperature sensor has a self-heating effect of less than 50 m $^\circ\text{C}$  at 25  $^\circ\text{C}$ , assuming 3.3V supply voltage and 500 $\mu\text{W}$  power consumption. It also has a relatively low thermal mass of 0.8 mJ/ $^\circ\text{C}$  when compared to the coil's thermal mass of 2.9 J/ $^\circ\text{C}$ .

The following aspects are discussed in the design guideline from the manufacturer (Texas Instruments, 2013), and I summarize them below:

#### *Coil inductance variation*

“In the absence of magnetic materials, such as ferrous metals and ferrites, the inductance depends only on current flow geometries. Those currents include the current in the coil itself, as well as all eddy currents induced in surrounding conductors.”

“The coil geometry changes with the temperature variation due to thermal expansion or contraction of the coil. For wound copper coils, the coefficient of thermal expansion (CTE):  $\alpha = 17\text{ppm}/^\circ\text{C}$ .  $L$  is typically proportional to the area of the coil divided by the length of the coil. Thus, the overall variation in  $L$  is also  $17\text{ppm}/^\circ\text{C}$ .”

“Another effect to consider is the change in inductance due to change of the current distribution in the windings (proximity effect). Temperature change changes wire resistivity, which in turn causes a change of the conductive skin depth. This effect, however, is much smaller than expansion-contraction of the PCB and is more of academic interest.”

#### *Capacitance variation*

“It is important to note that the value of the capacitance is also subject to temperature variations. To minimize this effect, COG capacitors, which have a  $30\text{ppm}/^\circ\text{C}$  temperature coefficient, are recommended.”

#### *Magnetic core or magnetic shielding*

“For the inductors with magnetic cores, the change in inductance over temperature is dominated in most cases by change of permeability of the core. Exact calculation of such change depends on the core material and the shape of the coil.”

### *SENSOR TESTING*

#### *Temperature coefficient measurement*

A precision thermometer (DP251, Omega) and a digital potentiostat (Gamry G300) were used to measure the coil impedance at DC and 300 kHz. The coil and the potentiostat electrodes connecting to the coil are put in an environmental chamber with a large thermal mass and shielded with metal plates from electromagnetic



interferences. It is also equipped with a digital temperature controller that allows the user to program a temperature versus time profile.

The DC coil resistance is measured with  $\pm 0.3\%$  accuracy in both voltage and current (equivalent to  $\pm 5$  m $\Omega$  accuracy) every 30 seconds with simultaneous temperature reading from a calibrated RTD temperature sensor ( $\pm 0.02$  °C accuracy). The measured temperature coefficient is  $0.0045/^\circ\text{C}$  by linear curve fitting, close to the reference value of  $0.00393/^\circ\text{C}$  for annealed copper at  $25^\circ\text{C}$  (Figure 3.7). Since coil AC resistance is proportional to the DC resistance, the same temperature effect will be at higher frequencies.

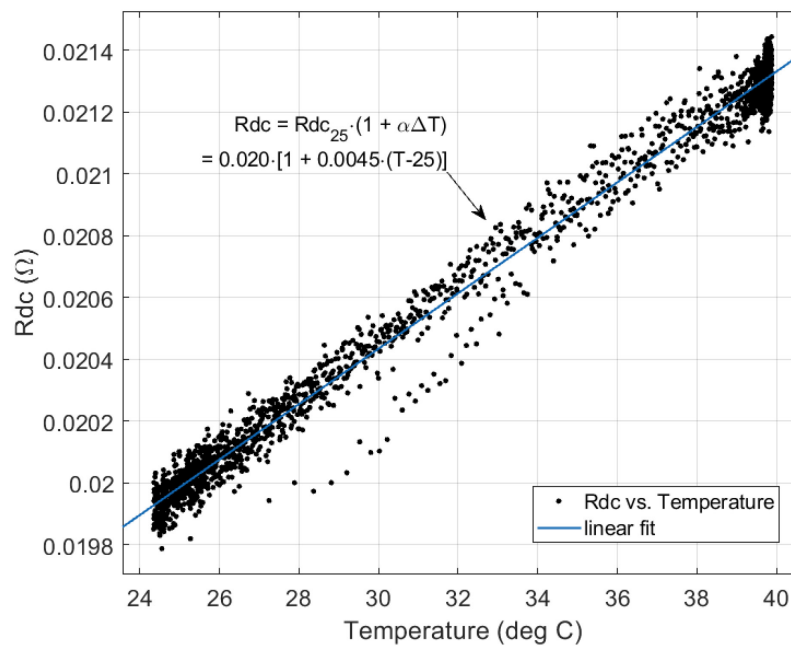


**Figure 3.7:** Custom-made coil's DC resistance  $R_{dc}$  as a function of temperature.

*Capacitance equivalent series resistance (ESR) measurement*

The quality factor  $Q$  is a dimensionless number equal to the capacitor's reactance divided by the equivalent series resistance (equation 3.23). The  $Q$  value changes with frequency as both the reactance and resistance are independent functions of frequency (Figure 3.8).

The parasitic inductance can be modeled as the equivalent series inductance (ESL) in a similar way (Figure 3.9). Still, it is negligible when the frequency is far below the capacitor's self-resonant frequency. Therefore, the manufacturer datasheet typically provides only the  $|Z|$  and ESR values.

$$Q(\omega) = \frac{|X_c|}{ESR(\omega)} = \frac{1}{\omega C \cdot ESR(\omega)} \quad (3.23)$$

The ESR can be derived from the dissipation factor (DF) or loss tangent of the dielectric material as:

$$P_c = V_c^2 \omega C \cdot DF(\omega) = I_c^2 \cdot ESR(\omega) \Rightarrow ESR(\omega) = \frac{DF(\omega)}{\omega C} \quad (3.24)$$

, where  $P_c$ ,  $V_c$  and  $I_c$  are the capacitor's power dissipation, voltage, and current, respectively. Note that dissipation factor  $DF(\omega) = \frac{1}{Q(\omega)}$  is a frequency-dependent material property and must be determined experimentally.

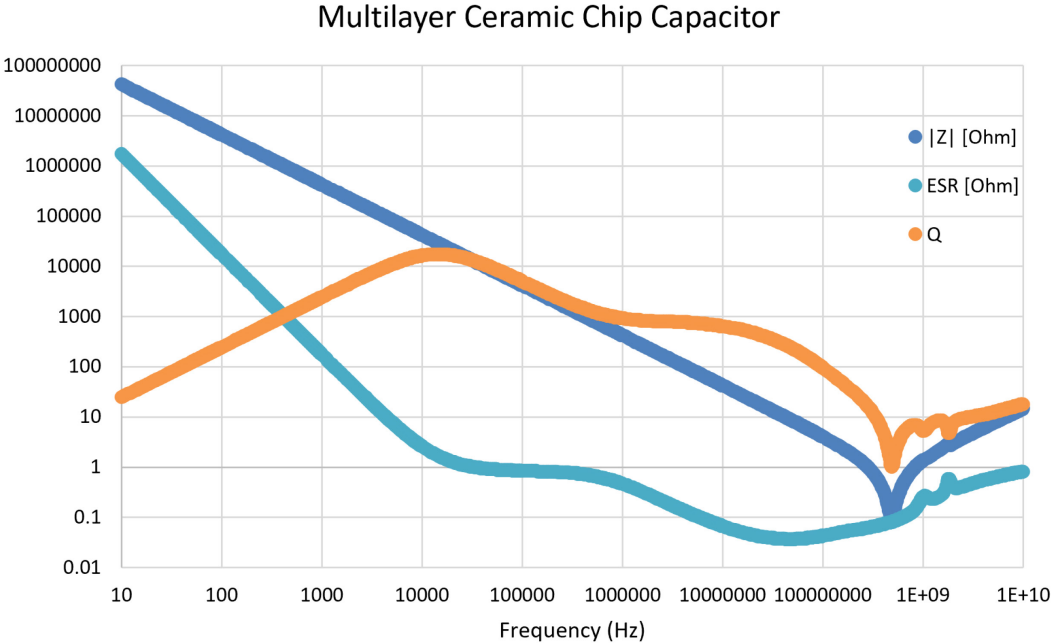


**Figure 3.8:** Typical ESR profile of a surface-mounted multi-layer ceramic capacitor showing frequency ranges dominated by dielectric loss below the self-resonant frequency (~500 MHz) and metallic loss above the self-resonant frequency.

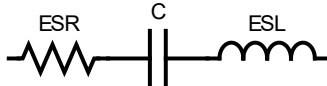


**Figure 3.9:** Equivalent circuit model for a multi-layer ceramic capacitor (MLCC). ESR = equivalent series resistance, ESL = equivalent series inductance.

*Reference clock stability*

The 16 MHz reference clock is generated from a temperature-compensated crystal oscillator (TCXO) with temperature stability of  $\pm 2.5\text{ppm}$  ( $\pm 40\text{ Hz}$ ) in the range of  $-30$  to  $+85^\circ\text{C}$ . The reference clock is measured with a precision frequency counter

for its frequency stability. The mean and standard deviation of the clock frequency are 16.000105 MHz and 2.76 Hz, respectively (Figure 3.10).

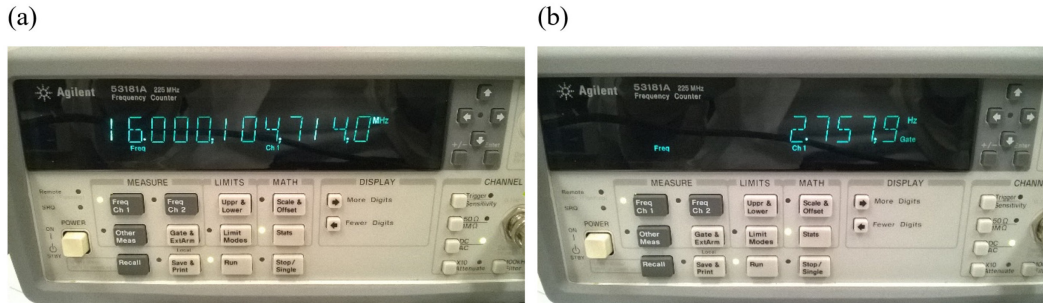


**Figure 3.10:** Frequency counter measurements showing the average reference frequency at 16 MHz (left) and standard deviation (right).

### *Coil quality factor measurement*

The custom-made coil is attached to a standard Q-meter, and the quality factor of the coil alone is measured (Figure 3.11). The quality factor is converted to the coil series resistance at the resonant frequency. The typical Q factor of the coil alone is around 200 in the MHz range, which is much higher than that of the commercially available PCB coils (Figure 3.12). Since the ESR of capacitor is typically much smaller than the coil resistance, and the reactance of the capacitor is on the same order of the reactance of the inductor, the entire LC-resonator has a Q factor close to the coil Q factor.

(a)



(b)

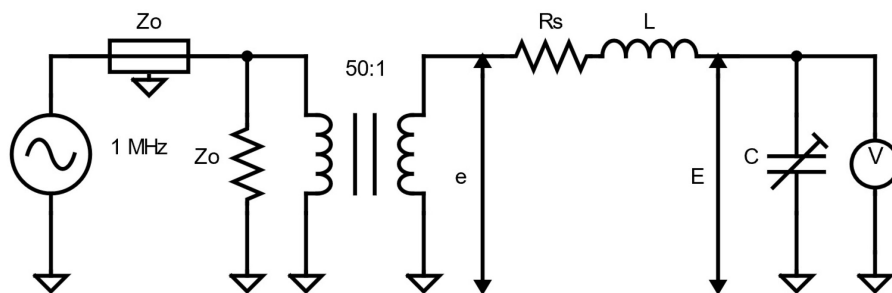


**Figure 3.11:** Coil quality factor measurements. (a) The Q-meter measurement setup. (b) The electrical circuit model of the Q-meter. The quality factor ( $Q$ ) is the ratio of the capacitor voltage amplitude ( $E$ ) to the injection voltage amplitude ( $e$ ) at the resonant frequency.

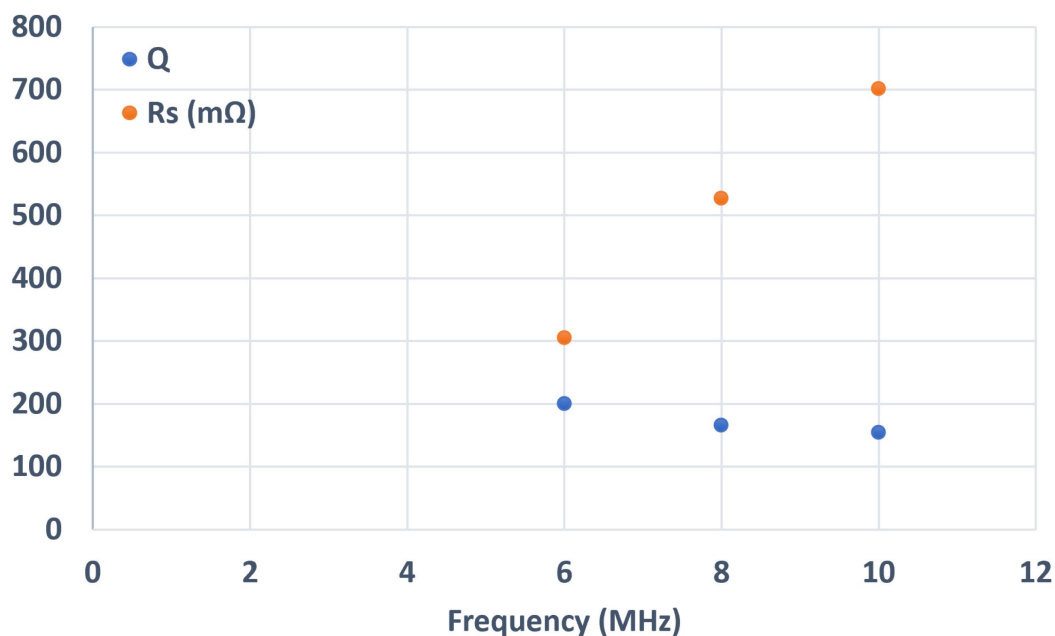


**Figure 3.12:** Measured quality factor  $Q$  and series resistance  $R_s$  of the sensor coil.

### *LIMITATIONS OF THE SENSOR*

However, there are also challenges relating to the long-term stability of the sensor. The main challenges are the drift from the electronic circuit and sensitivity to coil-target relative position and temperature. The ASTM E1004 standard test method provides guidelines on the limitations of the eddy current method (ASTM International, 2017), and I will recap them as follows:

#### *Signal level*

The ASTM standard states, “if the conductivity is not a strong function of the variable of interest, changes in conductivity due to changes in the variable of interest may be too small to detect.” Therefore, it is necessary to first identify the variable of interest. In this work, the variable of interest is the interstitial fluid volume fraction and its relation to subcutis conductivity is predicted by the Maxwell’s mixing formula as described in Chapter 2. However, the layered structure in the skin makes it no longer

a homogeneous material with uniform conductivity. Therefore, further analysis should be done on the equivalent conductivity contribution from each individual skin layer. The details will be given in Chapter 4.

### *Multi-variable dependence*

“The ability to isolate the variable of interest from other variables is also important. For example, if the alloy is not known, the heat treatment cannot be determined from conductivity alone.”

Other variables: temperature ( $R_s$  is  $0.4\%/^{\circ}\text{C}$ , the permeability of magnetic shielding is  $0.2\%/^{\circ}\text{C}$ ,  $C$  is  $30\text{ppm}/^{\circ}\text{C}$ ,  $L$  is  $17\text{ppm}/^{\circ}\text{C}$ ,  $\text{CLKIN}$  is  $2\text{ppm}/^{\circ}\text{C}$ , LDC1101 is  $0.5\%/^{\circ}\text{C}$ ), dielectric loss (ESR in the capacitor [imaginary part of the complex permittivity] and through capacitive coupling into the grounded human body), ferromagnetic loss (imaginary part of the complex permeability), capacitive coupling ( $C_c$  is around  $1\text{pF}$ ), geometric effect (target thickness, lift-off distance, coil diameter, etc. determined by magnetic field distribution).

Temperature effect: “The instrument, probe, reference standards, and parts being examined shall be stabilized at ambient temperature before conductivity evaluation.”

Lift-off effect: “Variations in the separation between the probe coil and the surface of the sample (lift-off) can cause large changes in the instrument output signal. Surface curvature may also affect the coupling.”

Edge effect: “Tests should not be performed within two coil diameters of any discontinuity, such as an edge, hole, or notch.”

Uniformity of the target: “Discontinuities or inhomogeneities in the target near the position of the probe coil will change the value of the measured conductivity.”

Instrument stability: “Instrument drift, noise, and nonlinearities can cause inaccuracies in the measurement.”

Thickness effect: “If the thickness of the sample and the reference standards is at least  $2.6\delta$ , the effect of thickness is negligible.”

Coil diameter effect: “The eddy-current density decrease with depth is also affected by the coil diameter. The change due to coil diameter variation is not considered in the skin effect equation.”



### 3.3 REFERENCES

- ASTM International, 2017. Test Method for Determining Electrical Conductivity Using the Electromagnetic (Eddy-Current) Method. ASTM International. <https://doi.org/10.1520/E1004-17>
- Dodd, C.V., Deeds, W.E., 1968. Analytical Solutions to Eddy-Current Probe-Coil Problems. *Journal of Applied Physics* 39, 2829–2838. <https://doi.org/10.1063/1.1656680>
- Feldkamp, J.R., Quirk, S., 2021. Single-Coil Magnetic Induction Tomography Using the LDC-1101 Chip. *IEEE Sensors Journal* 21, 633–641. <https://doi.org/10.1109/JSEN.2020.3014041>
- Hajimiri, A., Lee, T.H., 1999. Design issues in CMOS differential LC oscillators. *IEEE Journal of Solid-State Circuits* 34, 717–724. <https://doi.org/10.1109/4.760384>
- Hart, L.W., Ko, H.W., Meyer, J.H., Vasholz, D.P., Joseph, R.I., 1988. A noninvasive electromagnetic conductivity sensor for biomedical applications. *IEEE Trans. Biomed. Eng.* 35, 1011–1022. <https://doi.org/10.1109/10.8686>
- Hladovec, J., Přerovský, I., 1973. The Effect of Oedema on the Electric Conductivity of the Subcutaneous Tissue. *Angiologica* 10.
- Nabavi, M.R., Nihtianov, S.N., 2012. Design Strategies for Eddy-Current Displacement Sensor Systems: Review and Recommendations. *IEEE Sensors Journal* 12, 3346–3355. <https://doi.org/10.1109/JSEN.2012.2204321>
- New England Wire Technologies, 2017. Traditional Litz Wire Theory [WWW Document]. URL <https://www.newenglandwire.com/traditional-litz-wire-theory/> (accessed 10.8.21).
- Reatti, A., Grasso, F., 2000. Solid and Litz-wire winding non-linear resistance comparison, in: *Proceedings of the 43rd IEEE Midwest Symposium on Circuits and Systems (Cat.No.CH37144)*. Presented at the Proceedings of the 43rd IEEE Midwest Symposium on Circuits and Systems (Cat.No.CH37144), pp. 466–469 vol.1. <https://doi.org/10.1109/MWSCAS.2000.951684>
- Reatti, A., Kazimierczuk, M.K., 2002. Comparison of various methods for calculating the AC resistance of inductors. *IEEE Transactions on Magnetics* 38, 1512–1518. <https://doi.org/10.1109/20.999124>
- Redpath, T.W., Hutchison, J.M., 1984. Estimating patient dielectric losses in NMR imagers. *Magn Reson Imaging* 2, 295–300. [https://doi.org/10.1016/0730-725x\(84\)90195-4](https://doi.org/10.1016/0730-725x(84)90195-4)
- Terman, F., 1943. *Radio Engineers' Handbook*.

Texas Instruments, 2021. LDC1101 data sheet, product information and support [WWW Document]. URL <https://www.ti.com/product/LDC1101> (accessed 10.18.21).

Texas Instruments, 2013. LDC100x Temperature Compensation.

## THEORETICAL ANALYSIS FOR SENSOR OPTIMIZATION

In this chapter, I will establish the theoretical framework behind the coil sensor design, including critical performance metrics to optimize the coil geometry for maximal inductive loss in the target while minimizing the coil's AC resistance (Chapter 4.1). Besides boosting the signal level, I will analyze the phase and amplitude noise generated by periodic current injection into the oscillator (Chapter 4.2).

### 4.1 COIL OPTIMIZATION

In the following context, I will assume the secondary magnetic field generated by induced eddy currents is negligible when compared to the primary magnetic field. In other words, the coil inductance is assumed to be roughly the same value in the presence of the target. The assumption is verified by both the theoretical analysis and finite element simulations (Chapter 5).

There are two metrics of the coil sensor that require optimization to maximize the signal-to-noise ratio at the sensor output. The first metric is the geometric damping efficiency, defined as the ratio of inductive loss in the target to the total inductive loss in the entire space,  $\eta_G = \frac{P_{target}}{P_{total}}$ . Another way to look at  $\eta_G$  is how efficiently can the coil geometry minimize leakage electromagnetic fields outside the target.

On the other hand, the electrical damping efficiency is defined as the ratio of the maximum available loss to the total electrical power dissipated in the coil (that is, the undamped coil's resistive loss plus the eddy current damping loss). This ratio is a function of coil geometry and a function of operating frequency, as both the skin effect and the proximity effect are highly dependent on frequency. Practically

speaking, unless the coil is made of superconducting materials, the electrical damping efficiency is always less than 100% because of the non-zero undamped coil resistance.

The second metric is the electrical damping efficiency  $\eta_E$ , defined as the ratio of the total inductive loss to the total coil power loss,  $\eta_E = \frac{P_{total}}{P_{coil}}$ . Note that  $P_{coil}$  includes the ohmic losses from the coil's AC resistance  $R_{ac}$ , radiation resistance  $R_a$ , and capacitive coupling loss resistance  $R_c$ .

In the following sections, I will go through methods to derive  $\eta_G$  and  $\eta_E$ . The total damping efficiency, defined by  $\eta = \eta_E \eta_G$ , is the figure of merit representing the ratio of inductive loss in the target to the coil power loss. The total damping efficiency is also proportional to the sensor output from the LDC1101 ASIC.

The general optimization procedure for the geometric and electrical damping efficiency is as follows: first I search through all possibly available coil geometries and find the candidate geometries that have a geometric damping efficiency higher than the threshold (typically 80%), then these candidates are further optimized for their electrical damping efficiency by analyzing the detailed skin effect and proximity effect as functions of frequency. Finally, the candidate geometry with the maximal overall damping efficiency (that is, the product of the geometric and electrical damping efficiency) is selected along with the associated optimized operating frequency.

### *COIL GEOMETRY AND GEOMETRIC DAMPING EFFICIENCY*

The coil geometry is an important parameter that needs to be optimized. As the eddy current damping (formally quantified by the volumetric electromagnetic loss density) is proportional to the square of induced current density, and the induced current density is proportional to the time derivative of the total magnetic flux enclosed by the target, it is desirable to have the coil geometry just enough to encompass the target (to minimize coil resistance and inductance) and maximize the magnetic flux density

throughout this enclosed region. The geometric damping efficiency is defined as the ratio of the loss in the target to the maximum available loss when the target is the entire space. Note that this ratio is a function of the coil and target geometries only, assuming the secondary field generated by the eddy currents is negligible to the primary field (this assumption holds when the target conductivity is small and can be verified by  $\Delta L_{coil} \ll L_{coil}$ ). Therefore, when the target geometry is given, the optimized coil geometry can be found.

I will analyze several standard coil configurations suitable for wearable sensor designs, including circular and figure-8 coils on flat surfaces and solenoid coils that extend in the out-of-plane direction.

Some simple coil configurations have an analytical formula for their coil resistance increase  $\Delta R_s$  that can be evaluated using numerical integration methods. They are summarized below:

#### *Concentric planar coil*

The formula for the coil resistance increase in a planar coil with concentric loops is (Feldkamp and Quirk, 2017):

$$\Delta R_s = Re\{\Delta Z\} = \mu^2 f^2 \sum_{1 \leq j, k \leq n} \sqrt{\rho_j \rho_k} \int \frac{\sigma(\mathbf{r})}{\rho} Q_{\frac{1}{2}}(\gamma_j) Q_{\frac{1}{2}}(\gamma_k) d\mathbf{r} \quad (4.1)$$

$$Q_{\frac{1}{2}}(\gamma) = \frac{1}{\sqrt{2}} \int_0^{\pi} \frac{\cos(t)}{\sqrt{\gamma - \cos(t)}} dt \quad (4.2)$$

$$\gamma_j = \frac{\rho^2 + \rho_j^2 + z^2}{2\rho_j\rho}, \gamma_k = \frac{\rho^2 + \rho_k^2 + z^2}{2\rho_k\rho} \quad (4.3)$$

$$\rho = \sqrt{x^2 + y^2} \quad (4.4)$$

, where  $\mu$  is the magnetic permeability of the material (assumed to be uniform across the entire space),  $f$  is the frequency,  $\sigma(\mathbf{r})$  is the conductivity of the material,  $Q_{\frac{1}{2}}(\gamma)$  is the toroidal function defined for  $1 < \gamma < \infty$ ,  $n$  is the number of turns,  $\rho_j$  and  $\rho_k$  are the radial distance from the coil axis to loops  $j$  and  $k$ , respectively.

### Circular coil with rectangular cross-section

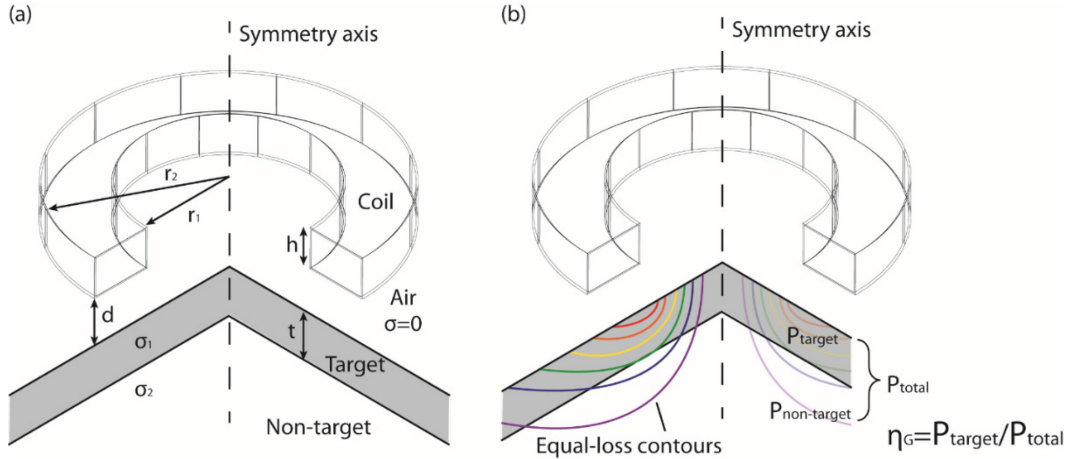


**Figure 4.1:** (a) Circular coil geometry showing the rectangular cross-section and geometric parameters (b) Conceptual drawing of the geometric damping efficiency.

Assuming the skin can be modeled as a flat, two-layer structure, then the coil's AC resistance is related to the tissue conductivity implicitly by  $\Delta R_s = \text{Re}\{Z\}$ , where the coil impedance  $Z$  is given by (Dodd and Deeds, 1968):

$$Z = \frac{j\omega\pi\mu n^2}{h^2(r_2 - r_1)^2} \int_0^\infty \frac{1}{\alpha^5} G^2(r_1, r_2) \left[ 2h + \frac{F(\alpha)}{\alpha} \right] d\alpha \quad (4.5)$$

$$F(\alpha) = 2H(\alpha) + e^{-2\alpha d} H(\alpha)^2 \frac{(\alpha + \alpha_1)(\alpha_1 - \alpha_2) + (\alpha - \alpha_1)(\alpha_2 + \alpha_1)e^{2\alpha_1 t}}{(\alpha - \alpha_1)(\alpha_1 - \alpha_2) + (\alpha + \alpha_1)(\alpha_2 + \alpha_1)e^{2\alpha_1 t}} \quad (4.6)$$

$$H(\alpha) = e^{-\alpha h} - 1 \quad (4.7)$$

$$\alpha_i = \sqrt{\alpha^2 + j\omega\mu\sigma_i} \quad (4.8)$$

$$G(r_1, r_2) = \int_{\alpha r_1}^{\alpha r_2} x J_1(x) dx \quad (4.9)$$

, where  $\mu$  is the magnetic permeability of the material (assumed to be uniform across the entire space),  $d$  is the separation distance between coil's bottom surface and target's top surface (see Figure 4.1),  $h$  is the height of the coil,  $r_1$  and  $r_2$  are the inner and outer radius of the coil,  $\sigma_i$  is the conductivity in layer  $i$ ,  $n$  is the number of turns,  $t$  is the thickness of the first layer.

#### *Planar figure-8 coils*

The magnetic vector potential  $\mathbf{A}(x, y, z) = (A_x, A_y, A_z)$  of a figure-8 coil consisting of two identical circular coils with opposite current flows is:

$$A_x(x, y, z) = [a_1(x, y, z) - a_2(x, y, z)] \cdot y \quad (4.10)$$

$$A_y(x, y, z) = a_1(x, y, z) \cdot (x + r_0) - a_2(x, y, z) \cdot (x - r_0) \quad (4.11)$$

$$A_z(x, y, z) = 0 \quad (4.12)$$

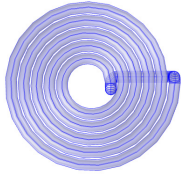
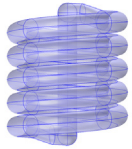
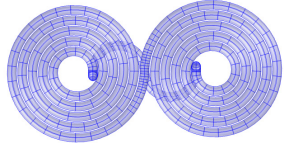
$$a_1(x, y, z) = \begin{cases} 0 & \text{if } (x + r_0)^2 + y^2 = 0 \\ \frac{A_0(\sqrt{(x + r_0)^2 + y^2}, z)}{\sqrt{(x + r_0)^2 + y^2}} & \text{otherwise} \end{cases} \quad (4.13)$$

$$a_2(x, y, z) = \begin{cases} 0 & \text{if } (x - r_0)^2 + y^2 = 0 \\ \frac{A_0(\sqrt{(x - r_0)^2 + y^2}, z)}{\sqrt{(x - r_0)^2 + y^2}} & \text{otherwise} \end{cases} \quad (4.14)$$

, where the circular coils are centered at  $(x, y, z) = (r_0, 0, 0)$  and  $(-r_0, 0, 0)$ , and  $A_0(r, z)$  is the magnetic vector potential of a single circular coil. From the magnetic vector potential, the coil impedance  $Z$  is derived in a way similar to the single circular coil (Dodd and Deeds, 1968).

Benchmark example: I will demonstrate the process to calculate the geometric damping efficiency  $\eta_G = \eta_G(V_{coil}, V_{target})$  when  $V_{coil}$  consists of a circular coil with rectangular cross-sections (tuning parameters  $r_1, r_2, h$ ) and  $V_{target}$  consists of an infinite slab of two layers (Figure 4.1). The results are summarized in Table 4.1.

**Table 4.1:** Common coil geometries and comparison of their geometric damping efficiency  $\eta_G$ .

| Coil types                                  | Planar circular coil   | Solenoid coil  | Planar figure-8 coil   |
|---|--|--|--|
|   |  |  |  |
| Optimized geometry for cylindrical target * | Diameter = 10 cm, number of turns = 6  | Diameter = 15 cm, number of turns = 2  | Diameter = 10 cm, number of turns = 5 for each circular coil                         |
| Geometric damping efficiency $\eta_G$       | ~32.5 %  | ~32.2 %  | ~33.9 %  |

\* Cylinder radius = 5 cm, length = 10 cm, dermis thickness = 2 mm, subcutis thickness = 4 mm



### COIL RESISTANCE AND ELECTRICAL DAMPING EFFICIENCY

The electrical damping efficiency  $\eta_E$  is defined as the ratio of total inductive loss  $P_{total}$  to the coil power loss  $P_{loss}$ . As mentioned at the beginning of this chapter, the latter includes the self-heating loss from the coil's AC resistance  $R_{ac}$  when no conductive target is present (including skin and proximity effects), inductive loss and capacitive coupling loss from the target, and radiation loss from radiation resistance  $R_a$  (negligible in the MHz range).

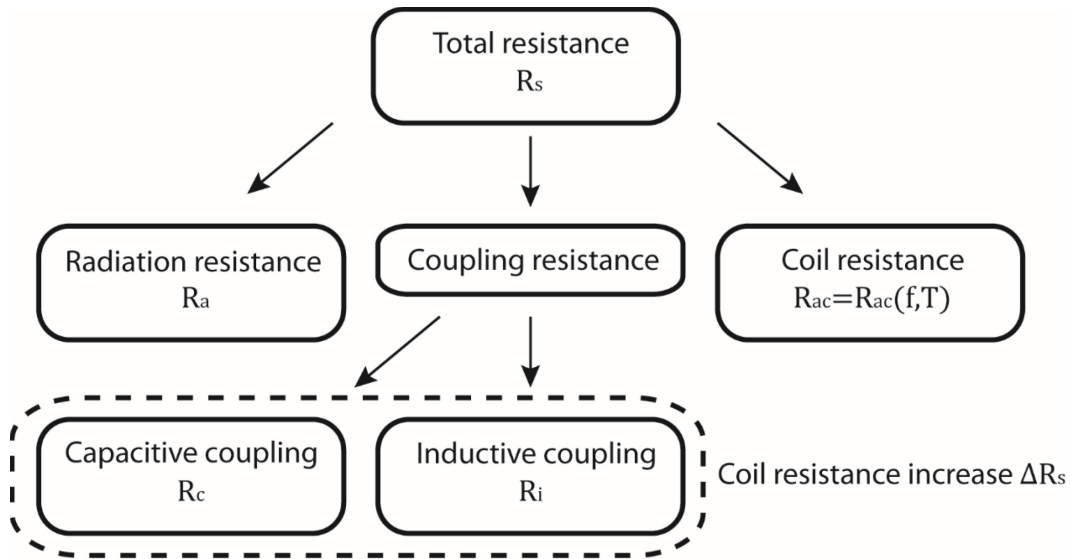


**Figure 4.2:** Components of the total resistance  $R_s$ .

The radiation resistance  $R_a$  of a magnetic loop antenna is given by (Balanis, 2005):

$$R_a(\Omega) = 320\pi^4 \left( \frac{NA}{\lambda^2} \right)^2 \quad (4.15)$$

, where  $N$  is the number of turns,  $\lambda$  is the wavelength, and  $A$  is the loop area.

Substituting in  $1/\lambda = f/c$  where  $f$  is the frequency and  $c$  is the speed of light, the equation becomes:

$$R_a(\Omega) = 320 \left( \frac{\pi f}{c} \right)^4 (NA)^2 = 20\pi^6 N^2 \left( \frac{fD}{c} \right)^4 \quad (4.16)$$

, where  $D$  is the diameter of the coil.

For  $N = 10$ ,  $D = 5$  cm,  $f = 10$  MHz, the radiation resistance is  $20\pi^6 N^2 \left( \frac{fD}{c} \right)^4 = 14.9$   $\mu\Omega$ . This value is about 100 times smaller than the typical coil resistance increase from inductive loss (several m $\Omega$ ). Therefore, the radiation loss is negligible in the MHz frequency range.

A thorough comparison between different methods to calculate coil's AC resistance suggested the Reatti and Kazimierczuk method is the most accurate analytical formula in the literature (Reatti and Kazimierczuk, 2002). According to the study, this formula can predict the AC resistance accurately from DC up to the self-resonant frequency, and the calculation is independent from the winding composition.

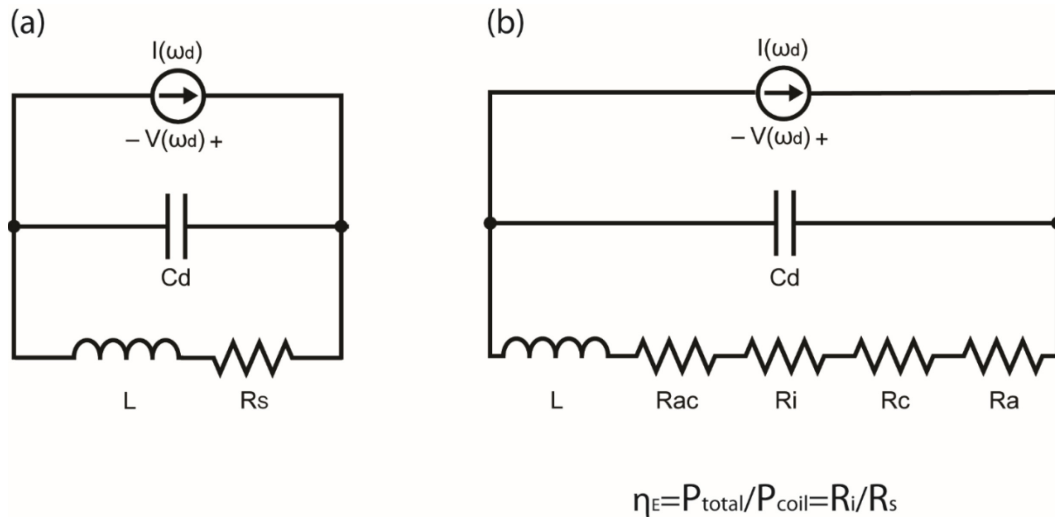


**Figure 4.3:** (a) Equivalent circuit of the LC oscillator at the damped resonant frequency  $\omega_d$ , and (b) the same equivalent circuit with total resistance  $R_s$  expanded to show the individual resistive components. The electrical damping efficiency, defined as the ratio of total inductive loss to the coil loss, is equal to the ratio  $R_i/R_s$  as all the resistive components are in series. See Figure 4.2 for definitions for each resistive element.

As described in Chapter 3, the Reatti and Kazimierczuk method has the following formula for the AC resistance of a solenoid coil made from the Litz cable (equations 3.10 – 3.17).

The Matlab code to calculate the AC resistance is attached below:

```

gamma=ds/(skin_depth*sqrt(2));
A=(ber(0,gamma)*Dbei(0,gamma)-
bei(0,gamma)*Dber(0,gamma))/(Dber(0,gamma)^2+Dbei(0,gamma)^2);
C=(ber(2,gamma)*Dber(0,gamma)+bei(2,gamma)*Dbei(0,gamma))/(ber(0,gamma)^2+bei(0,gamma)^2);

function value = ber(n,x)
value=real(besselj(n,x*exp((3*1i*pi/4))));
end

function value = bei(n,x)
value=imag(besselj(n,x*exp((3*1i*pi/4))));
end

% Calculate ber'(x) with order of n
function value = Dber(n,x)
syms z;
syms nu;
eq=diff(besselj(nu,z*exp(3*1i*pi/4)),z);
value=real(subs(eq,{nu,z},{n,x}));
end

% Calculate bei'(x) with order of n
function value = Dbei(n,x)
syms z;
syms nu;
eq=diff(besselj(nu,z*exp(3*1i*pi/4)),z);
value=imag(subs(eq,{nu,z},{n,x}));
end

```

A final remark on the electrical damping efficiency is that the dissipation power can be combined with losses from other electrical components. For example, the dielectric loss from the parallel capacitor as a function of frequency can be easily

included in the equation as an equivalent series resistor (ESR). This remark is beneficial because the power meter measures the dissipation power in the LC-resonator.

#### *COIL FOCAL SPREAD AREA AND HALF-LOSS PENETRATION DEPTH*

A previous study analyzed 50 coil configurations for their focal spread  $S_{E/2}$  and half-field penetration depth  $d_{E/2}$  (Deng et al., 2013). The half-field penetration depth is defined as the maximal depth from the target surface where the induced electric field decays to half its maximum value. In other words,  $d_{E/2} = \max\{z: |\mathbf{E}(x, y, z)| = \frac{1}{2}E_{max}\}$ . The half-field focal spread area  $S_{E/2}$  is defined as the half-field volume  $V_{E/2}$  (the volume in which  $|\mathbf{E}| \geq \frac{1}{2}E_{max}$ ) divided by the half-field penetration depth  $d_{E/2}$ . The visualization of these quantities is shown in Figure 4.4.

I will characterize the coil focal spread area and half-loss penetration depth in a similar fashion. Using the cumulative inductive loss  $P(x, y, z) = \int_V \sigma |\mathbf{E}|^2 dV$  in place of the induced electric field and noting that  $\sigma |\mathbf{E}|^2$  is non-negative everywhere, it follows immediately that  $P_{max} = \int_{\mathbb{R}^3} \sigma |\mathbf{E}|^2 dV$ , where  $\mathbb{R}^3$  denotes the entire three-dimensional space. Also note that the limit exists because the decay of the electric field is fast enough. The half-loss penetration depth is defined as the minimum depth from the target surface where the cumulative inductive loss equals half of its maximum value. In other words,  $d_{P/2} = \min\{z: P(x, y, z) = \frac{1}{2}P_{max}\}$ . The half-loss focal spread area  $S_{P/2}$  is defined as the minimal area perpendicular to the  $z$ (depth) direction in which the cumulative inductive loss is less than half of its maximum value. In other words,  $S_{P/2} = \min\{\int dx dy : P(x, y, z) = \frac{1}{2}P_{max}\}$  In an axially symmetric coordinate system,  $S_{P/2} = \pi \cdot \min\{x^2 + y^2 : P(x, y, z) = \frac{1}{2}P_{max}\}$ . The threshold is arbitrary for the spread area and depth, so it can be adjusted as needed to fit in a particular application. For example, I will use 80% instead of 50% as the threshold in Chapter 6.

According to the law of conservation of energy, the extra power loss in the coil due to eddy currents is equal to the integrated inductive loss in the target. Therefore, we have  $P_{max} = \frac{|\bar{I}|^2 \Delta R_s}{2}$  and this equation links the cumulative inductive loss function  $P$  to the increase in coil resistance  $\Delta R_s$ . Furthermore,  $\Delta R_s$  can be estimated by looking at the spatial distribution of  $P$  in the target.

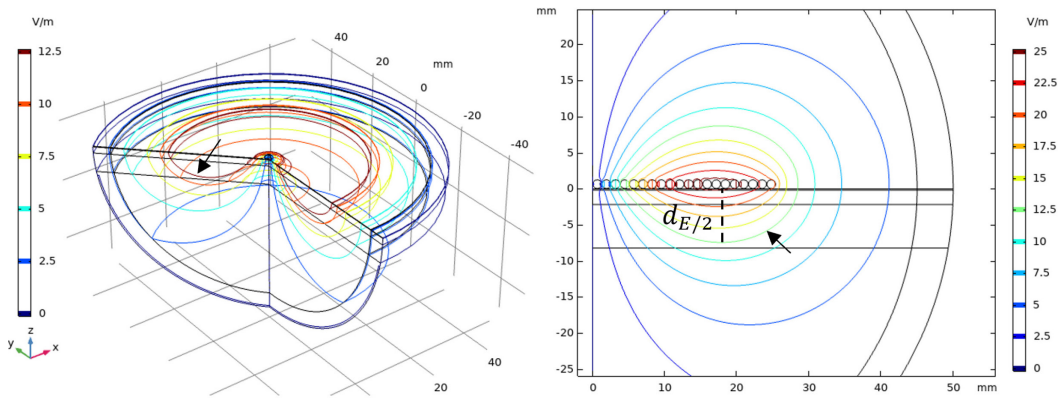


**Figure 4.4:** Contour plots of the induced electrical field intensity  $|\mathbf{E}|$  showing the half-maximum contour of an axially symmetric planar circular coil. The half-field spread  $S_{E/2}$  is approximately the surface area enclosed by the  $E_{max}/2$  contour surface (black arrow in the left figure). The half-field depth  $d_{E/2}$  is the maximum depth of the 2-D contour line representing  $E_{max}/2$  (black arrow in the right figure). Note the colormap in the 3-D contour plot (left) is adjusted for better visualization.

## 4.2 NOISE ANALYSIS

### *THERMAL NOISE*

For an ideal parallel RLC oscillator, the thermal noise comes from the tank resistance and has a root mean square noise voltage of  $v_n^2 \equiv \overline{v_n^2} \Delta f = \frac{4kTR}{4RC} = \frac{kT}{C}$ , where  $\Delta f$  is the bandwidth,  $k$  is Boltzmann's constant,  $T$  is the absolute temperature in Kelvin, and  $C$  is the tank capacitor. Assuming a capacitor value of 390 pF,  $v_n = 3.26 \mu V_{rms}$  and is much smaller than the oscillation voltage ( $V_{amp} = 1.2 V_{pp}$ ). Therefore, the thermal noise is negligible in the parallel RLC oscillator.

### PHASE NOISE AND AMPLITUDE NOISE

The LDC1101 chip modulates the oscillation voltage amplitude  $V_{amp}$  by alternating the coil driving current  $I_{drive}$  between the max and min values defined in the RP\_MAX and RP\_MIN registers. The relation between  $V_{amp}$  and  $I_{drive}$  was given in the previous chapter (equation 3.18).

Every time the current source injects a current pulse into the LC-resonator, a phase change is generated at the output voltage waveform. This process can be characterized by a linear time-varying system with an impulse sensitivity function  $\Gamma(\omega_0 t)$  as (Figure 4.5):

$$h_\phi(t, \tau) = \frac{\Gamma(\omega_0 t)}{q_{max}} u(t - \tau) \quad (4.17)$$

$$\phi(t) = \int_{-\infty}^{\infty} h_\phi(t, \tau) i(\tau) d\tau = \frac{1}{q_{max}} \int_{-\infty}^t \Gamma(\omega_0 \tau) i(\tau) d\tau \quad (4.18)$$

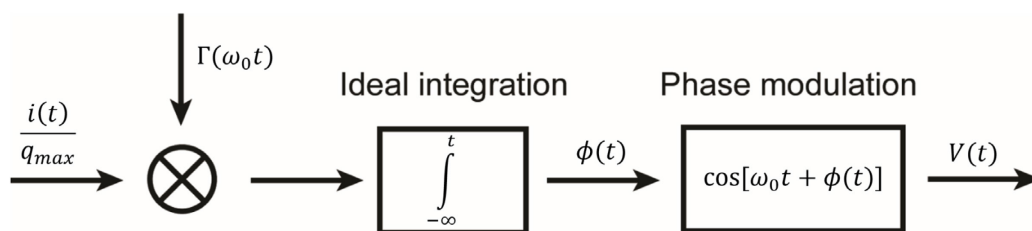


**Figure 4.5:** The linear time-varying system model showing the impulse sensitivity function for the phase modulation process in an oscillator.

The derivation of the phase noise power spectral density follows closely to a previously published work for an RLC oscillator (Yu, 2006), in which the impulse sensitivity function is assumed to be  $\Gamma(\omega_0 t) = \Gamma(\theta) = \cos \theta$ . The resulting power spectral density shows a  $1/(\Delta\omega)^2$  dependency:

$$L_{phase}(\Delta\omega) = \frac{4kTR_p}{V_{osc}^2} \left( \frac{\omega_0}{2Q\Delta\omega} \right)^2 \left( \frac{2\gamma I_{drive} R_p}{\pi V_{osc}} \right) \quad (4.19)$$

, where  $R_p$  is the parallel resistance of the LC tank,  $Q$  is the quality factor,  $\gamma$  is the channel factor of the transistor,  $I_{drive}$  is the driving current, and  $V_{osc}$  is the oscillation voltage.

On the other hand, the amplitude noise is naturally suppressed by the oscillator as it regulates the oscillation voltage at a near-constant level. Therefore, the amplitude impulse response does not behave like a step change  $u(t - \tau)$  as in the phase impulse response. Instead, a decaying function  $d(t - \tau) \rightarrow 0$  as  $t \rightarrow \infty$  is used to describe the amplitude modulation process. The typical assumption for  $d(t - \tau)$  in a first-order system is  $d(t - \tau) = e^{-\omega_0(t-\tau)/Q} \cdot u(t - \tau)$ , where  $\omega_0$  and  $Q$  are the resonant frequency and quality factor of the oscillator, respectively.

Substituting the decaying function  $d(t - \tau)$  for the unit step function  $u(t - \tau)$ , and the amplitude impulse sensitivity function  $\Lambda(\omega_0 t)$  for the (phase) impulse sensitivity function  $\Gamma(\omega_0 t)$ , equations 4.24 and 4.25 become:

$$h_A(t, \tau) = \frac{\Lambda(\omega_0 t)}{q_{max}} d(t - \tau) \quad (4.20)$$

$$A(t) = \int_{-\infty}^{\infty} h_A(t, \tau) i(\tau) d\tau = \frac{1}{q_{max}} \int_{-\infty}^t \Lambda(\omega_0 \tau) i(\tau) e^{-\omega_0(t-\tau)/Q} d\tau \quad (4.21)$$

If the current source  $i(t)$  can be modeled by a white noise source with power spectral density  $i_n^2/\Delta f$ , then the power spectral density of the amplitude noise is

$$L_{amplitude}(\Delta\omega) = \frac{\Lambda_{rms}^2}{q_{max}^2} \cdot \frac{i_n^2/\Delta f}{2 \left( \frac{\omega_0^2}{Q^2} + \Delta\omega^2 \right)} \quad (4.22)$$

The total noise power spectral density is the sum of phase noise and amplitude noise (Figure 4.6), where the noise spectrum is the sum of the phase noise and amplitude noise:

$$L_{total}(\Delta\omega) = L_{phase}(\Delta\omega) + L_{amplitude}(\Delta\omega) \quad (4.23)$$



**Figure 4.6:** The time domain oscillation voltage waveform measured across one of the coil terminals and ground. The amplitude noise resulted from the current injection is indicated by the white double arrow.

The noise spectrum near the resonant frequency was measured using a digital oscilloscope that has the fast Fourier transform function (Figure 4.7). The maximum frequency offset is 50 kHz from the center frequency of 4.8 MHz, and the measured noise is orders of magnitude higher than the values predicted from equations 4.19 and 4.22, possibly due to the extra noise introduced in the oscillator attenuator and analog-to-digital converter. However, there exist numerous methods to reduce the noise. These include small bypass capacitors to ground, additional constant current source, deglitch filter, and RF choke.



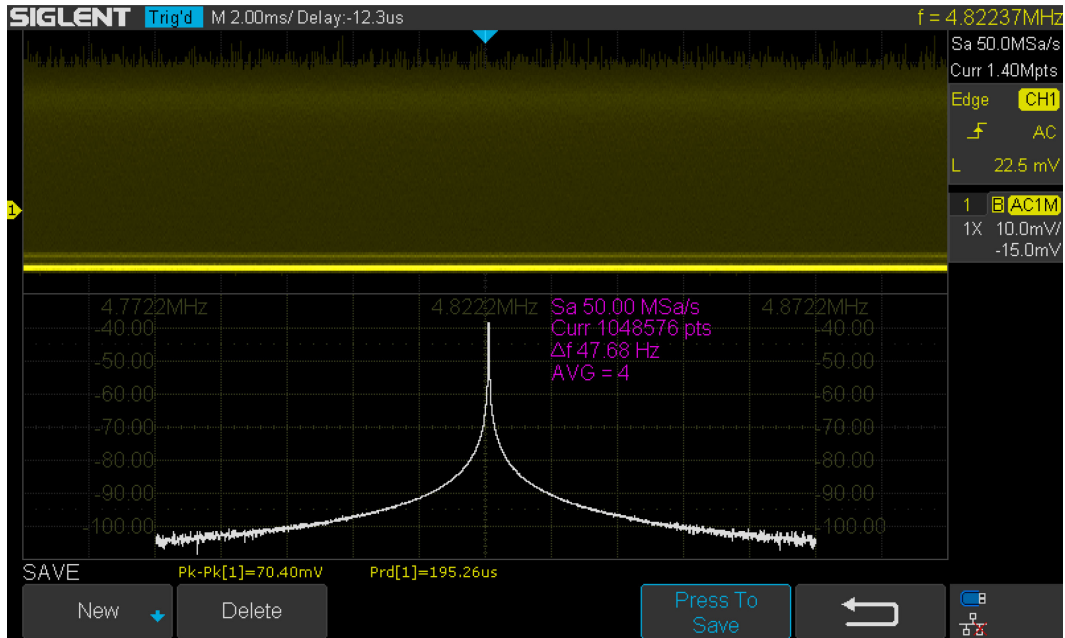


**Figure 4.7:** Representative phase noise spectrum of the oscillation voltage waveform near the sensor resonant frequency at 4.8 MHz. Maximum frequency offset is 50 kHz from the resonant frequency. Horizontal scale is 10 kHz per division. Vertical scale is 10 dBVrms per division.

### 4.3 REFERENCES

- Balanis, C.A., 2005. Antenna Theory: Analysis and Design (3rd. Edition).
- Deng, Z.-D., Lisanby, S.H., Peterchev, A.V., 2013. Electric field depth–focality tradeoff in transcranial magnetic stimulation: simulation comparison of 50 coil designs. *Brain Stimul* 6, 1–13. <https://doi.org/10.1016/j.brs.2012.02.005>
- Dodd, C.V., Deeds, W.E., 1968. Analytical Solutions to Eddy-Current Probe-Coil Problems. *Journal of Applied Physics* 39, 2829–2838. <https://doi.org/10.1063/1.1656680>
- Feldkamp, J.R., Quirk, S., 2017. Coil geometry effects on scanning single-coil magnetic induction tomography. *Phys. Med. Biol.* 62, 7097–7113. <https://doi.org/10.1088/1361-6560/aa807b>
- Reatti, A., Kazimierczuk, M.K., 2002. Comparison of various methods for calculating the AC resistance of inductors. *IEEE Transactions on Magnetics* 38, 1512–1518. <https://doi.org/10.1109/20.999124>
- Yu, S.-A., 2006. Effects of Switching Pairs on CMOS Differential LC Tank Oscillators.

*Chapter 5*

## COIL SENSOR SIMULATION AND EXPERIMENTAL RESULTS

In this chapter, I will approximate the actual coil sensor used in the experiments with a simulation model. The purpose of simulating the sensor is to bridge the gap between predictions from classical electromagnetic theory and measurements from the experiment. The analytical theory described in chapter 4 provides closed-form formulae for both the inductive loss distribution and coil's AC resistance. Using these formulae, the total damping efficiency  $\eta = \eta_E \eta_G$  can be derived as the figure-of-merit for coil optimization. However, in the derivations, the coil geometry is limited to more straightforward cases like solenoid coils or planar coils. The target geometry is also limited to an infinitely large slab or the entire half-space.

These constraints are non-ideal for calculations of real-world inductive damping problems as both the coil and target no longer have simple geometries. Specifically, the target can be a complex anatomical structure (for example, the human ankle shown in Figure 5.7) that requires time-consuming three-dimensional modeling. The coil can also be wound on a curved surface to conform to the target surface. In general, they need numerical methods to approximate the real solution to three-dimensional problems. The finite element analysis (FEA) or finite element method (FEM) is a powerful tool to solve such problems. It decomposes the geometry with a finite number of mesh elements and solves the partial differential equations describing the physical phenomena on these discrete elements. One of the advantages brought by FEM is the ability to resolve details at regions that require higher accuracy. This is especially important for areas in the model with a small but crucial feature (for example, the individual strands in a Litz cable). It is also possible to remove details in regions where no physical phenomenon of interest occurs (for example, a large air domain). The other advantages include multiple sweeping

parameters of interest all at once, which saves a significant amount of time compared to carefully designed experiments.

Using the FEM to solve Maxwell's equations in the frequency domain, I will show results of the AC resistance of a coil made from the Litz cable (chapter 5.1), the primary magnetic field, the induced electrical field, and the volumetric inductive loss function from the coil sensor (chapter 5.2), and finally the human edema model with tissue properties derived from the literature (chapter 5.3).

As two-dimensional problems are easier to solve with lower memory cost and faster numerical convergence, I will first compute the axially symmetric model where the field variables are rotationally invariant around the  $r = 0$  symmetry axis (Figure 5.1).

The model consists of three main parts: the coil sensor, the conductive target, and the surrounding air domain. The target is divided into four layers (epidermis, dermis, subcutis, and bone). Each layer is assigned with the electrical properties from a Cole-Cole dispersion model in the literature.

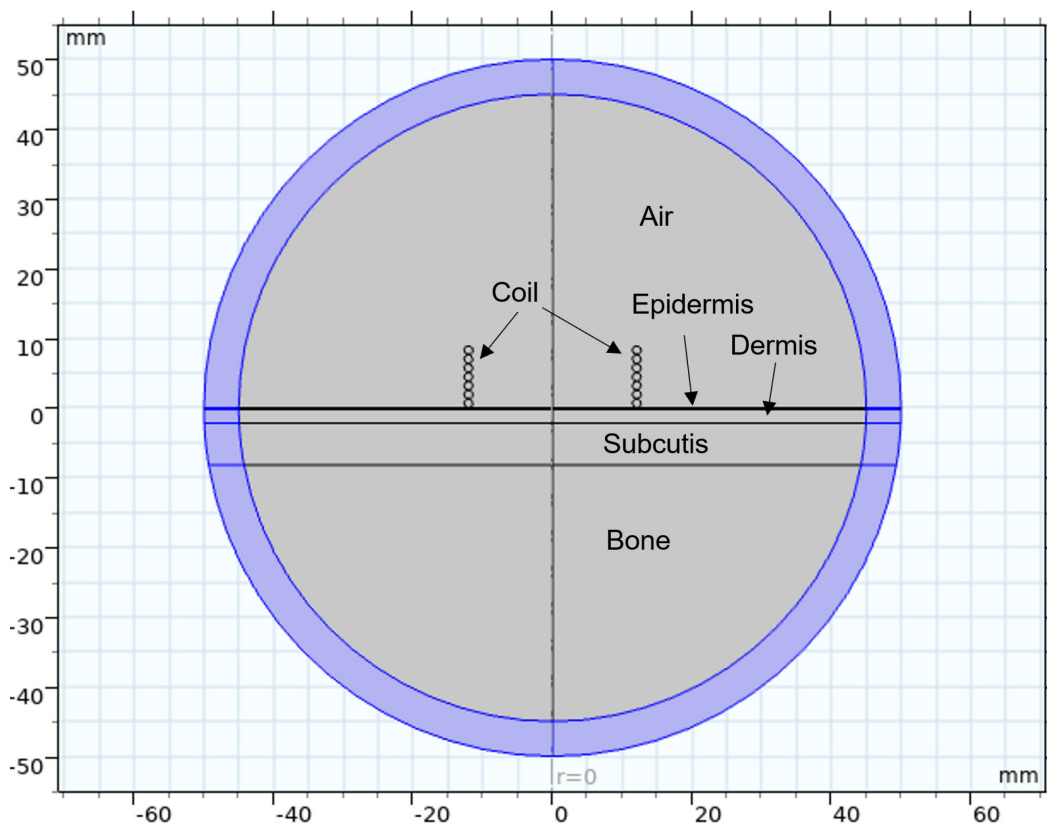


**Figure 5.1:** The schematic drawing of the 2-D axially symmetric model. The symmetric axis is  $r = 0$ . The coil lies flat on the  $z=0$  surface and has its height and width as free variables. The target ( $z < 0$ ) is positioned right below coil and contains four layers (epidermis, dermis, subcutis, and bone). The air domain ( $z > 0$ ) surrounds the coil and target from above and is assigned with zero conductivity. The purple region is the infinite domain that contains a stretched mesh to approximate an infinitely large space. Note the target also stretches out to infinity in this model.

### 5.1 AC RESISTANCE OF COILS MADE FROM THE LITZ CABLE

As mentioned previously in chapter 4, one of the most accurate methods to calculate the coil impedance is the finite element method. This section will describe how to calculate the AC resistance and inductance of a coil made from the Litz cable. A benchmark example of a solenoid coil is given to demonstrate the consistency between theory and simulation. The experimental data measured by both the

LDC1101 ASIC and Q-meter are also shown for comparison with the simulation results.

The coil is made from 7 turns of 1.3 mm Litz cable and has a diameter of 1 inch. The target consists of the epidermis (0.2 mm), dermis (2 mm), subcutis (6 mm), and bone (20 mm). The air domain is a sphere of 5 cm enclosing the coil and target.

The Litz cable used in the simulation consists of individual copper strands in hexagonal packing (Figure 5.2). As described in chapter 3, each individual strand has a radius smaller than the skin depth of copper at the coil's resonant frequency to minimize the skin effect. To capture the skin effect in detail, I chose a mesh element size at least three times smaller than the strand radius. The simulation parameters of a solenoid coil are summarized in Table 5.1.

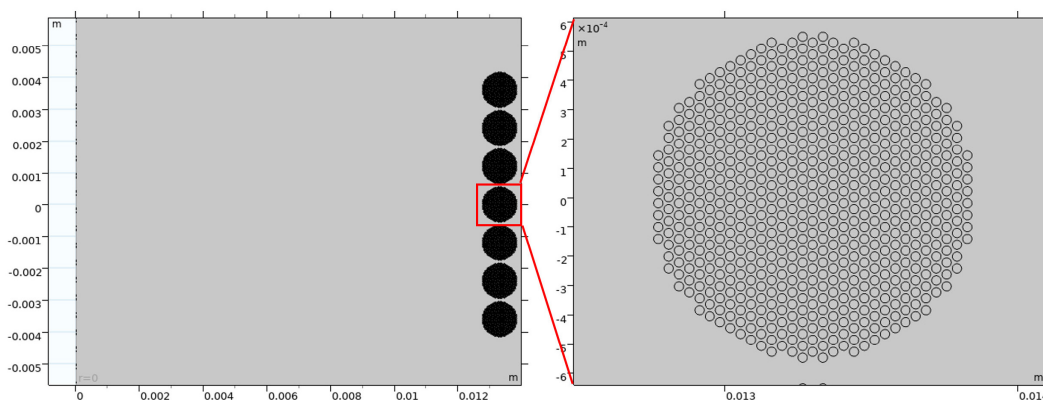


**Figure 5.2:** 7-turn, 1-inch diameter solenoid coil geometry used in the simulation. The magnified view of the Litz cable showing the individual strands is on the right.

**Table 5.1:** Parameters of a solenoid coil made from the Litz cable

| <b>Parameter</b>              |                   |
|-------------------------------|-------------------|
| <b>Number of strands</b>      | 673               |
| <b>Number of turns</b>        | 7                 |
| <b>Strand diameter</b>        | 32 $\mu\text{m}$  |
| <b>Coil diameter</b>          | 1 inch            |
| <b>Copper conductivity</b>    | 58 MS/m           |
| <b>Coil peak current</b>      | 1 A               |
| <b>Coil driving frequency</b> | 0.5 MHz to 10 MHz |

A solenoid or spiral coil may be made from multiple turns of the Litz cable. However, for simplicity and computational efficiency, I will approximate the coil configuration with an axially symmetric model. All the field variables are rotationally invariant with respect to the symmetric axis. The magnetic vector potential is assumed to have only the out-of-plane components as the induced electric field lies primarily in the out-of-plane direction. Displacement currents are ignored as the turn-to-turn parasitic capacitance is small.

The current in each strand is set to be  $\frac{I_{coil}}{n_{strands}}$ . This assumes that the strands swap their relative positions in the Litz cable periodically, so each strand is subject to the same proximity effect and has an equal share of the total current. The current density  $J$ , on the other hand, is a frequency-dependent variable subject to the integral constraint  $\int_{strand} J dA = \frac{I_{coil}}{n_{strands}}$ . At lower frequencies,  $J$  is almost uniform in the radial direction of the strand. When the skin depth approaches the strand radius as frequency increases, the distribution of  $J$  becomes non-uniform and more concentrated near the edge of the Litz cable (Figure 5.3).

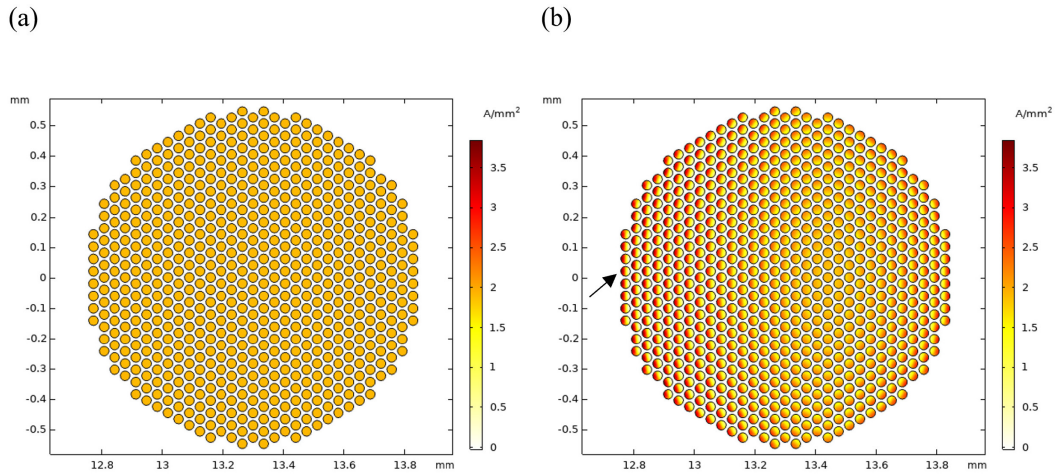


**Figure 5.3:** The current density in the azimuthal direction at (a) 500 kHz where the stand diameter to skin depth ratio  $\frac{d_s}{\delta} \sim \frac{1}{4}$  and (b) 5 MHz where the stand diameter to skin depth ratio  $\frac{d_s}{\delta} \sim 1$ . The proximity effect is visible at 5 MHz near the edge of the Litz cable (indicated by the black arrow).

The coil resistance is calculated from  $R_s = \frac{V}{I_{coil}}$  and the coil inductance is calculated from the spatial integral of magnetic energy per unit volume as  $L = \frac{\int |B|^2}{\mu_0 I_{coil}^2}$ . The results show that the coil resistance is highly dependent on frequency, as it starts from a value close to  $R_{dc}$  at 500 kHz and increases almost seven times of  $R_{dc}$  at 5 MHz (Figure 5.4). However, the coil inductance does not exhibit the same behavior but merely decreases by less than 0.2% over the entire frequency range.



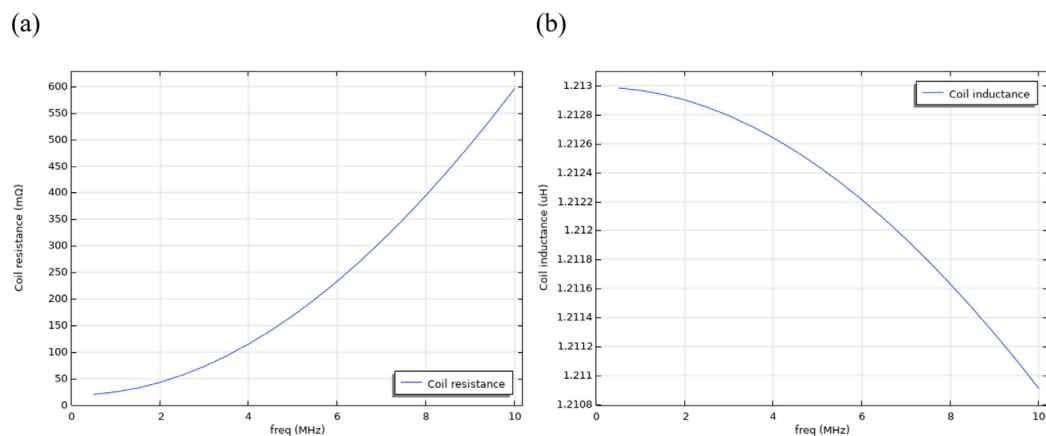


**Figure 5.4:** Simulated coil properties. (a) Coil resistance and (b) coil inductance as a function of frequency.

## 5.2 MAGNETIC FIELD, INDUCED ELECTRICAL FIELD, AND VOLUMETRIC INDUCTIVE LOSS

I approximate the ankle structure by two types of target geometry (Figure 5.5). The first type is the cylindrical target with zero surface curvature, which allows the coil windings to sit directly on the top surface of the cylinder for maximal inductive damping. The second type is the ellipsoidal target with surface curvature given by  $b/a^2$ , where  $a$  and  $b$  are the long semiaxis and the short semiaxis of the ellipse. The different layers under the skin are assumed to be parallel to the surface and their dimensions are listed in Table 5.2.

**Table 5.2:** Parameters of two types of target geometry

| Parameter                  | Cylinder | Ellipsoid   |
|----------------------------|----------|---|
| <b>Epidermis thickness</b> | 0.2 mm   | 0.2 mm  |
| <b>Dermis thickness</b>    | 2 mm     | 2 mm  |
| <b>Subcutis thickness</b>  | 6 mm     | 6 mm  |
| <b>Bone thickness</b>      | 25 mm    | 16.8 mm (parallel to the short axis) to 31.8 mm (parallel to the long axis) |
| <b>Target radius</b>       | 40 mm    | 25 mm (short semiaxis $b$ )<br>40 mm (long semiaxis $a$ )                   |
| <b>Surface curvature</b>   | 0/cm     | 0.15/cm   |
| <b>Target conductivity</b> | 1 S/m    | 1 S/m   |

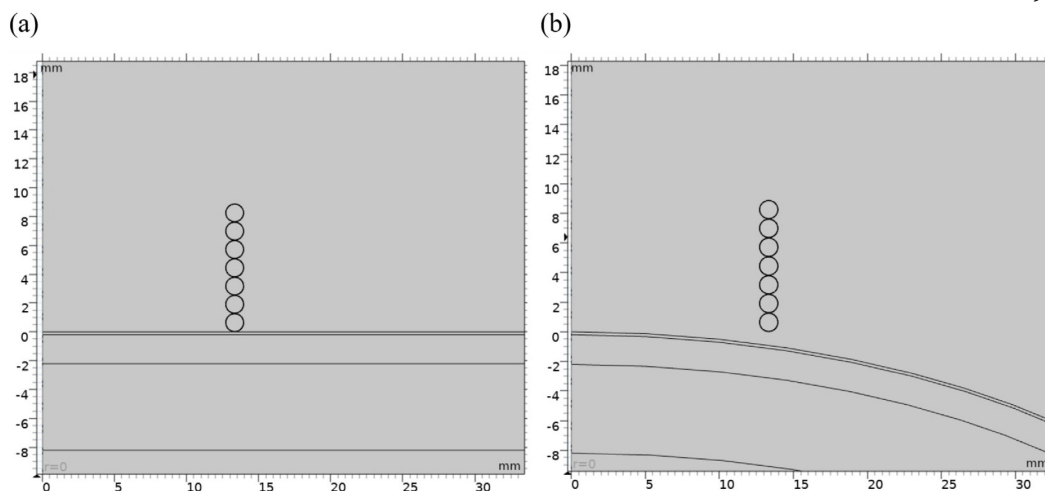


**Figure 5.5:** Two types of target geometry used in the axially symmetric model (left) cylindrical target (right) ellipsoidal target. The coil position remains the same in both cases.

The magnetic flux intensity  $\mathbf{B}$  and the induced electric field  $\mathbf{E}$  are calculated from the magnetic vector potential  $\mathbf{A}$  as  $\mathbf{B} = \nabla \times \mathbf{A}$  and  $\mathbf{E} = -j\omega\mathbf{A}$ . The induced current density  $\mathbf{J}$  and the volumetric inductive loss function  $Q$  are derived from the induced electric field  $\mathbf{E}$  as  $\mathbf{J} = \sigma\mathbf{E}$  and  $Q = \sigma|\mathbf{E}|^2$ . Since  $Q$  is the volumetric inductive loss function and has the physical meaning of inductive loss per unit volume, taking volume integral of  $Q$  over the target volume represents the total inductive loss in the target. The spatial distribution of  $Q$  suggests the location in the target has the most contribution to the inductive loss. The representative plots of  $Q$  under the two types of target geometry show little difference in the spatial distribution of  $Q$ , but the volume integral of  $Q$  decreased by about 30% for the ellipsoid target (Figure 5.6).

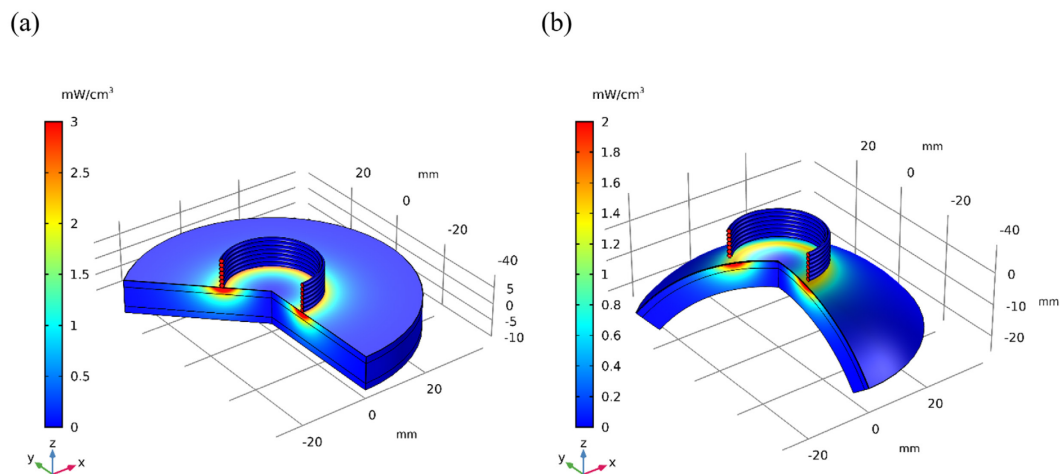


**Figure 5.6:** Volumetric loss function in the (a) cylindrical target and (b) ellipsoid target at 8 MHz. Note the differences in the color map scale.

### 5.3 ANATOMICAL MODEL OF THE HUMAN ANKLE

To capture the anatomical structure of the ankle, I further developed a 3-D foot model and simulated the increase in coil resistance. The foot geometry was imported from an open-source database that provides 3-D models reconstructed from computed tomography (Figure 5.7). The sensor was conformal to the skin surface (with a near constant separation of 1 mm) and located on top of the tibia section near the medial malleolus. The thickness values of the epidermis and dermis are 0.2 mm and 2 mm, respectively. The remaining structure except the bone is assigned to the subcutis. The subcutaneous conductivity was assigned to be 0.2 S/m to mimic a subcutaneous edema with 20% interstitial fluid volume fraction (Figure 5.8).

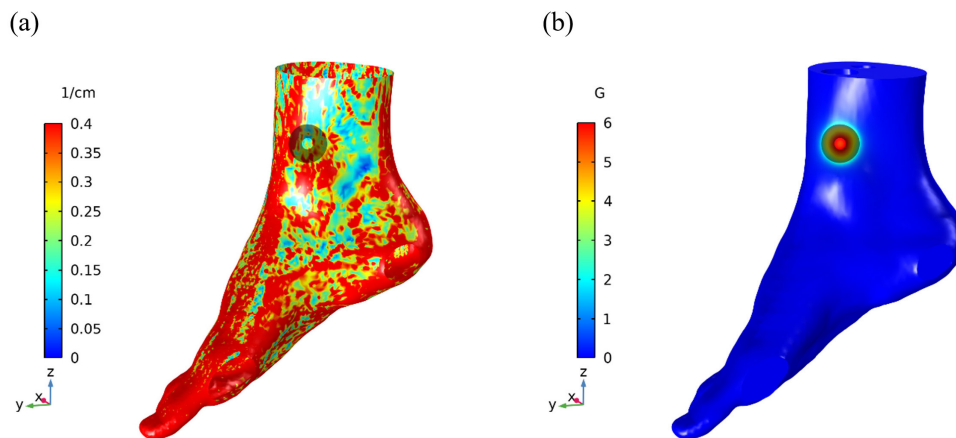


**Figure 5.7:** 3D model of the right foot showing (a) the surface curvature and (b) magnetic flux intensity.

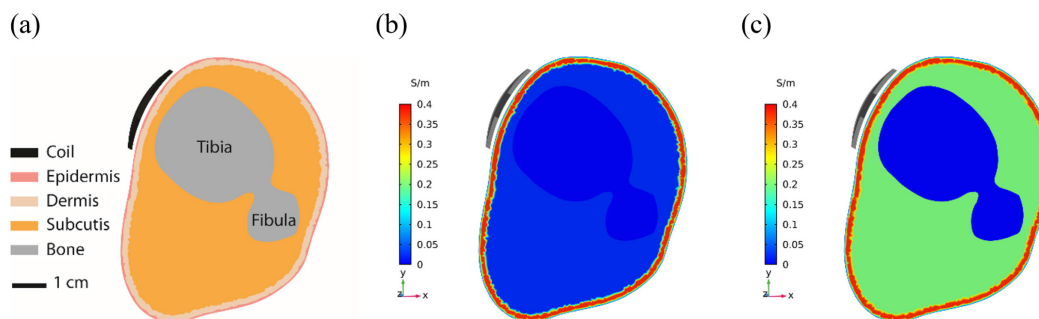


**Figure 5.8:** Cross-sectional views of the ankle showing (a) different layers under the skin and the relative location of the coil sensor, (b) conductivity distribution under normal conditions, and (c) conductivity distribution under subcutaneous edema conditions.

By assigning conductivity values to the epidermis, dermis, and subcutis based on their depth relative to the skin surface, I computed the volumetric loss density and coil resistance in the frequency range of 500 kHz to 10 MHz (Figure 5.9). The bone conductivity is set to zero to improve computational efficiency, as 2-D models suggest the inductive loss in the bone is negligible. The conductivity and permittivity spectra of the dermis are extracted from an online database (IT'IS Foundation, 2021).

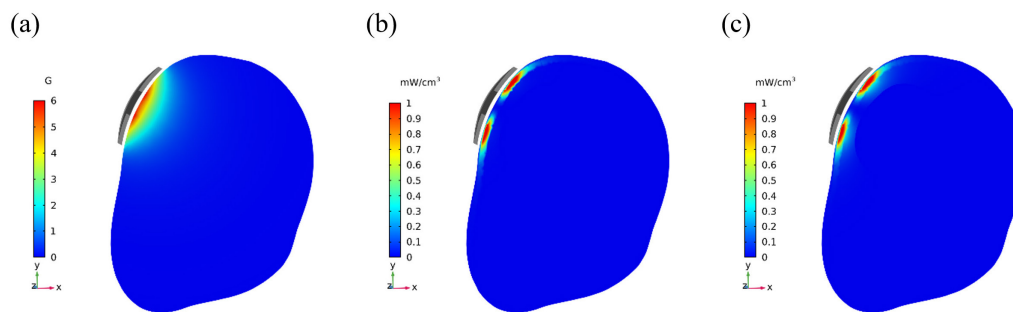


**Figure 5.9:** Cross-sectional views of the ankle showing (a) magnetic flux intensity distribution, (b) volumetric loss density function under normal conditions, and (c) volumetric loss density function under subcutaneous edema conditions.

## 5.4 FABRICATION OF WEARABLE INDUCTIVE DAMPING SENSORS

### *COIL FABRICATION*

The design of the coil is largely constrained by the LDC 1101 ASIC specifications. The manufacturer datasheet states that the coil inductance should be between  $1 \mu\text{H}$  and  $500 \mu\text{H}$ , the sensor resonant frequency should be from 500 kHz to 10 MHz, and the quality factor of the LC-resonator should be between 10 and 400 (Texas Instruments, 2021).

Although coils made from printed circuit boards are easy to mass produce, the quality factor of these coils seldom exceeds 100 in the frequency range around 1 MHz. Therefore, the Litz cable was used to construct the coils for benchtop testing and human subject experiments.

The strand diameter in the Litz cable was selected according to the skin depth at the resonant frequency. The smallest strand diameter available (48 AWG) allows the resonant frequency to operate close to 3 MHz without a significant increase in the coil resistance. The number of strands in the Litz cable was 675, giving a cable diameter of 1.3 mm. This cable diameter allowed a balance between coil resistance per unit length and weight.

As the strands in the Litz cable are individually insulated, all the strands need to be soldered together at the end of the cable. All strands were heated up to >300 degrees Celsius to simultaneously remove the insulation layer and allow solder to wick the bare copper inside. Quality factor measurements confirmed the contact resistance at the coil's terminals is low.

After properly terminating the Litz cable, I wound it around a 1-inch plastic cylinder to make a solenoid coil of seven turns. The number of turns was determined by inductance calculations, and seven turns give an inductance value slightly higher than  $1 \mu\text{H}$ . Then I poured epoxy around the coil and cured it in a convection oven overnight to help fix the coil in place. An acrylic plate of  $\frac{1}{4}$  inch thick was added on the top as a cover to protect the coil. It also reduced the capacitive and thermal coupling to the environment.

#### *PRINTED CIRCUIT BOARD FABRICATION*

The design of the custom printed circuit board (PCB) was completed using the Altium CircuitMaker software. Since the PCB is near the coil sensor, special care was taken to avoid large metal areas or loops for eddy currents to flow. The PCB is ring-shaped with an inner diameter slightly larger than 1-inch to enclose the coil, and an outer diameter of 5 cm to fit into the vacuum pump used in human experiments.

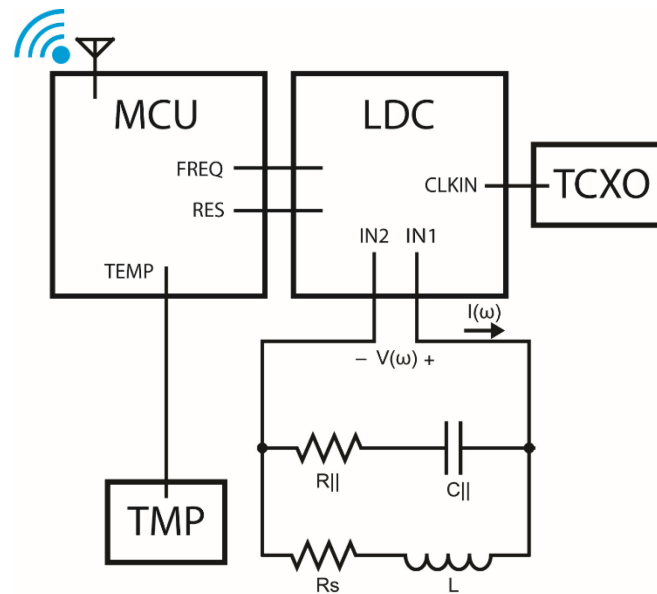


**Figure 5.10:** Block diagram of the custom designed PCB for LDC1101.

The PCB and surface mount components were assembled by the standard reflow process at a peak temperature of 260 degrees Celsius. Staying below 260 degrees Celsius helps to protect the temperature-sensitive package of the LDC1101 ASIC. Other surface mount sensors on board included a temperature sensor for temperature compensation and a pressure sensor to record the suction pressure. The microcontroller was a Bluetooth Low Energy (BLE) module that can communicate with peripheral sensors using the standard I2C and SPI protocols and transmit data to a nearby tablet device or smart phone.

After assembling the PCB, the components were checked with a digital multimeter for accidental short or open circuits during the reflow process. Then the custom firmware was written to the microcontroller and a logic analyzer was connected to trace the packets and debug potential issues.

## **5.5 MEASUREMENTS FROM CONDUCTIVITY STANDARDS, SALINE SOLUTIONS AND GELATIN PHANTOMS**

### *POTASSIUM CHLORIDE CONDUCTIVITY STANDARDS AND SALINE SOLUTIONS*

The potassium chloride solution is commonly used as the conductivity standard for calibrating the conductivity meter. Therefore, I chose it as the initial target for proof-of-concept verifications. The conductivity values tested were 44.7 mS/m, 0.15 S/m, and 1.29 S/m at 25 degrees Celsius. The solution was stored in the original 500 mL plastic container from the manufacturer and remained intact during the measurements.

Before the experiment, the coil sensor was attached to a flat acrylic plate with epoxy and left in a convection oven overnight at 60 degrees Celsius to cure the epoxy. The acrylic plate had a thickness of  $\frac{1}{4}$  inch (6.35 mm) to reduce the capacitive coupling effect and provided a landing site for the test samples. During the experiment, the acrylic plate was held from below by plastic support (Figure 5.11). The cylindrical support helped stabilize the sensor to prevent vertical movements when it was in contact with the bottle containing the conductivity standard. Therefore, the gap between the conductivity standard and sensor is assumed to be equal to the thickness of the acrylic plate. The support also isolated the sensor from nearby objects that could interfere with the output signal. The clearance distance from the surrounding objects was 25 cm or ten times the coil diameter. As shown in chapter 5, this reduced the amount of inductive loss from the fringing magnetic field to less than 10% of the inductive loss in the target.



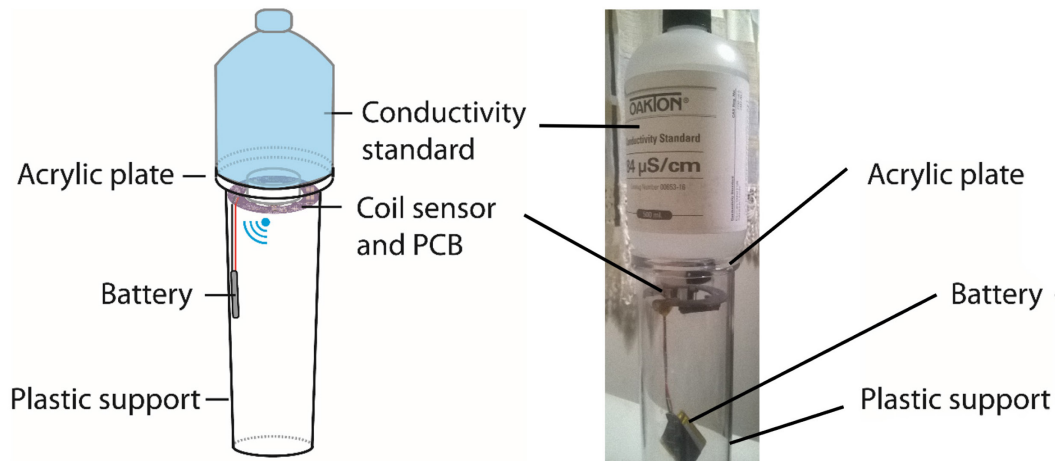


**Figure 5.11:** Schematic drawing (left) and photo (right) of the experimental setup for measuring the conductivity standards. The plastic bottle containing the conductivity standard has a volume of 500 mL and a diameter of 7 cm. The height of the plastic support is 25 cm.

Based on the theoretical analysis (chapter 4), the change in coil resistance should be linearly proportional to the target conductivity. However, in the experiments, the linear relationship was no longer held when the conductivity dropped below  $\sim 0.1$  S/m. One possible explanation is the dielectric loss through the capacitive coupling effect, which represents a resistance offset in the coil resistance versus conductivity plot when conductivity approaches zero (Figure 5.12). The effect can be mitigated by proper electrical shielding.

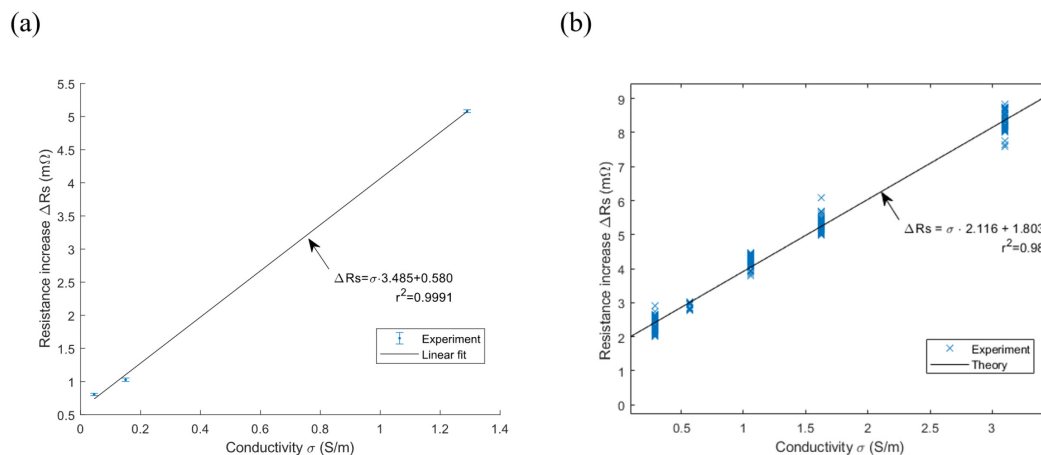


**Figure 5.12:** The coil resistance increase  $\Delta R_s$  as a linear function of conductivity. (a) Results from potassium chloride conductivity standards (500 mL, diameter = 7 cm) measured at 5 MHz. (b) Results from sodium chloride solutions (25 mL, diameter = 2 cm) measured at 7.7 MHz. The room temperature was at 25 degrees Celsius.

### *GELATIN PHANTOMS WITH VARYING THICKNESS AND SALINE SOAKING TIME*

The gelatin phantoms were prepared according to the standard recipe for ballistic gelatin (Wikipedia, 2021). One part of gelatin powder was mixed with nine parts of deionized water to make a 10% gelatin-water mixture by weight.

The gelatin-water mixture was stirred with a magnetic stirrer under continuous heating on a hot plate until all the visible gelatin chunks were dissolved and the solution became light-yellow. Then the solution was poured into a 14-cm diameter plastic petri dish and weighed on a digital laboratory balance with 0.01 g resolution. The solution was cooled at room temperature on a flat surface until it solidified.

The electrical conductivity of the 10% gelatin solution was measured by a conductivity probe, which gave a conductivity reading of 0.063 S/m. Therefore, the ion concentration in the unmodified gelatin was negligible compared to the buffer solution, which has a conductivity of 1.48 S/m at 26 degrees Celsius. Five gelatin

phantoms with the same diameter but different thickness values were prepared by adjusting the amount of gelatin poured into the petri dish. The weight of each gelatin phantom was measured to be 46.0 g, 72.0 g, 104.0 g, and 134.0 g. The corresponding thickness values were 2.8 mm, 3.6 mm, 6.3 mm, 8.1 mm.

After the phantoms became solidified, the Dulbecco's Phosphate Buffered Saline (DPBS) solution was added to the phantom. The phantoms were soaked in DPBS for a maximum of 4 hours and intermittently rinsed with deionized water for conductivity measurements (Figure 5.13).

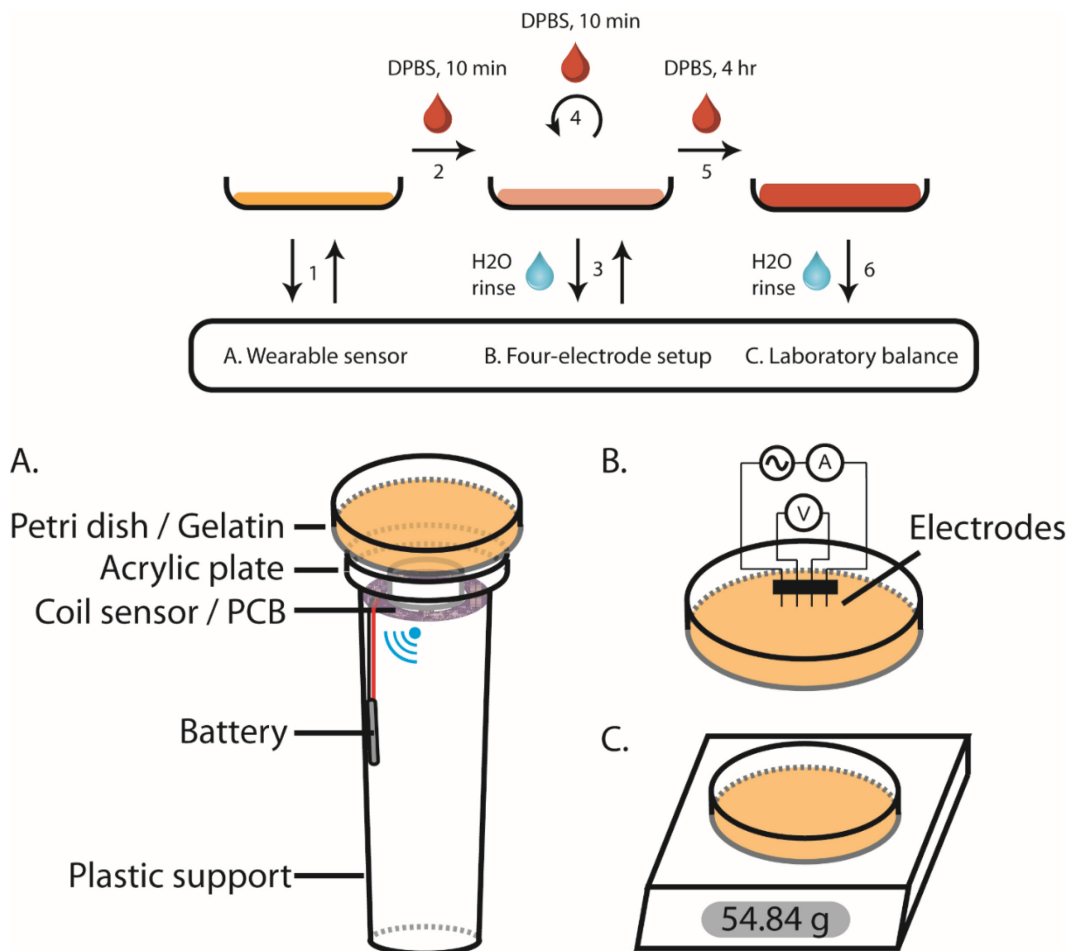


**Figure 5.13:** The experimental setup for gelatin phantom soaking test.

A four-electrode setup was used to measure the gelatin phantom conductivity (Figure 5.14). The electrodes were gold plated pin header with a pitch of 0.1 inch and a cross-sectional area 0.025 inch by 0.025 inch. This allows equal spacing between adjacent electrodes for the four-point probe measurements. The AC voltage source is a commercial signal generator that allows quick sweeping of frequencies (1 kHz to 1 MHz). A peak-to-peak value of 4 V was used for the experiment. A current-sensing resistor of 3.9 k $\Omega$  was used to limit the total current to be less than 1 mA. The voltage waveforms at the sensing electrodes (B and C) were recorded by a digital oscilloscope at a sampling rate of 1 billion samples per second. The subtraction function of the oscilloscope was used to measure the voltage difference across the electrodes. An average of 1024 waveforms was used to reduce the noise from the attenuator in the oscilloscope.

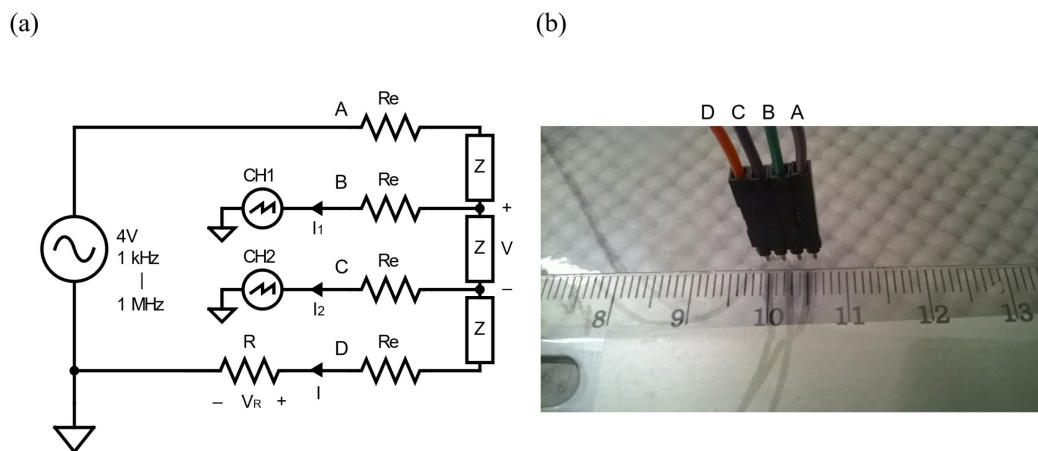


**Figure 5.14:** The four-electrode circuit diagram (left) and experimental setup (right). The currents  $I_1$  and  $I_2$  flowing into the oscilloscope probes are assumed to be negligible compared to the total current  $I$ . The voltage source is from a commercial signal generator. The oscilloscope has a sampling rate of 500 MSPS. The letters (A, B, C, and D) mark the wiring connections to the four electrodes. The electrode pair A-D provides the driving current  $I$  while the pair B-C senses the voltage drop  $V$ . The resistor  $R$  serves a current-sensing element and limits the amount of current flowing through the sample to prevent overload.  $R_e$  denotes the electrode resistance.

The four-point probe equation for the bulk resistivity is (Smits, 1958):

$$\rho = \rho_s t = \frac{V}{I} C \left( \frac{d}{s} \right) F \left( \frac{t}{s} \right) t = \frac{V}{V_R/R} C \left( \frac{d}{s} \right) F \left( \frac{t}{s} \right) t \quad (5.1)$$

, where  $\rho$  is the bulk resistivity,  $\rho_s$  is the sheet resistivity,  $t$  is the thickness of the sample,  $s$  is the separation distance between adjacent electrodes,  $C$  is the diameter correction factor for a circular piece depending on the ratio  $d/s$ ,  $F$  is the thickness correction factor depending on the ratio  $t/s$ ,  $V$  and  $I$  are the voltage and current of the electrode pair B-C,  $V_R$  and  $R$  are the resistor voltage and resistance (Figure 5.15).

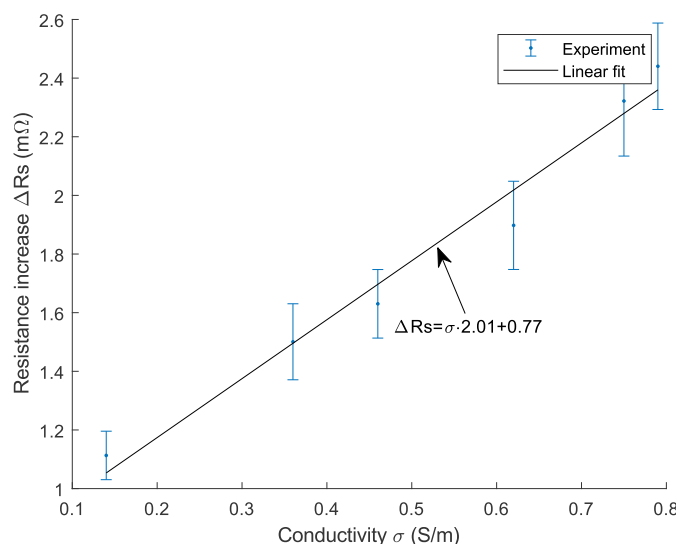


**Figure 5.15:** The measured increase in coil resistance  $\Delta R_s$  as a function of measured four-point probe conductivity from the 46.0 g gelatin phantom. The r-square value of the linear fit line is 0.97.

The plot of  $\Delta R_s$  to  $\sigma$  is close to a straight line like the calibration curve obtained from the conductivity standards. However, one noticeable difference is the upward kink when the conductivity is higher than 0.6 S/m. This can be explained by an increase in gelatin thickness after prolonged soaking in saline, and more eddy currents are allowed to flow and dissipate power. A similar phenomenon is expected in the case of skin edema.

## 5.6 RESULTS FROM HEALTHY HUMAN SUBJECTS

In this section I will describe the measurements on healthy human subjects to establish a baseline of skin conductivity under normal conditions and then move forward with results from the artificially induced skin edema. The method I used was applying a negative suction pressure on the ankle skin, so the pressure difference in the interstitial space became significantly larger than the normal value. According to the revised Starling's equation, the plasma filtration rate was increased by more than ten times. This caused an imbalance between the inflow and drainage in the interstitial space, which eventually resulted in subcutaneous edema. The edema skin thickness was evaluated with a 10 MHz single-element ultrasound transducer and compared to the value predicted by the skin edema model in chapter 2.

### *VACUUM INDUCED SUBCUTANEOUS EDEMA CONDUCTIVITY*

Three healthy volunteers (two males, one female) were recruited for the skin edema sensor experiments. The human experiments were conducted under the protocol approved by the Institutional Review Board at the California Institute of Technology (protocol no. 19-0945). An informed consent was obtained before conducting the experiment.

The human subject protocol involves applying a negative suction pressure on the skin surface near the ankle area. The suction pressure ranged from 5 kPa to 40 kPa below one atmospheric pressure, and the total suction time ranged from 5 minutes to 30 minutes.

A commercially available vacuum pump was integrated with the custom circuit board and coil sensor for vacuum suction (Figure 5.16). The sensor holder is conformal to the skin surface so the separation distance between the sensor and the skin is minimized. A 1-mm thick edema was visible after 30 minutes of suction at 40 kPa, confirming the validity of this method to induce skin edema.

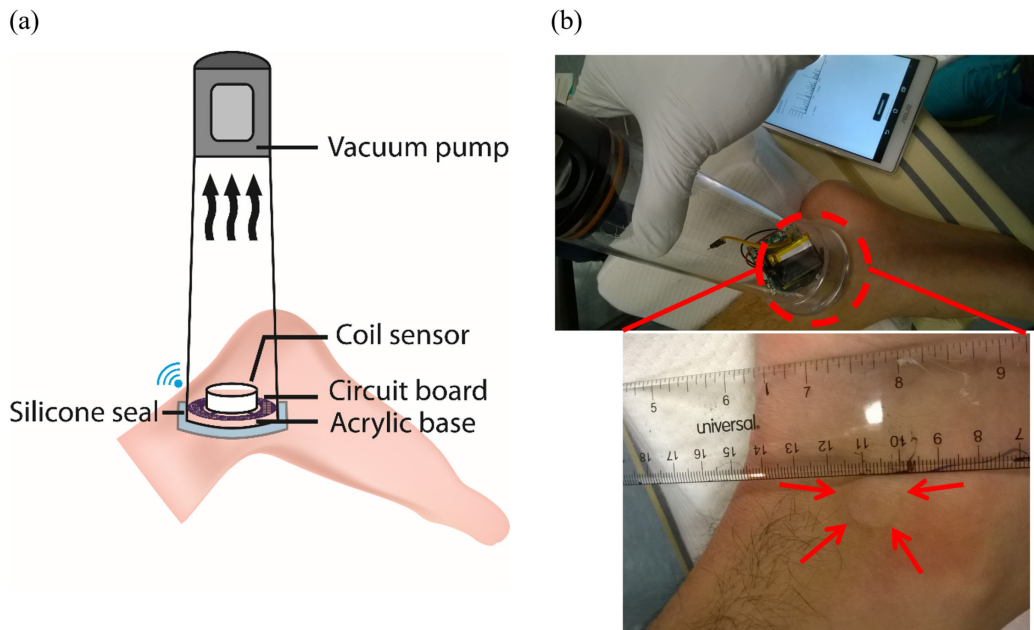


**Figure 5.16:** (a) Schematic drawing of the experimental setup for vacuum suction induced edema, and (b) a photo showing the vacuum pump integrated with the skin edema sensor (top) and the induced skin edema (bottom). Measurements were taken from human ankle over 30 minutes.

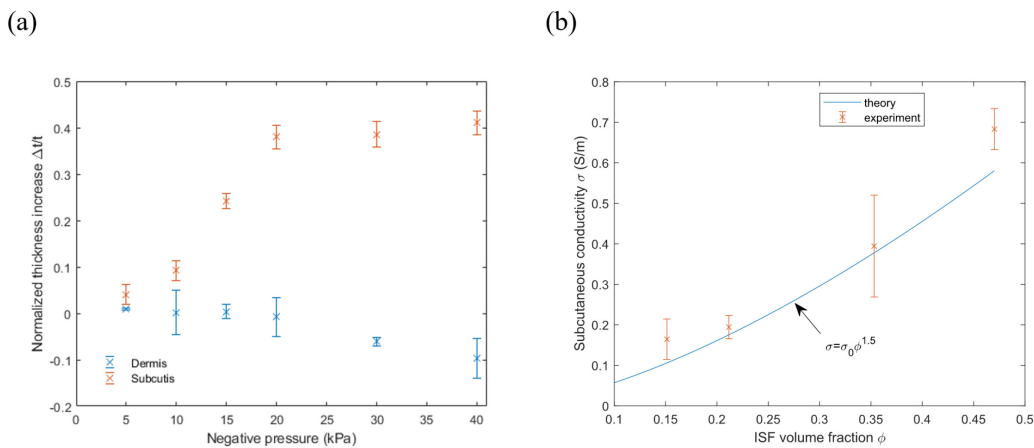


**Figure 5.17:** Experimental results from healthy human subjects. (a) relative thickness change of dermis and subcutis as a function of negative pressure applied to the skin, (b) subcutaneous conductivity predicted by the edema model and Archie's law (blue solid line) and measured by the skin edema sensor (orange error bars). Measurements were taken from human ankle over 15 minutes.

### SKIN THICKNESS MEASUREMENTS

The auxiliary ultrasound skin thickness sensor is not required for skin edema quantification. Still, it provides extra information on the thickness of each skin layer and is used in the experimental setup as the benchmark measurement of skin edema.

Skin thickness is an essential parameter for estimating the interstitial fluid volume fraction. Assuming the skin can be modeled as a three-layer cylinder and denoting the baseline values of the subcutaneous thickness, radius, length, and interstitial fluid volume fraction as  $t_0$ ,  $R_0$ ,  $L_0$ ,  $\phi_0$ , respectively (Figure 2.9), then the edematous interstitial fluid volume fraction can be derived from the change in subcutis thickness:

$$\begin{aligned}\phi &= \frac{2\pi R_0 L_0 t_0 \phi_0 + 2\pi \left(R_0 + \frac{t_0}{2} + \frac{\Delta t}{2}\right) (L_0 + \Delta L) \Delta t}{2\pi \left(R_0 + \frac{\Delta t}{2}\right) (L_0 + \Delta L) (t_0 + \Delta t)} \\ &\approx \frac{R_0 t_0 \phi_0 + \left(R_0 + \frac{t_0}{2} + \frac{\Delta t}{2}\right) \Delta t}{\left(R_0 + \frac{\Delta t}{2}\right) (t_0 + \Delta t)}\end{aligned}\tag{5.2}$$

I used a single-element ultrasound transducer with a center frequency of 10 MHz to capture the skin thickness change with an axial resolution around 0.3 mm from  $t_0$  to  $t_0 + \Delta t$  during the experiment. An off-the-shelf ultrasound transmitter chip drives the transducer with  $\pm 80$  V triple pulses at a pulse repetition rate at 20 Hz. The received signal is amplified by a low-noise amplifier and digitized by an oscilloscope at 1 billion samples per second. The raw signal waveform is collected during the vacuum suction to create a time-motion image for tracking the dermal thickness (Figure 5.18). An optional digital band-pass filter from 5 MHz to 15 MHz can be applied to further enhance the dermis layer.



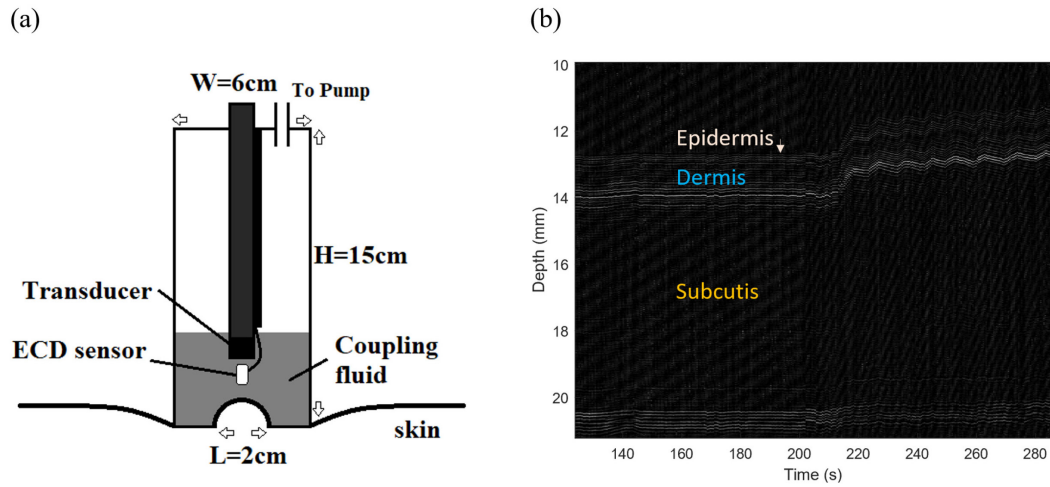


**Figure 5.18:** Skin thickness measurement setup. (left) schematic drawing of the setup dimension and relative locations of the ultrasound transducer and skin edema eddy current damping (ECD) sensor, (right) the motion-mode ultrasound image captured by the skin thickness sensor. The epidermis is below the axial resolution of the ultrasound transducer and is labeled with an arrow to only indicate its boundary.

## 5.7 REFERENCES

- IT'IS Foundation, 2021. Tissue Frequency Chart [WWW Document]. URL <https://itis.swiss/virtual-population/tissue-properties/database/tissue-frequency-chart/> (accessed 10.18.21).
- Smits, F.M., 1958. Measurement of sheet resistivities with the four-point probe. *The Bell System Technical Journal* 37, 711–718. <https://doi.org/10.1002/j.1538-7305.1958.tb03883.x>
- Texas Instruments, 2021. LDC1101 data sheet, product information and support [WWW Document]. URL <https://www.ti.com/product/LDC1101> (accessed 10.18.21).
- Wikipedia, 2021. Ballistic gelatin.

*Chapter 6***MAGNETIC SHIELDING FOR IMPROVED SENSOR  
PERFORMANCE**

In this chapter, I will explore the possibility of using ferrite materials to build magnetic shielding around the sensor coil. The idea is to have air gaps that dominate the reluctance in the magnetic circuit, so the leaking magnetic flux is limited in the proximity of the gap. The advantage of magnetic shielding includes concentrating the induction loss field in the region of interest so the signal-to-noise ratio can be improved. It also helps to reduce the interference from the back of the coil sensor and the environment.

To quantify the effectiveness of the magnetic shielding, I will investigate the spread of the loss distribution in the coil plane and distance away from the coil in the direction perpendicular to the coil plane. Another objective for the first half of this chapter is the ratio of loss in the region of interest normalized to the total induction loss. I will show how to use finite element analysis (FEA) simulations to calculate these objectives and optimize the magnetic shielding geometry. The overall goal is to achieve focused inductive damping in the subcutis.

In the second half of the chapter, I will show experimental results from the optimized design from the FEA simulations. The two objectives are compared with the first sensor prototype on saline tissue phantoms with different width and depth. The results suggest that the improved coil design with magnetic shielding helps to concentrate more than half of the total induction loss in the subcutis layer and reduce the area spread in the horizontal direction. Therefore, the magnetic shielding improves the sensor performance by increasing the damping signal from the subcutis layer and reducing the unwanted signals that are outside the subcutis.

## 6.1 SIMULATION SETUP

The simulations are based on an axially symmetric model for better computer efficiency and faster design iterations. The coil geometry is the same planar circular design from the previous chapter, which consists of three turns in the sample coil plane for maximum geometric damping efficiency. Each turn formed by the Litz cable has a diameter of 1.27 mm. The ferrite geometry encloses the coil windings and the shielding thickness  $t$ , air gap width  $w$ , and height  $h$  are the model parameters (Figure 6.1). The remaining domain is modeled by a large air sphere with infinite domain boundaries.

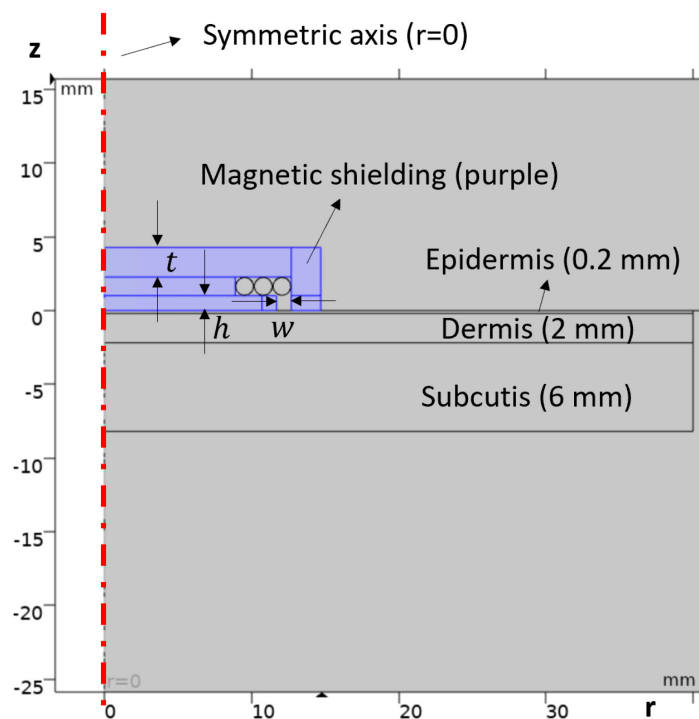


**Figure 6.1:** The schematic drawing of the 2-D axially symmetric model of ferrite magnetic shielding. The symmetric axis is  $r = 0$ . The purple region is the domain that contains the ferrite material with relative permeability of 130. The shielding thickness  $t$ , air gap width  $w$  and height  $h$  are the changing variables. The target ( $z < 0$ ) is positioned right below coil and contains three layers (epidermis, dermis, and subcutis). The region of interest has a cross-section area of 40 mm (width) by 8 mm (depth). The air domain ( $z > 0$ ) surrounds the coil, magnetic shielding, and target from above and is assigned with zero conductivity.

For material properties, the permeability of commercially available ferrite sheets is set to be 130 in the frequency range of 500 kHz to 10 MHz according to the manufacturer's datasheet (Laird Performance Materials, 2021). The imaginary part of the relative permeability has a maximum of 5 at 13.56 MHz and is practically negligible below 10 MHz. Therefore, the ferrite material is assumed to have no magnetic loss in the simulations.

## 6.2 SIMULATION RESULTS

### *SPREAD OF INDUCTIVE LOSS DISTRIBUTION*

The volume integration of the inductive loss density function gives the cumulative loss distribution in the target. Since the model is axially symmetric and the coil center sits at the origin of the r-z coordinate system, it is natural to take the volume integral from  $(r, z) = (0,0)$  to the point of interest:

$$P(r, z) = 2\pi \int_z^0 \int_0^r Q(r', z') r' dr' dz' \quad (6.1)$$

, where  $P(r, z)$  is the cumulative loss function, and  $Q(r, z)$  is the inductive loss density function assuming a uniform conductivity value of 1 S/m in the lower half space  $z < 0$ .

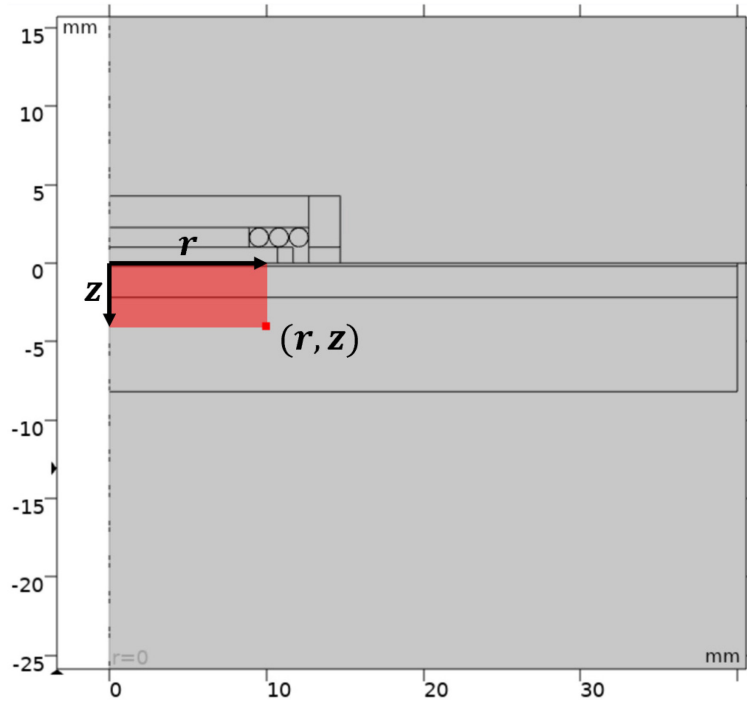


**Figure 6.2:** The schematic drawing of the volume integration to calculate the cumulative loss distribution in the skin ( $z < 0$ ). The red area is the region for the definite volume integral in equation 6.1. Also note that the integration is taken on a revolved geometry that has a symmetric axis at  $r = 0$ .

The selection of 1 S/m is to remove the dependency on the conductivity of individual skin layer and leave out only the power loss weightings  $w_{epi}$ ,  $w_{der}$ , and  $w_{sub}$  (equation 6.2).

$$\sigma_{eff} = \frac{P_{measured}}{P_{ref}} \sigma_{ISF} \approx w_{epi} \sigma_{epi} + w_{der} \sigma_{der} + w_{sub} \sigma_{sub} \quad (6.2)$$

Now if we assume  $w_{epi} \sigma_{epi} \ll \sigma_{eff}$  (the contribution from the epidermis is negligible) and imagine two coil configurations that have linearly independent weighting vectors  $(w^1_{der}, w^1_{sub})$  and  $(w^2_{der}, w^2_{sub})$ , then both the dermis conductivity and subcutis conductivity can be solved as:

$$\begin{pmatrix} w_{der}^1 & w_{sub}^1 \\ w_{der}^2 & w_{sub}^2 \end{pmatrix}^{-1} \begin{pmatrix} \sigma_{eff}^1 \\ \sigma_{eff}^2 \end{pmatrix} = \begin{pmatrix} \sigma_{der} \\ \sigma_{sub} \end{pmatrix} \quad (6.3)$$

Since the loss density function is non-negative and decreasing relatively fast, the limit of  $P(r, z)$  exists when both  $r$  and  $z$  approach infinity, and I will define this value as the maximum loss:

$$P_{max} = \lim_{\substack{r \rightarrow \infty \\ z \rightarrow \infty}} P(r, z) \quad (6.4)$$

Therefore, the ratio of  $P(r, z)$  to  $P_{max}$  defines the loss percentage in the cylinder of radius  $r$  and depth  $z$ . I will define 80% for the loss ratio in the skin (including subcutis) and 40% in the subcutis as the desired values. The remaining 20% of loss is in the bone or other tissue and should be considered as a possible source of measurement errors.

I will first investigate the effect of magnetic shielding thickness  $t$  on the loss distribution. To simplify the problem, the bottom shielding layer is temporarily removed, and the shielding thickness is swept from 1 mm to 8 mm. According to the simulation, doubling the shielding thickness increases the total loss by about 13%. However, changing the shielding thickness does not have a significant effect on the equal loss contours, except for the case  $t = 1$  mm when the loss distribution is slightly more spread out (Figure 6.3). Therefore, I set the thickness of the ferrite magnetic shielding to be 2 mm for a balance between the shielding performance and sensor weight.

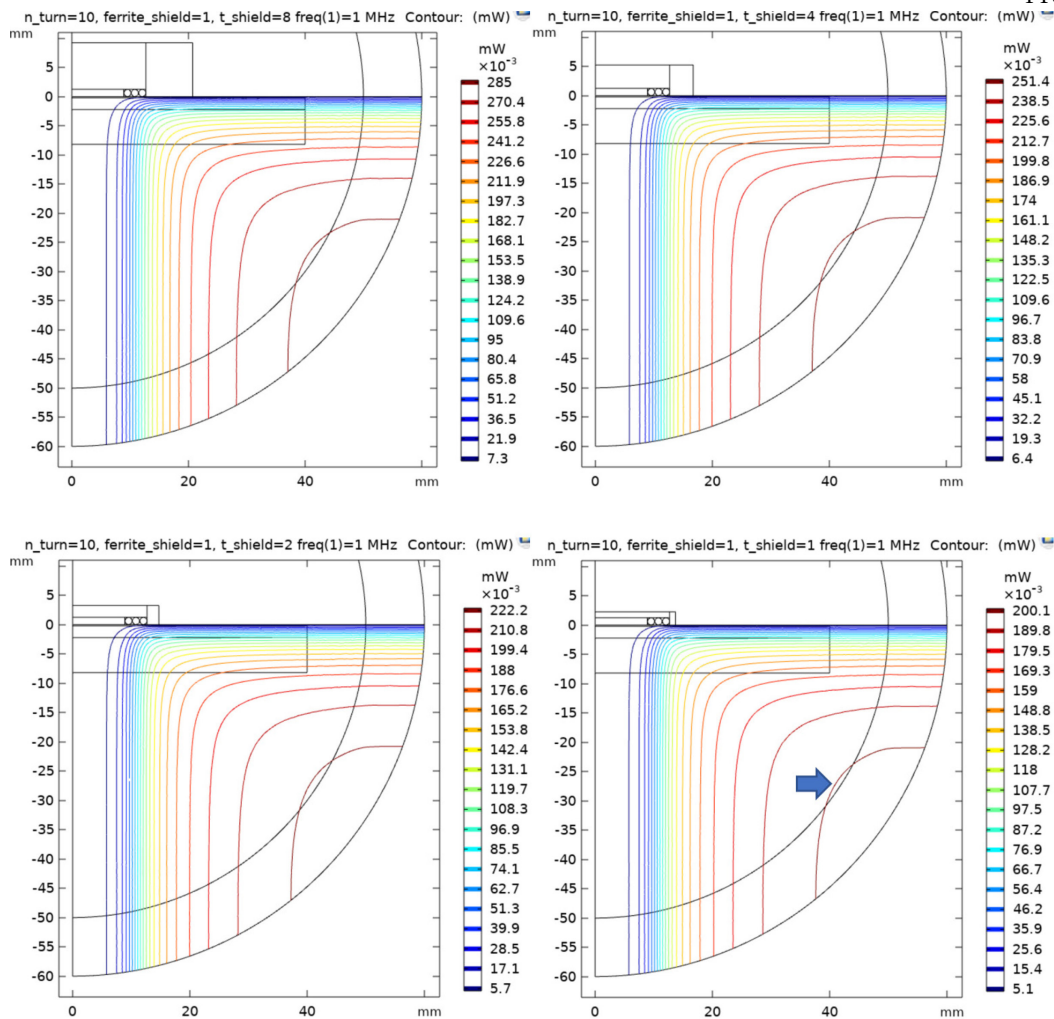


**Figure 6.3:** Comparison of the cumulative loss distribution for the coil sensor with different magnetic shielding thickness values (top-left: 8 mm, top-right: 4 mm, bottom-left: 2 mm, bottom-right: 1 mm). Doubling the shielding thickness increases the total loss by about 13% but has almost no effect on the equal loss contours. For  $t = 1$  mm (bottom-right), a slight change in the 97.5% loss contour is visible (blue arrow).

After investigating the effect of magnetic shielding thickness, I further explore the possibility of adding a bottom shielding layer so that the width of the shielding opening can be adjusted. The thickness of the bottom shielding layer was swept from 0 mm (no bottom shielding) to 4 mm, while the top and side shielding thickness was fixed at 8 mm for consistency (Figure 6.4).



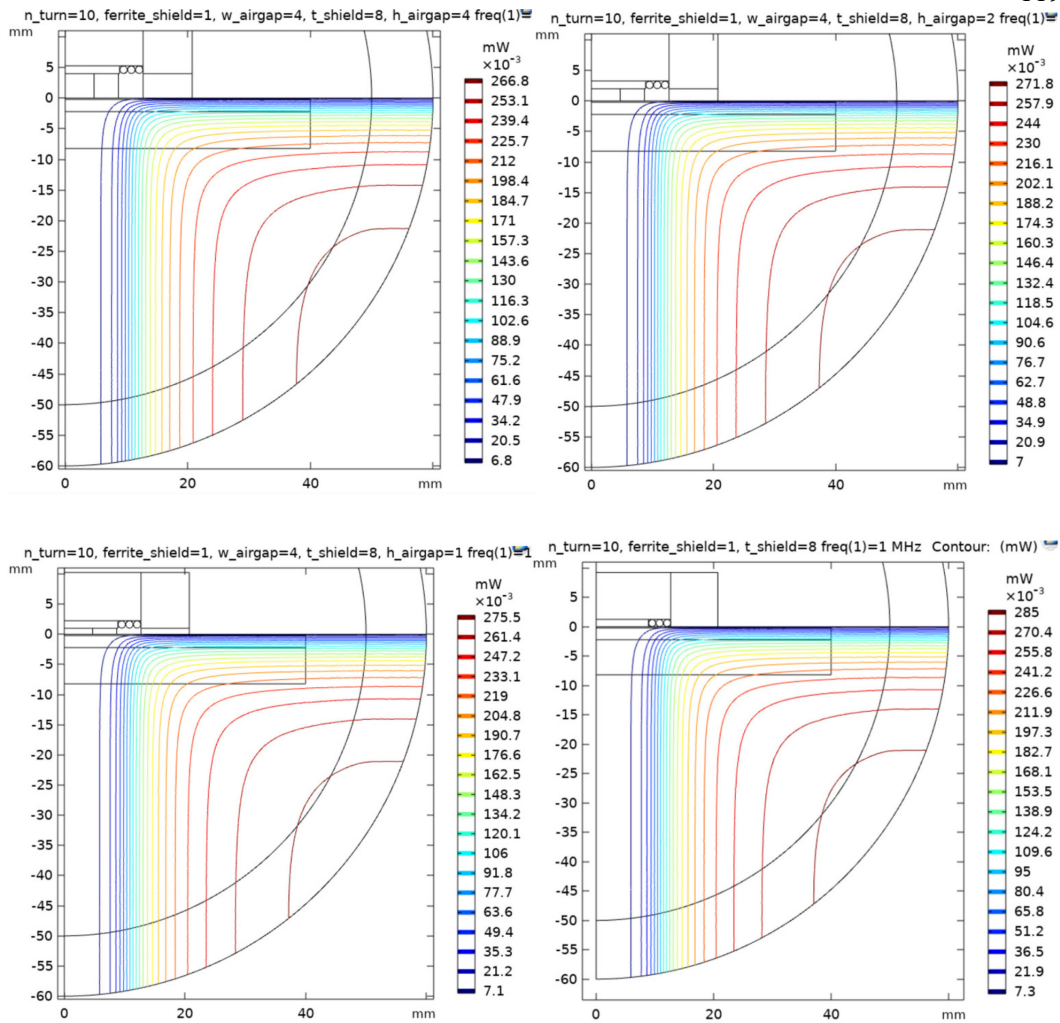


**Figure 6.4:** Comparison of the cumulative loss distribution for the coil sensor with different bottom magnetic shielding thickness values (top-left: 4 mm, top-right: 2 mm, bottom-left: 1 mm, bottom-right: 0 mm). The top and side magnetic shielding thickness is 8 mm. The opening width of the bottom shielding is 4 mm.

According to the simulation results, thinner bottom shielding has higher total inductive loss and slightly more concentrated loss contours. This phenomenon can be explained by the smaller separation between the coil and target. To further investigate the effect of opening width, the bottom shielding thickness is set to 1 mm. The opening width is swept from 0.5 mm to 4 mm in bottom shielding (Figure 6.5).

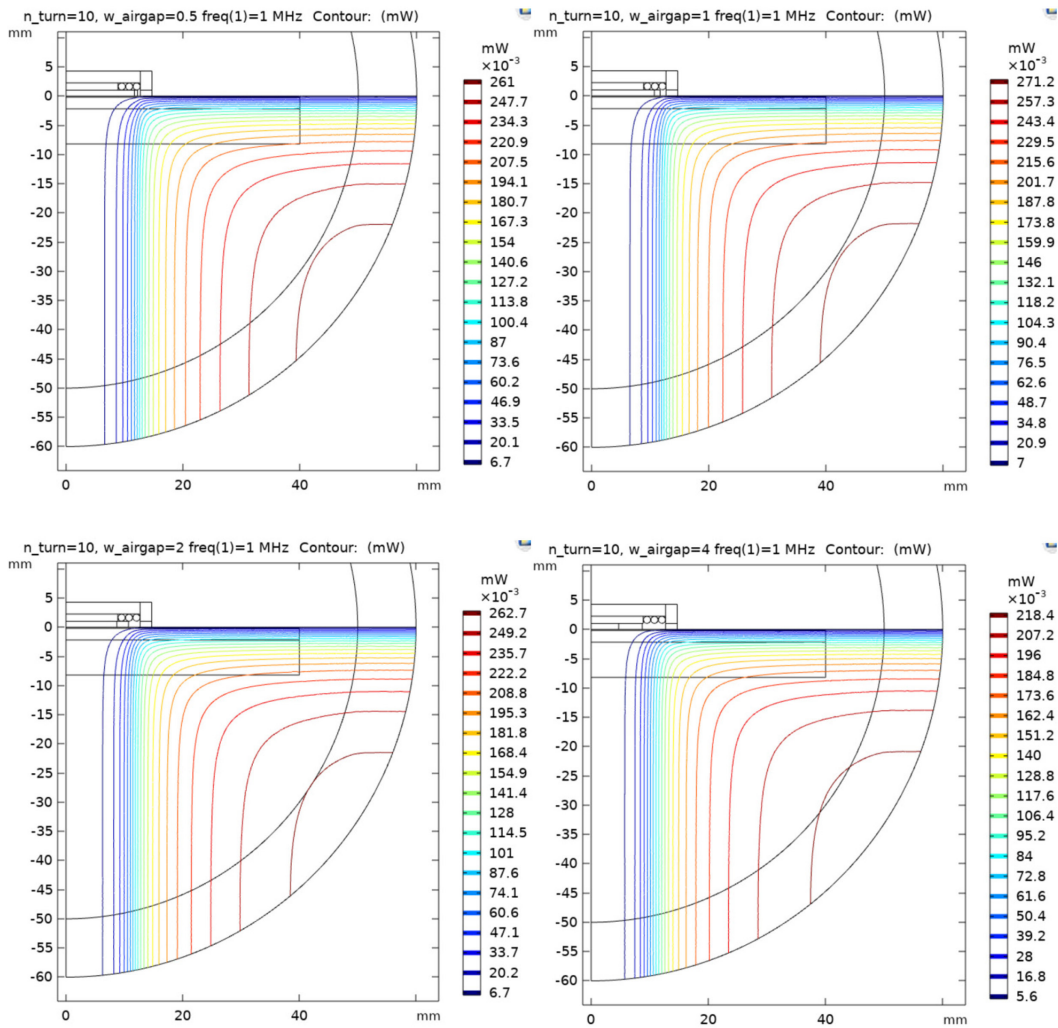


**Figure 6.5:** Comparison of the cumulative loss distribution for the coil sensor with different bottom magnetic shielding opening widths (top-left: 0.5 mm, top-right: 1 mm, bottom-left: 2 mm, bottom-right: 4 mm). The top and side magnetic shielding thickness is 2 mm. The bottom magnetic shielding thickness is 1 mm.

Although smaller opening width seems to have higher total inductive loss, the loss distribution is significantly more spread out (Figure 6.5). The reason is because smaller bottom shielding is blocking a larger portion of the magnetic flux created by the coil windings, which is confirmed by plotting the inductive loss density function (Figure 6.6). As concentrated inductive loss contours are more desirable for the skin

edema sensor, I will stay with the design that has the opening width equal to the coil winding width.

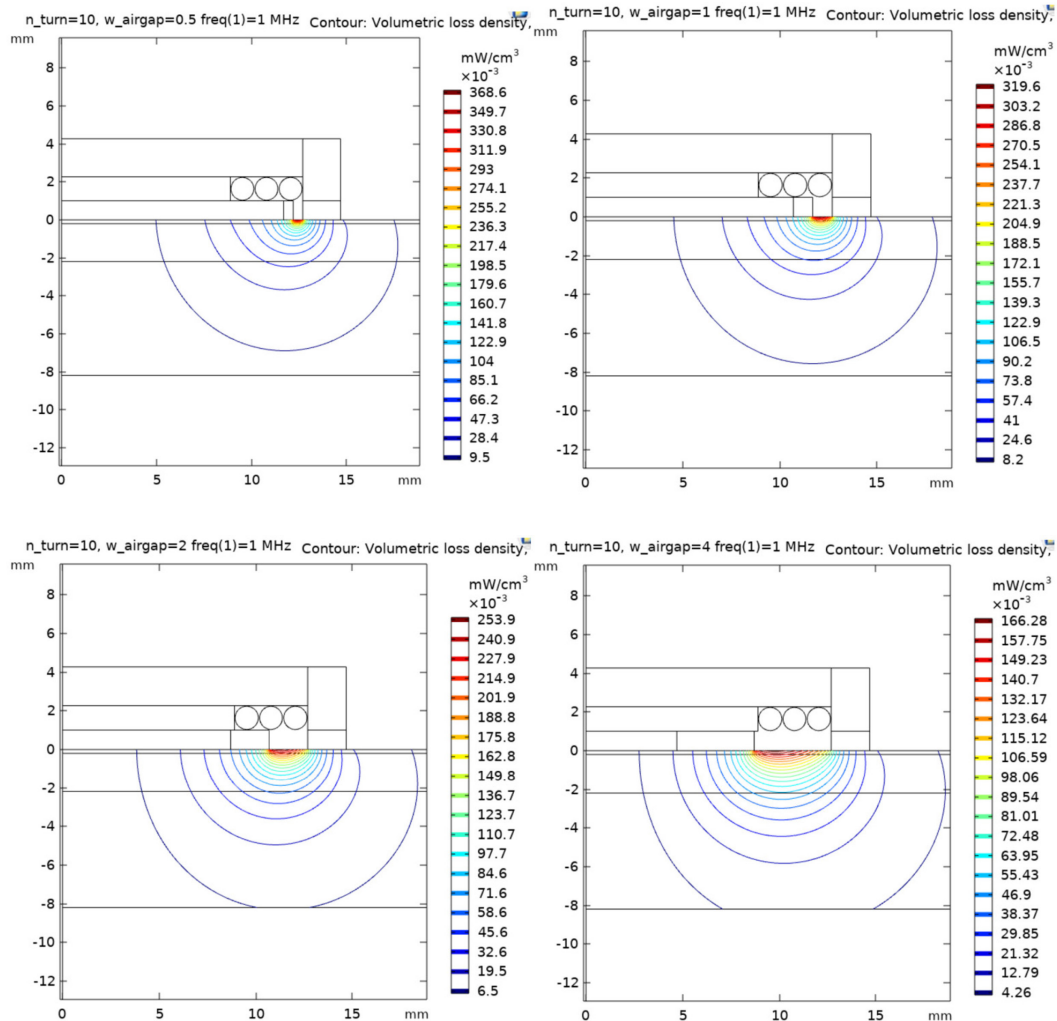


**Figure 6.6:** Comparison of the inductive loss density for the coil sensor with different bottom magnetic shielding opening widths (top-left: 0.5 mm, top-right: 1 mm, bottom-left: 2 mm, bottom-right: 4 mm). The top and side magnetic shielding thickness is 2 mm. The bottom magnetic shielding thickness is 1 mm.

Finally, I will compare the sensor design without magnetic shielding (air coil) with the optimized design with top and side shielding (Figure 6.7). The total inductive loss increases by more than 250%, and the size of the cylinder containing 82.5% of the

total loss is reduced in both the radial and axial directions. The cumulative loss distribution of improved design with magnetic shielding shows a significant reduction in the radial spread (25 mm to 20 mm) and penetration depth (10.5 mm to 8.5 mm) for the 82.5% loss contour (Figure 6.7). This shows the effectiveness of the magnetic shielding design for improved sensor performance.

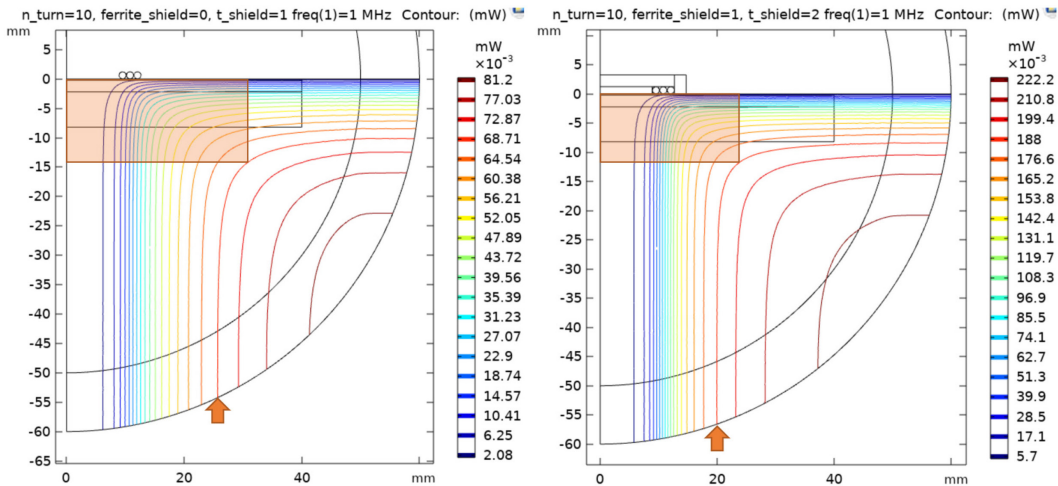


**Figure 6.7:** Comparison of the cumulative loss distribution for the coil sensor without magnetic shielding (left) and with optimal magnetic shielding (right). The 82.5% cumulative loss ratio contours are indicated by orange arrows. Note that  $P_{max}$  increases by more than 250% in the improved sensor design, and radial spread is reduced from 25 mm to 20 mm (orange arrows). The orange boxes represent the cylinder containing 82.5% of total inductive loss.

#### *RATIO OF TARGET LOSS TO TOTAL LOSS*

A simpler way to quantify the inductive loss distribution is to look at the percentage of loss in the target (for example, in the subcutis). Since the spread of the inductive loss distribution is reduced in both directions for the magnetic shielding design, the loss ratio in the bone or other surrounding tissue is expected to decrease and this is confirmed by simulations (Figure 6.8). The ratio of target loss to total loss is also a function of coil to target separation, and this opens an opportunity for choosing a separation distance that maximizes the target loss ratio.

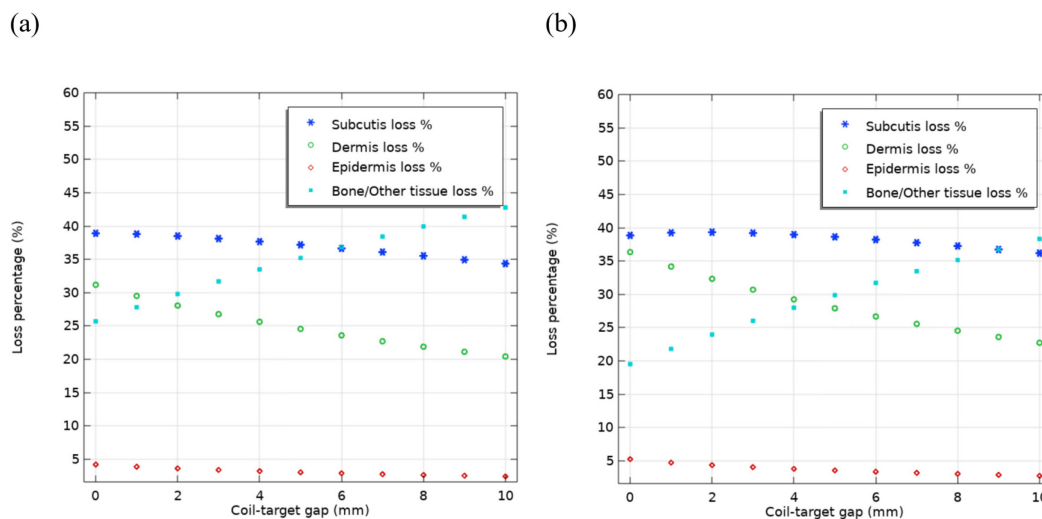


**Figure 6.8:** Loss ratio for different gap distance between the coil and target. (a) Sensor without magnetic shielding, (b) sensor with top and side magnetic shielding (opening width = coil windings width). The optimal separation is 1.5 mm and 4.5 mm for designs with and without magnetic shielding, respectively.

### 6.3 EXPERIMENTAL RESULTS

In the second half of the chapter, I will show experimental results from the optimized design based on FEA simulations. The inductive loss versus depth profile was compared with the first sensor prototype on saline tissue phantoms. The experimental results were obtained using a glass beaker that contains saline solution to verify the improved sensor design with magnetic shielding (Figure 6.9). The diameter of the beaker is about 9 cm, which means the saline thickness increases about 1.6 mm with every 10 mL addition of liquid.

Measurements on the optimal magnetic shielding design show good consistency with the simulations, as the predicted coil resistance increase falls within the error bars of the experimental curve. Furthermore, when compared to the first sensor prototype without magnetic shielding, the improved design exhibited faster rise to the final inductive loss value (Figure 6.10). This confirms the manufacturing of the improved coil design has better sensor performance.

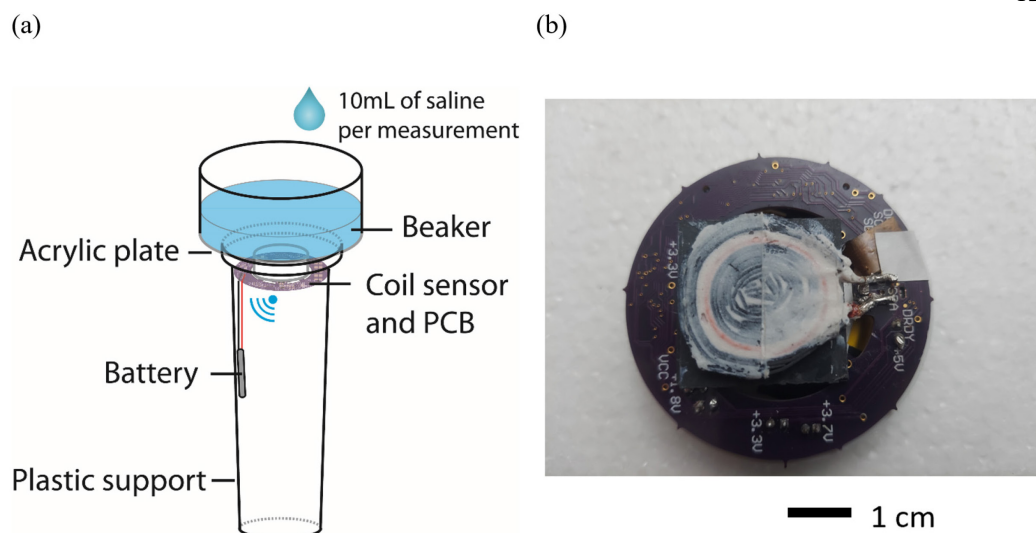


**Figure 6.9:** (a) Schematic drawing of the experimental setup to measure the inductive loss versus depth profile. (b) Photo of the coil sensor with optimized magnetic shielding design.

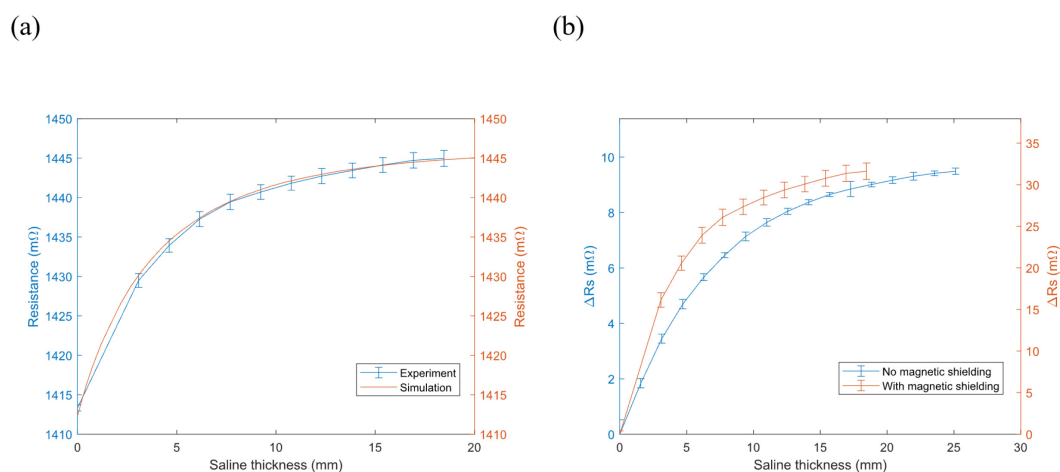


**Figure 6.10:** (a) Comparison of the experimentally measured resistance with simulations for the optimal magnetic shielding design. The only fitting parameter used is the initial coil resistance when no saline is present (saline thickness = 0 mm). (b) Comparison of the measured resistance increase from coil designs with and without magnetic shielding. Note that the vertical scales are set from 0 to 120% of the maximum  $\Delta R_s$  for comparison, and the absolute values differ by a ratio close to 3.5.

## 6.4 REFERENCES

Laird Performance Materials, 2021. MHLL Series [WWW Document]. Laird Performance Materials. URL <https://www.laird.com/products/inductive-components-emc-components-and-ferrite-cores/ferrite-sheets/mhll-series> (accessed 10.18.21).

*Chapter 7*

## CONCLUSION AND FUTURE WORKS

In the previous chapters, I brought up the challenge of continuous and accurate skin edema monitoring and proposed a wearable inductive damping coil sensor as the solution. The solution consists of two parts: the first part is an interstitial fluid model that relates the interstitial fluid volume fraction to the effective skin conductivity, and the second part is the eddy current method that measures the effective skin conductivity. The eddy currents are induced in a time-varying magnetic field to dissipate power in conductive materials like the edematous skin. This power dissipation is proportional to the target conductivity and is represented by an increase in the sensor coil's AC resistance  $\Delta R_s$  which can be measured by a commercially available ASIC.

From the theoretical aspects, I analyzed the sensor coil's AC resistance as a function of frequency, coil geometry, temperature, and effects other than eddy currents. Finite element simulations were conducted to calculate the damping contributions from each skin layer. The results helped to optimize the design of magnetic shielding around the coil, which concentrates the magnetic flux and the loss in the subcutis layer. Benchtop experiments on saline solutions and gelatin phantoms confirmed the linearity of the sensor output as a function of conductivity, and the magnetic shielding helped to reduce the sensing depth that contains 80% of the total damping. Finally, the human subject experiments on vacuum-induced skin edema validated the interstitial fluid model.

Future works include experiments on real edema patients for both cross-sectional (single measurement on patients with different stages of edema) and longitudinal studies (time series measurements on a single patient). with statistical analysis on the sensor's performance in terms of sensitivity and specificity.